Turbulent premixed flames in a model gas turbine combustor: fuel sensitivity and flame dynamics

Pignatelli, Francesco

2023

Document Version:
Publisher's PDF, also known as Version of record

Turbulent premixed flames in a model gas turbine combustor: fuel sensitivity and flame dynamics

FRANCESCO PIGNATELLI
DEPARTMENT OF ENERGY SCIENCES | FACULTY OF ENGINEERING | LUND UNIVERSITY

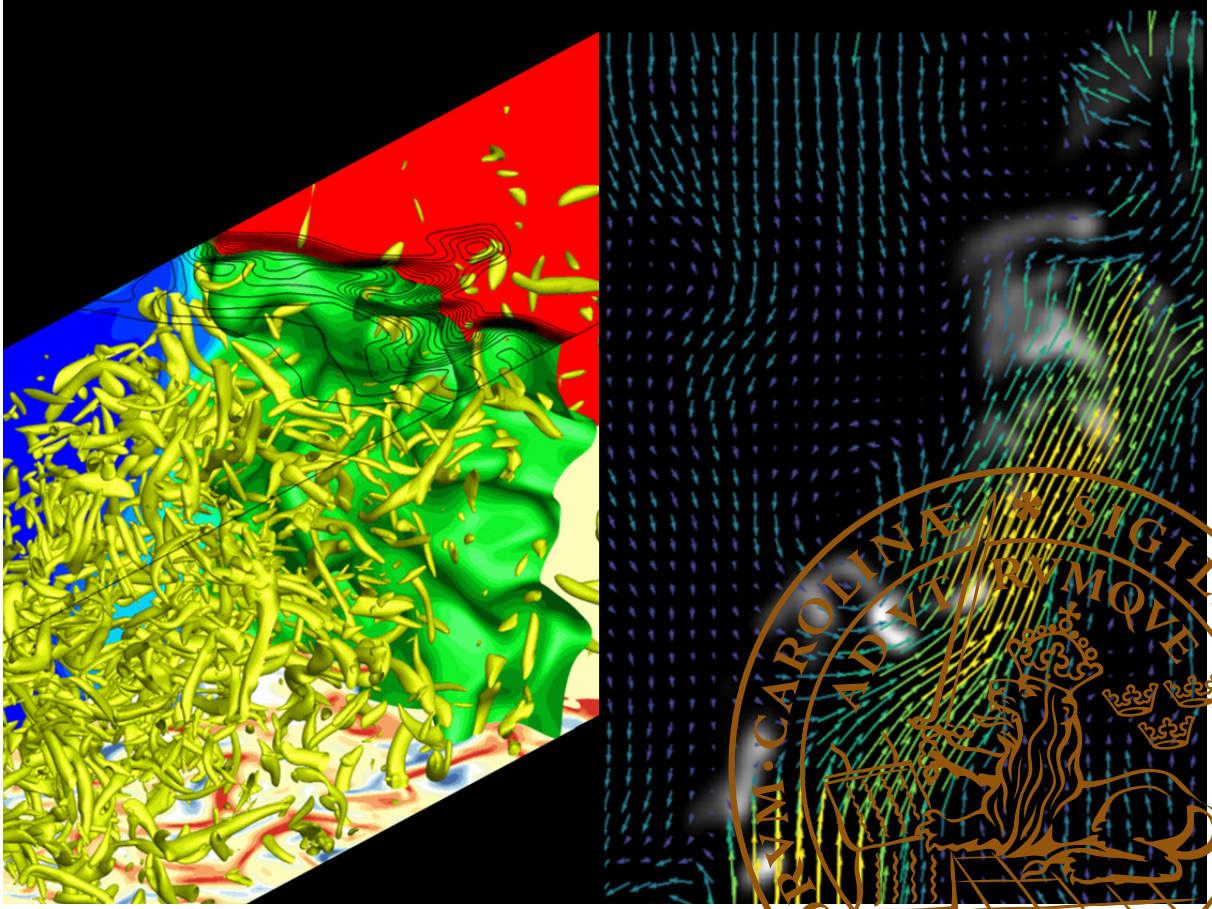

Turbulent premixed flames in a model gas turbine combustor: fuel sensitivity and flame dynamics

Turbulent premixed flames in a model gas turbine combustor: fuel sensitivity and flame dynamics

by Francesco Pignatelli

LUND
UNIVERSITY

Thesis for the degree of Doctor of Philosophy
Thesis advisors: Prof. Xue-Song Bai, Dr. Robert-Zoltán Szász, Docent Rixin Yu, and Dr. Arman Ahmed Subash
Faculty opponent: Prof. Markus Klein, Universität der Bundeswehr München, Germany

To be presented, with the permission of the Faculty of Engineering of Lund University, for public criticism at KC:A lecture hall of the Department of Energy Sciences on June 2, 2023 (Friday) at 10:00.

Organization
LUND UNIVERSITY

Department of Energy Sciences
P.O. Box 118, SE–221 00 LUND
Sweden

Document name
DOCTORAL DISSERTATION

Date of disputation
2023-06-02

Sponsoring organization
Swedish Research Council (VR), Swedish Energy Agency (STEM) through KC-CECOST, Knut & Alice Wallenberg foundation, Swedish National Infrastructure for Computing (SNIC)

Author(s)
Francesco Pignatelli

Title and subtitle
Turbulent premixed flames in a model gas turbine combustor: fuel sensitivity and flame dynamics

Abstract
The demand for energy security and reduction of greenhouse gas emissions has led toa surge of interest in the development of high-efficiency and low-emission gas turbine engines that can run on alternative low carbon content fuels, such as hydrogen-enriched fuel and syngas. However, the combustion characteristics of these fuels can significantly alter the flame characteristics and operability range of existing combustors. Therefore, it is crucial to gain a better understanding of the turbulent combustion characteristics of these fuels from both fundamental and practical perspectives. In this thesis, a combination of numerical and experimental diagnostic methodologies has been employed to investigate how the fuel characteristics can affect the fundamental properties of flames andtheir structure in gas turbine-like combustors. The aim is to provide a comprehensive understanding of the complex combustion processes associated with these alternative fuels.

The propagation of turbulent premixed flames under different density ratio conditions is investigated using direct numerical simulation (DNS). The displacement speed, which characterizes the self-propagation of an isosurface defined based on a reaction progress variable in a turbulent premixed flame, has gained significant interest in the scientific community for flame modeling purposes. In this thesis, a set of new transport equations for dilation and curvature-induced flame stretch rate is derived. Based on the set of evolution equations for displacement speed that takes into account the effects of curvature, normal diffusion, and reactions, this thesis analyzes the thermal expansion effecton the correlation between these quantities. The results reveal four scenarios of flame self-acceleration. The findings provide valuable insights into the understanding of the complex dynamics of turbulent premixed flames.

A newly improved gas turbine model combustor, known as CeCOST burner, is the focus of an experimental campaign that involves laser-based diagnostics techniques, including simultaneous OH-/CH_2O planar laser-induced fluorescence (PLIF), simultaneous OH-PLIF, particle imaging velocimetry (PIV), and phosphor thermometry for surface temperature measurements. High-speed OH* chemiluminescence and exhaust gas measurements are also utilized. The results of the study reveal that hydrogen-enrichment can significantly extend the operation of methane/air to ultra-lean mixtures, resulting in low NO_x emissions. The structures of the flame and the flow show significant variations with hydrogen-enrichment. Isolated flame pockets are identified in lean hydrogen-enriched methane/air flames, as well as in syngas flames where a substantial amount of hydrogen is present. The vortex breakdown structure is found to be strongly coupled with the location of the reaction zones. Furthermore, it is observed that pilot flames can enhance flame stabilization by producing hot gas and radicals that aid in anchoring the flames in the outer recirculation zone of the combustor. The findings of this study provide valuable insights into the combustion characteristics of methane/air, hydrogen-enriched methane/air, and syngas/air flames in the CeCOST burner, as well as the influence of pilot flames on flame and flow structures. These insights contribute to the development of more efficient and environmentally friendly gas turbine combustor designs.

Key words
Fuel flexibility, Premixed Turbulent Combustion, DNS, Optical Diagnostic

Classification system and/or index terms (if any)

Supplementary bibliographical information

Language
English

ISSN and key title
0282-1990

ISBN
978-91-8039-513-7 (print)
978-91-8039-512-0 (pdf)

Recipient's notes

Number of pages
245

Price

Security classification

Turbulent premixed flames in a model gas turbine combustor: fuel sensitivity and flame dynamics

by Francesco Pignatelli

LUND
UNIVERSITY

A doctoral thesis at a university in Sweden takes either the form of a single, cohesive research study (monograph) or a summary of research papers (compilation thesis), which the doctoral student has written alone or together with one or several other author(s).

In the latter case the thesis consists of two parts. An introductory text puts the research work into context and summarizes the main points of the papers. Then, the research publications themselves are reproduced, together with a description of the individual contributions of the authors. The research papers may either have been already published or are manuscripts at various stages (in press, submitted, or in draft).

Cover illustration front: Left half: 3D snapshots of a DNS simulation showing an isosurface of $\hat{c} = 0.3$ (green), projection of c-field (left plane), c-isolines (top plane), density-weighted displacement speed (bottom plane), and rotating flow structures indicated by Lambda2-vortexes (yellow tubes). Right half: instantaneous flow field (colored with the velocity magnitude) superimposed to corresponding instantaneous OH-PLIF snapshot for syngas mixture (3% CH_4, 44% CO and 53% H_2 in vol.) for equivalence ratio 0.47.

Funding information: Swedish Energy Agency (STEM) through KCCECOST, Knut Alice Wallenberg foundation (KAW COCALD project).

Faculty of Engineering, Department of Energy Sciences

ISBN: 978-91-8039-513-7 (print)
ISBN: 978-91-8039-512-0 (pdf)
ISSN: 0282-1990
ISRN: LUTMDN/TMHP-23/1172-SE

Printed in Sweden by Media-Tryck, Lund University, Lund 2023

Contents

List of publications

This thesis is based on the following publications, referred to by their Roman numerals:

I **Displacement Speed Analysis of Surface Propagation in Moderately Turbulent Premixed Reacting Waves**
Francesco Pignatelli, Rixin Yu, Xue-Song Bai, Karl-Johan Nogenmyr
Physics of Fluids 33, 035109 (2021)
https://doi.org/10.1063/5.0039023

II **Pilot Impact on Turbulent Premixed Methane/Air and Hydrogen-Enriched Methane/Air Flames in a Laboratory-Scale Gas Turbine Model Combustor**
Francesco Pignatelli, Haisol Kim, Xin Liu, Arman Ahamed Subash, Robert Zoltan Szasz, Xue-Song Bai, Christian Brackmann, Marcus Aldén, Daniel Lörstad
International Journal of Hydrogen Energy 47, 60 (2022)
https://doi.org/10.1016/j.ijhydene.2022.05.282

III **Impact of Pilot Flame and Hydrogen Enrichment on Turbulent Methane/Hydrogen/Air Swirling Premixed Flames in a Model Gas Turbine Combustor**
Francesco Pignatelli, David Sanned, Saeed Derafshzan, Robert Zoltan Szasz, Xue-Song Bai, Mattias Richter, Daniel Lörstad, Per Petersson, Arman Ahamed Subash
Manuscript to be submitted to Fuel

IV **Impact of Methane and Hydrogen-Enriched Methane Pilot Injection on the Surface Temperature of a Scaled-Down Burner Nozzle Measured Using Phosphor Thermometry**
Henrik Feuk, **Francesco Pignatelli**, Arman Ahamed Subash, Ruike Bi, Robert-Zoltán Szász, Xue-Song Bai, Daniel Lörstad, Mattias Richter
International Journal of Turbomachinery Propulsion and Power 7, 29 (2022)
https://doi.org/10.3390/ijtpp7040029

V **Effect of CO2 Dilution on Structures of Premixed Syngas/Air Flames in a Gas Turbine Model Combustor**
Francesco Pignatelli, Saeed Derafshzan, David Sanned, Nikolaos Papafilippou, Robert-Zoltán Szász, Muhammad Aqib Chishty, Per Petersson, Xue-Song Bai, Rikard Gebart, Andreas Ehn, Mattias Richter, Daniel Lörstad, Arman Ahamed Subash
Manuscript under Review in Combustion and Flame

Publications not included in this thesis:

I **Pilot Impact On Swirling Combustion Characteristics Of Premixed Methane/Air Flame Structure**
Francesco Pignatelli, Arman Ahamed Subash, Robert Zoltan Szasz, Xue-Song Bai, Marcus Aldén, Daniel Lörstad, Per Petersson
12th Mediterranean Combustion Symposium - Luxor, Egypt

II **Numerical Simulations of Spray Combustion in Jet Engines**
Arvid Åkerblom, **Francesco Pignatelli**, Christer Fureby
Aerospace 9, 838 (2022)
https://doi.org/10.3390/aerospace9120838

III **Predictions of Spray Combustion using Conventional Category A Fuels and Exploratory Category C Fuels**
Francesco Pignatelli, Martin Passad, Arvid Åkerblom, Thommie Nilsson, Elna Nilsson and Christer Fureby
AIAA SCITECH 2023 Forum, 23-27 January 2023 National Harbor, MD
https://doi.org/10.2514/6.2023-1486

Acknowledgements

First of all, I would like to express my sincere gratitude and appreciation to my supervisors Prof. Xue-Song Bai, Dr. Robert-Zoltán Szász, Dr. Arman Ahmed Subash, and Docent Rixin Yu, who gave me the chance to study and carry out research in this exciting field. You have always been available for discussions, provided me suggestions about directives for the research, and helped me improving the quality of my manuscripts. I feel I could not ask for more from you. It was a great pleasure and honour to work with and learn from you. I would also like to my sincere gratitude to Prof. Christer Fureby that granted my research during the third year of my PhD and that gave me the opportunity to explore new frontiers of aviation fuels. I would also like to thank my co-authors. Thanks for helping me with numerical models and experiments, for helping to analyze the results from different perspectives, and also for the writing and revision of the papers.

I truly enjoyed the time I have spent at Lund University as a PhD student, mainly thank to the great people I met here. I am very grateful to the senior staff and the colleagues at the Department of Energy Sciences, Hesameddin Fatehi, Catarina Lindén, Isabelle Frej, Johan Revstedt, and Magnus Genrup. I will never forget the help and advice that you provided to me whenever I needed it, and all the things that I have learnt from you. I am also extremely grateful to my wonderful friends in the department, Michael Bertch, Seyed Morteza Mousavi, Shijie Xu, Leilei Xu, Miao Yang, Mark Treacy, Yuxiang Lim, Heng Hu, Alessandro Ercole, Himani Garg, and Guillaume Sahut and all the other students and postdocs that I met at the department. We had a very great time together. I would like to thank my friends met here in Sweden, I was extremely lucky to have found you out of the department. I have never felt alone in the past years here, simply because of your kind presence. The gatherings, random discussions, fun activities, and all the time we spent together is something that will be always on my mind and my soul. We will always be friends.

Words cannot express my gratitude to my family, Fabrizio, Stefania, Manuela and Alex. You taught me that distance is nothing compared to love. My special thanks go to my girlfriend, Francesca. You have been patient and understanding the whole time, and I am so glad that I have found you and you are in my life.

Finally, I acknowledge the financial support for this work from the Swedish Research Council (VR), the Swedish Energy Agency (STEM) through KC-CECOST, the Knut & Alice Wallenberg foundation (KAW COCALD project), and the Swedish National Infrastructure for Computing (SNIC) for providing

the resources for computation.

Popular science summary

Modern society heavily relies on combustion processes to satisfy the different energy demands of everyday life. Combustion still plays a vital role in fulfilling the needs of a vast range of sectors, e.g., transportation, heating, propulsion, and industrial processes. Although renewable energy sources, such as solar, hydro, and wind energy, exist, more than 80% of the total global energy is provided by combustion devices, e.g., internal combustion engines and gas turbines, using fossil fuels. However, the main drawback of the combustion of these types of fuels is the emission of unwanted species that represent health and environmental hazards. The primary emissions are carbon dioxide (CO_2), carbon monoxide (CO), unburned hydrocarbons, particulate matter, nitrogen oxides (NO_x), and in some applications, sulfur oxides (SO_x) and heavy metals. Furthermore, the availability of fossil fuels is limited, representing a severe problem in modern times when the energy demand constantly increases over time. Therefore, it is of enormous interest to discover and develop alternative fuels that can (i) be easily accessed and (ii) be able to reduce the level of pollutants. To this end, a question arises: how is the performance of combustion devices affected by using a different fuel?

It is generally impossible to replace an existing fuel with another one, as different fuels have different burning speeds. Some fuels burn faster than others, while some burn slower. Ideally, the flame should be located in the combustion chamber of the device. However, if a fuel burns slower than the original fuel for which the device was designed, the flame may be pushed out of the combustion chamber. This phenomenon is known as a blow-out. On the other hand, if the fuel burns too quickly, the flame may move toward the fuel supply pipes. This is known as a flashback. Neither of these phenomena is desirable, as they can cause the flame to disappear or damage the device. Therefore, it is essential to carefully consider the fuel's properties and the device's design before attempting to replace the fuel. In some cases, modifications may need to be made to the device to ensure that the new fuel can be used safely and effectively.

This thesis addresses the above issues, focusing on gas turbine engines. Gas turbines are engines that can convert the chemical energy content of a fuel into mechanical power. In stationary applications, this power can be connected to a generator for electric power generation. Gas turbines typically consist of three main parts: a compressor, a combustor, and a turbine. The combustor is often operated using premixed natural gas flames. The need to address the challenge of reducing environmental impact has increased interest in carbon-free fuels such as green hydrogen. The absence of carbon atoms eliminates the production of

some pollutant species such as CO and CO_2. However, hydrogen flames have much higher flame speeds than natural gas and are very unstable in existing gas turbine combustors. Therefore, it is common to blend hydrogen with other fuels, such as natural gas, rather than burning pure hydrogen.

In modern gas turbine engines for electricity production, the fuel and air are often premixed before being supplied to the combustion chamber. By reducing the amount of fuel mixed to the air to form a fuel-lean reactant mixture, it is possible to reduce the flame temperature, thus the emission of NO_x. However, the flame under this fuel-lean mixture conditions becomes harder to stabilize. The flame propagation depends on the chemical reaction, the turbulent flow in the combustor, the interaction of the fresh products with already burned gases, and the heat transfer of the flame with the surrounding environment. Investigating these various physical and chemical processes is crucial to understand flame propagation. This can be done using experimental methods and numerical simulations.

Accurate measurement techniques are required to visualize and observe what is happening during combustion. Within this context, laser-based diagnostic techniques represent a reliable method to investigate flames due to their capability of capturing very small phenomena that occur in a short time. Furthermore, these techniques give the possibility to provide information such as velocity field, species distribution, and temperature without disturbing the chemical processes and flame dynamics. Additionally, numerical simulations are commonly employed to investigate flame characteristics. In this approach, flames are described using mathematical equations solved using computer programs, providing an opportunity to achieve a deeper understanding of the flames.

In this thesis, I have utilized experimental and numerical approaches to investigate the flame dynamics of new fuels for gas turbine engines, including carbon-free hydrogen and biomass-derived syngas. The objective is to better understand flame propagation and its dynamics for different fuels under conditions relevant for gas turbines. The main contributions of this thesis are: (i) the understanding of the thermal expansion effect on the flame propagation speed; (ii) the characterization of flame structures and dynamic behavior of different fuels, including hydrogen, biomass-derived syngas, and mixtures of hydrogen and natural gas. Since applying laser-based measurement techniques in actual gas turbines is impossible, the experiments reported in this thesis were carried out in a smaller model gas turbine combustor that mimics the behaviour of the ones used to electric power generation. The results explain the processes leading to CO and NO_x emissions under various fuel/air mixture conditions. A fundamental understanding of local flame propagation characteristics is provided

using high-fidelity numerical simulations. The results provide insights into the basic combustion processes in the combustor, aiding in the design of gas turbine engines operating on renewable carbon-free or carbon-neutral fuels to address the UN Paris agreement on the decarbonization of our society and industry.

Abstract

The demand for energy security and reduction of greenhouse gas emissions has led to a surge of interest in the development of high-efficiency and low-emission gas turbine engines that can run on alternative low carbon content fuels, such as hydrogen-enriched fuel and syngas. However, the combustion characteristics of these fuels can significantly alter the flame characteristics and operability range of existing combustors. Therefore, it is crucial to gain a better understanding of the turbulent combustion characteristics of these fuels from both fundamental and practical perspectives. In this thesis, a combination of numerical and experimental diagnostic methodologies has been employed to investigate how the fuel characteristics can affect the fundamental properties of flames and their structure in gas turbine-like combustors. The aim is to provide a comprehensive understanding of the complex combustion processes associated with these alternative fuels.

The propagation of turbulent premixed flames under different density ratio conditions is investigated using direct numerical simulation (DNS). The displacement speed, which characterizes the self-propagation of an isosurface defined based on a reaction progress variable in a turbulent premixed flame, has gained significant interest in the scientific community for flame modeling purposes. In this thesis, a set of new transport equations for dilation and curvature-induced flame stretch rate is derived. Based on the set of evolution equations for displacement speed that takes into account the effects of curvature, normal diffusion, and reactions, this thesis analyzes the thermal expansion effect on the correlation between these quantities. The results reveal four scenarios of flame self-acceleration. The findings provide valuable insights into the understanding of the complex dynamics of turbulent premixed flames.

A newly improved gas turbine model combustor, known as CeCOST burner, is the focus of an experimental campaign that involves laser-based diagnostics techniques, including simultaneous OH-/CH_2O planar laser-induced fluorescence (PLIF), simultaneous OH-PLIF, particle imaging velocimetry (PIV), and phosphor thermometry for surface temperature measurements. High-speed OH* chemiluminescence and exhaust gas measurements are also utilized. The results of the study reveal that hydrogen-enrichment can significantly extend the operation of methane/air to ultra-lean mixtures, resulting in low NO_x emissions. The structures of the flame and the flow show significant variations with hydrogen-enrichment. Isolated flame pockets are identified in lean hydrogen-enriched methane/air flames, as well as in syngas flames where a substantial amount of hydrogen is present. The vortex breakdown structure is found to

be strongly coupled with the location of the reaction zones. Furthermore, it is observed that pilot flames can enhance flame stabilization by producing hot gas and radicals that aid in anchoring the flames in the outer recirculation zone of the combustor. The findings of this study provide valuable insights into the combustion characteristics of methane/air, hydrogen-enriched methane/air, and syngas/air flames in the CeCOST burner, as well as the influence of pilot flames on flame and flow structures. These insights contribute to the development of more efficient and environmentally friendly gas turbine combustor designs.

Chapter 1

Introduction

Motivation

Despite the recent increase in energy production from alternative pathways, combustible fuels still represent the primary source of human energy supply. A recent technical report from the International Energy Agency [1] highlights that the combustion of fossil fuels, such as coal, oil, and natural gas, provides around 82% of worldwide energy consumption, making it the main contributor to global warming. Currently, energy consumption and pollutant emissions have bounced back to pre-COVID-19 levels due to post-pandemic economic recovery [2]. Therefore, comprehensive research on the combustion of alternative fuels is needed to fulfill society's energy needs while reducing pollutant emissions. These pollutant species include unburned hydrocarbons (UHCs), carbon monoxide (CO), nitrogen oxides (NO_x), and soot. UHCs are a pollutant in themselves and an indicator of the combustion efficiency of a device. They are mainly formed where the flame is quenched or in regions where combustion does not occur. CO and NO_x are toxic species usually formed at low (CO) or very high (NO_x) flame temperatures. Soot is a generic term representing a wide collection of large carbon-chain compounds (with a size above 10 nm) formed under fuel-rich conditions. A driving force behind combustion research is reducing pollutant emissions while maintaining high combustion device efficiency. The latter is crucial to reduce fuel consumption and, consequently, carbon dioxide emission (CO_2), one of the main greenhouse gases. In addition to achieving low emission levels, ensuring the stable operation of combustion devices is essential, making control of combustion processes a key priority. Furthermore, investigating alternative fuels is crucial due to the increasing price of fossil fuels resulting

from their depletion and higher energy demands.

Gas turbines are considered one of the best devices for generating power, according to Saravanamuttoo [3]. The combustion process occurs in a turbulent environment in gas turbine combustors. Turbulence enhances the mixing between air and fuel, accelerating the combustion process through rapid heat and mass transfer. This allows combustion to occur in a more compact chamber. Additionally, combustion in gas turbine combustors often occurs under lean premixed conditions to reduce the emissions of soot and NO_x. In such conditions, the fuel and oxidizer are mixed before combustion at a low fuel-to-air ratio, meaning a low equivalence ratio. Lean premixed conditions are favorable for low pollutant emissions. However, the resulting flame is more prone to combustion stabilization problems.

Previous investigations of combustion processes have been conducted through both fundamental and applied experimental and numerical methods. Optical techniques based on lasers are the most common experimental diagnostics for flames. The interaction between laser photons and combustion atoms/molecules results in a signal that can be detected by an appropriate detector, providing qualitative and/or qualitative information on flame characteristics. Since the interaction between light and matter occurs at small scales, larger-scale phenomena, e.g., combustion chemistry and flow field, are practically unaffected by the laser beam. This makes the diagnostic methodology non-intrusive. Furthermore, the interaction of turbulent eddies and chemical reactions requires the usage of time- and space-resolved techniques to understand the flame dynamics properly [4]. Laser diagnostics can also be used for species-specific studies tuning the laser beam to a specific wavelength. However, it is challenging to achieve high turbulence levels in laboratory combustion environments [5]. To properly understand the flame dynamics, it is desired to investigate several species simultaneously; however, such simultaneous multi-species measurements are complex, expensive, and limited to a few species [6–11]. Furthermore, most techniques provide information only in a 2D frame, while obtaining a complete picture with 3D data is possible. Thus, in the last decades, the massive development of computer power allowed computational fluid dynamics (CFD) to become a feasible scientific tool for reacting flow studies. Studies related to the behavior of different fuel compositions or the optimization of existing combustion chambers are possible without constructing several test rigs or experiments.

The most accurate way to simulate turbulent flames using CFD is to solve numerically the equations coupling the flow and the chemistry related to combustion, with full-resolution of the flow and chemical time and length scales. However, this method, referred to as Direct Numerical Simulations (DNS), is not

feasible for practical combustion devices due to the wide range of the involved time and length scales requiring massive computational resources. Therefore, the DNS approach is limited to simple geometries, typically a small rectangular Cartesian domain where turbulent premixed flames propagate in the streamwise direction [12–16], or small-scale turbulent jet flames [17, 18], for fundamental investigations. For practical applications, the aforementioned set of equations is manipulated to overcome the difficulties related to turbulent eddies at small scales and the flow-flame interaction at small scales, reducing the range of solved scales and, consequently, the computational time. The resulting approaches are the Reynolds Averaged Navier-Stokes (RANS) and the Large Eddy Simulation (LES) methods. The resulting set of equations contains unclosed terms for the unresolved small-scales, which therefore need to be modeled. One of the main challenges of CFD is to develop suitable closure models whose performances can be validated against experimental results. Therefore, experimental and numerical methods need to be viewed as tools that need to work alongside to provide a complete scenario of combustion processes.

Turbulent Premixed Combustion

As compared with laminar flows, turbulent flows are characterized by randomness and irregularity that greatly enhance the mixing of different substances within a fluid. In most industrial applications, the mixing process needs to be fast. Thus, the preferred flow is turbulent. Based on the concepts introduced by Richardson [19], turbulence is composed of a wide range of eddies having different sizes and moving at different velocities, i.e., turbulent flows are characterized by a wide spectrum of lengths and time scales. The largest eddies are characterized by the integral length, l_0, and time, τ_0, scales. The smallest motions are characterized by the Kolmogorov length scale, $\eta = \nu^{3/4}/\epsilon^{1/4}$, where ϵ and ν represent the dissipation rate of turbulent kinetic energy and the kinematic viscosity, respectively. Correspondingly, the Kolmogorov time scale, $\tau_\eta = (\nu/\epsilon)^{1/2}$, can be defined. A key non-dimensional number in turbulent flows, characterizing the ratio of flow convection to diffusion at the integral scale, is the Reynolds number [20].

$$Re = \frac{l_0 u^{'}}{\nu} \tag{1.1}$$

where $u^{'}$ is the characteristic velocity at the integral scale.

Combustion processes refer to exothermic reactions where the fuel oxidizes due to the interaction with an oxidizer, and heat is released. Combustion pro-

cesses can be classified into non-premixed, premixed, and partially premixed combustion. In non-premixed combustion, the fuel and oxidizer are not mixed before the reaction. The chemical reactions occur in regions where the mixture composition is approximately at the stoichiometric condition, and therefore it is characterized by a high flame temperature. In non-premixed combustion, the flame temperature can not be easily controlled, leading to increased NO_x emissions. Therefore, in several devices, e.g., stationary gas turbines, premixed combustion is preferred. In fact, in these types of flames, the fuel and oxidizer are mixed before the reaction, and, therefore, it is possible to control the flame temperature through the fuel and oxidizer mass ratio in the mixture. There are also combustion processes where the fuel and oxidizer are partially premixed [21, 22]. This could be due to the short mixing time in the premixing chamber, such that the fuel and oxidizer could not mix sufficiently. In some cases, e.g., in a lifted jet flame, the fuel and oxidizer mix partially in front of the lifted flame, and the combustion process is considered to be a partially premixed one [22], or a fuel-rich premixed jet flame in ambient air, the flame is also partially premixed [23].

An important parameter used to describe the fuel and air mass ratio in premixed combustion is the equivalence ratio, defined as

$$\Phi = \frac{\dot{m}_{fuel}/\dot{m}_{oxidizer}}{(\dot{m}_{fuel}/\dot{m}_{oxidizer})_{stochiometric}} \tag{1.2}$$

$\Phi = 1$ indicates that the local mixture is at stoichiometric condition. $\Phi < 1$ and $\Phi > 1$ correspond to the fuel-lean and fuel-rich conditions, respectively.

Unlike in a non-premixed flame, where chemical reactions occur in the stoichiometric mixture, in premixed combustion, chemical reactions occur in the mixture of the given equivalence ratio. By using a fuel-lean mixture, the flame temperature is lower than that of a stoichiometric mixture. Thus, the thermal NO_x emission in a lean premixed flame is reduced.

In a premixed mixture, the flame is not controlled by mixing the fuel and the oxidizer. Instead, the reaction zone can propagate in the mixture. In laminar premixed flames, chemical reactions occur in a distinct zone characterized by a thickness, δ_L. The reaction zone propagates at a characteristic velocity referred to as the laminar flame speed, S_L. Figure 1.1 shows the inner structure of a premixed methane/air flame at $\Phi = 0.62$, which is represented by the distribution of mass fractions of a few selected species and of the temperature across the reaction zone. The results were computed using the Smooke-Giovangigli [24] mechanism. The flame can be divided into three different zones: the preheat zone, the reaction zone (which consists of an inner layer [25] where the fuel is

consumed, and an oxidation layer where the combustion intermediates such as CH_2O and CO are oxidized), and finally a postflame zone to the right of the oxidation zone. The inner layer is less than 1 mm in width, and it represents the location where most of the reactions occur [26]. Far upstream in the unburned mixture, the fuel and the air are perfectly mixed at room temperature. In the preheat zone, the temperature increases due to heat diffusion from the reaction zone. In this zone, no significant chemical reactions could occur since the temperature is below the cross-over ignition temperature. The temperature rises in the reaction zone where the fuel and oxidizer are consumed through chain branching and propagating reactions. These involve intermediate species such as CH_2O and OH radicals. The former is produced in the inner layer, and it is rapidly consumed in the oxidation zone by reacting with the radicals, i.e., OH.

Furthermore, temperature and major combustion products, i.e., CO_2, monotonically increase till the end of the oxidation zone. In the oxidation zone, the high-temperature level allows other reactions to occur. As a result, the OH concentration decreases while the CO_2 (not shown in the figure) increases. In the postflame zone, the reactions reach equilibrium.

The reaction zone propagates to the unburned mixture due to the diffusion of heat and hot gas to the unburned mixture. Such a process is often called deflagration wave propagation or simply a reacting wave propagation.

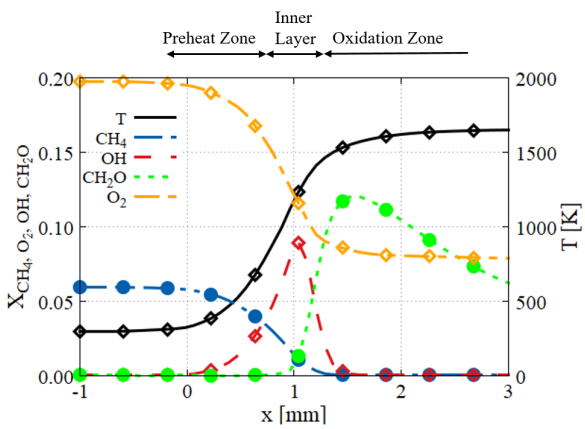

Figure 1.1: Overall structure of 1D methane/air premixed flame at $\Phi = 0.62$.

The propagation of a premixed flame in a turbulent environment introduces more scales that need to be considered. Several non-dimensional parameters have been proposed for a complete description of the phenomenon. Commonly used flame scales are the previously introduced S_L and δ_L and the laminar flame

residence time, $\tau_F = \delta_L / S_L$. The interaction of the flame with turbulence eddies at the integral and the small scales is described using the Damköhler and the Karlovitz numbers, respectively. Bearing in mind that $\epsilon = u^{'3}/l_0$ and $\nu = S_L \delta_L$, the Damköhler number can be defined as

$$Da = \frac{\tau_0}{\tau_F} = \frac{S_L l_0}{\delta_L u'} \tag{1.3}$$

which is the ratio of large eddy time to that of flame residence time and the overall chemical reaction time. The Karlovitz number is defined as [27],

$$Ka = \frac{\tau_F}{\tau_\eta} = \frac{u'^{3/2} \delta_L^{1/2}}{S_L^{3/2} l_0^{1/2}} \tag{1.4}$$

which is the ratio of the flame residence time to the time of the smallest eddies, the Kolmogorov time scale.

These dimensionless numbers historically inspired studies aiming to classify premixed flames into different regimes [25, 28–32]. The diagram proposed by Borghi [25] and later revised by Peters [32] is of general acceptance to describe the flame/flow interaction in a turbulent premixed flame, and it is shown in figure 1.2.

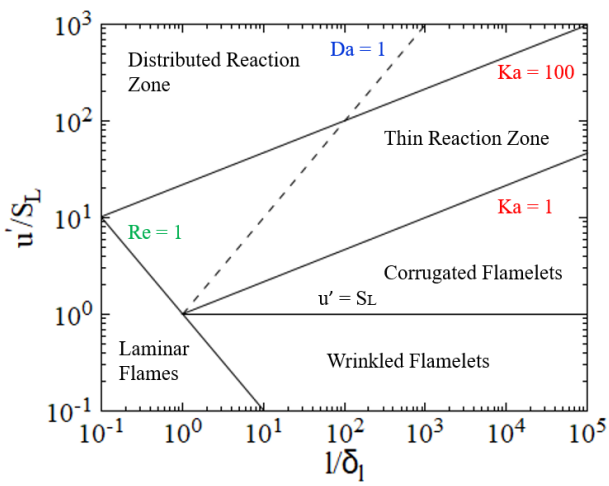

Figure 1.2: Regime diagram of turbulent premixed turbulent combustion.

As shown in Figure 1.2, laminar flames are defined for Re < 1, while the other regimes are referred to as turbulent flames. When Ka is below unity, the flame is considered a laminar flamelet since all turbulent eddies are larger than the

thickness of the flame, and the flame time is shorter than the time scales of all turbulent eddies. The flame is embedded in a range of turbulence eddies. In contrast, the local flame structure is similar to that of laminar flame, e.g., the one presented in Fig. 1.1. In other words, the flame is affected by turbulence only at scales that are larger than the flame thickness. Thus, the flames are wrinkled by turbulent eddies without disturbing their local structure. This flamelet regime can be divided into two sub-regimes based on the ratio $u^{'}/S_L$, the wrinkled flamelets regime and the corrugated flamelets regime. In both sub-regimes, turbulence wrinkles the flame front, but in the latter one, the intensity of turbulence is higher, and the flame structure is strongly affected by local eddy straining and stretching. Due to the extensive experimental [33–35] and numerical [36–39] results along with theory, this flamelets regime can be considered well understood.

Based on the definition proposed by Peters [27, 32], the thin reaction zone regime is defined for $1 < Ka < 100$. Here, turbulent scales are small enough to interact and distort the structure of the flame. In this regime, Kolmogorov eddies are smaller than the preheat zone of the flame but larger than the inner layer of the flame. Thus, turbulence eddies can distort the preheat zone of the flame without penetrating the inner layer. The interaction between the turbulence and the preheating zone of the flame is well-studied [40–43], but the effect of such interaction on the burning rate is less known. Since the turbulence eddies are unable to perturb the reaction layer, the flamelet concept is often used to model the thin reaction zone.

The distributed reaction zone regime, also referred to as the broken reaction zone regime [27, 32], is characterized by $Ka > 100$. In this regime, the Kolmogorov length scale is much smaller than the flame thickness; thus, the smallest turbulent eddies are expected to penetrate and disturb the inner reaction zone. Several authors have investigated this speculation recently, and different observations have been reported, with some experiments verifying the eddy distortion of inner layer structure [9, 10]. In contrast, other researchers report non-distortion of the inner layer [44–46]. Recent experimental and large eddy simulation studies have shown that distortion and non-distortion could occur at the same Karlovitz numbers depending on the burner length scales (and the integral length scales) [47–49]. Essentially, when small-scale eddies enter the preheat zone, the eddy scales become larger due to thermal expansion (dilation effect) and increased viscous dissipation. Local eddies (not that in the preheat zone based on which the Karlovitz number is defined) must remain smaller than the inner layer thickness to have a distortion of the inner layer.

The Borghi diagram represents a useful way to classify the flame regimes, but

the regime differentiation is based on qualitative analysis only. Furthermore, the regime diagram based only on the two parameters, l_0/δ_L and $u^{'}/S_L$, is not able to represent all the possible situations since there exist several parameters that affect the flow/flame interaction, e.g., the volume dilatation present in non-zero heat release flames. The single-step chemistry DNS results by Nilsson [50] show that two flames having the same Re, Ka, Da, S_L, $u^{'}/S_L$, δ_L and differing only by the density ratio between the unburned and the burned gas mixtures, propagate and appear differently. Thus, the Borghi diagram considers the differences between different fuels only through S_L and δ_L, although flames behave differently depending on the fuel composition properties. To account for these differences, it is possible to introduce another non-dimensional number, the Lewis number, defined as the thermal-to-mass diffusion speed ratio for each species. Mathematically,

$$Le_i = \frac{\lambda}{\rho c_p D_i} \tag{1.5}$$

where λ, c_p, and D_i represent the mixture averaged thermal conductivity, the mixture averaged heat capacity at constant pressure and the mass diffusion coefficient for specie i. Most of the species, e.g., CO, CO_2, CH_4, O_2 and N_2 have a $Le \approx 1$. Therefore it can be assumed to be equal to 1. However, other relevant species, e.g., H and H_2, are characterized by a Le that differs significantly from 1. Thus the previous simplification is no longer valid. A non-unity Lewis number highly influences the flame structure and appearance. This behavior is also called differential diffusion, and it represents a relevant phenomenon for hydrogen flames that results in a non-homogeneous equivalence ratio distribution.

Fuel flexibility and lean premixed combustion in gas turbine engines

The actual challenge for modern gas turbine engines is the demands of low emission (mainly CO_2 and NO_x) and fuel flexibility. These two requirements must be fulfilled without compromising the combustor's safety and efficiency. Although most of the existing gas turbines are designed to operate for natural gas or methane, a common way to reduce the CO_2 and NO_x emission simultaneously is to operate the existing combustor using low-carbon content fuels [51–54] under lean premixed or partially premixed conditions [55, 56]. This thesis mainly focuses on hydrogen and syngas within the range of the existing possible alternative fuels.

Hydrogen represents a desirable fuel due to the absence of carbon atoms in the molecule structure. Thus, no carbon chemistry is involved, thereby recognizing it as a possible solution to carbon dioxide emissions. However, burning pure hydrogen under lean premixed conditions can be rather challenging. Experimental observations [53, 57] showed that hydrogen tends to shift the burner operability range toward a leaner mixture. However, if, on the one hand, this matches well with the need for lean premixed combustion, it represents a considerable disadvantage in terms of flame stabilization. In fact, due to the high flame speed, hydrogen flames tend to be more prone to flashback, limiting the possible operability range. Based on the definition of turbulent premixed flame regimes introduced early in this chapter, the fundamental numerical analysis performed by Aspeden et al. [13] highlighted that hydrogen flames could no longer be considered in the thin reaction zone regime under the turbulence intensities typical of existing combustor devices. The DNS results from Carlsson et al. [14, 15] showed that the differential diffusion property of hydrogen introduces non-uniformities on the equivalence ratio distribution, introducing complexities in the overall flame behavior. Furthermore, the high product gas temperature of hydrogen flames can increase NO_x emission. Therefore, the blend of hydrogen with other fuels, e.g., methane, represents an excellent compromise to compensate for the drawbacks and complexities of using pure hydrogen [58, 59].

Synthetic gas, or syngas, represents an alternative energy source to natural gas in gas turbine applications. It presents combustion characteristics that match the combustor requirements [60]. Syngas is a combustible gas mixture that is mainly composed of CO and H_2 whose composition depends on the gasification process and the feedstocks, e.g., coal, biomass, or solid waste, used [61, 62]. Usually, impurities and a small number of light hydrocarbons, e.g., methane, are detectable in the syngas composition depending on the quality of raw materials and the production process. This makes the combustion characteristics sensitive to the syngas composition, and it can give rise to different flame characteristics, such as laminar flame speed [63–66], ignition delay time [67, 68], and flame extinction strain rate [69], affecting in a different manner the operating conditions of gas turbines [70]. Furthermore, as previously mentioned, the H_2 content in the fuel mixture significantly alters the range of operating conditions of gas turbine engines [71]. Therefore, syngas mixtures are often diluted, adding inert species, e.g., N_2, CO_2 and Ar to mitigate the propensity of the mixture to flashback and to reduce NO_x emissions [72, 73]. This thesis only focuses on testing different CO_2 dilutions levels. This represents one of the most promising inert species to reduce NO_x emissions due to its capability to participate in chemical reactions [74, 75]. This is due to carbon dioxide being able to lower the concentration of H and O atoms and CH radicals in the reaction zone [74, 76, 77]. This has been

proved in an experimental study reported by Williams et al. [78], where it was found that the CO_2 dilution on syngas mixture was very low (below two ppm). However, the participation of CO_2 in chemical reactions implies a shift in the lean blow-off limits compared to the pure syngas [79, 80].

Knowledge Gaps Addressed in the Thesis

Within the background set in the previous sections, some knowledge gaps have been identified and represent the motivation at the basis of this thesis. These gaps can be summarized as follows:

- Simulation of combustion processes in practical devices usually rely on models, i.e., G-equation [81] and FSD approach [82], that highly benefit from statistical information on fundamental quantities, such as displacement speed, especially at high Karlovitz number. Therefore, the statistical behavior of displacement speed has been of relevant importance in basic research works based on direct numerical simulations of reacting flows [83–94]. Furthermore, significant efforts have been spent on modeling the displacement speed as a function of the flame front curvature and the local flow strain rate [95–100]. However, most of these models have been derived in the context of flames weakly stretched. Thus, they are not suitable for predicting flame behavior under highly turbulent conditions where negative values on displacement speed are possible. Although recent studies [101, 102] provided a deeper understanding of the displacement speed and its correlations with its well-established decomposed parts [83, 103], the impact of the thermal expansion effect related to density varying reacting wave is not yet fully understood.

- A common way to stabilize flames in gas turbine engines is to use swirling flows. Due to the need to reduce the level of pollutant emissions, burners are operated under lean premixed conditions. However, lean flames tend to be prone to stability issues. Although it is well recognized that the usage of pilot flame improves the flame stabilization in gas turbine flames [104, 105], the interaction between pilot and main flame in terms of flow field and flame structure is yet not fully understood. Albrecht et al. [105] showed that using a non-premixed pilot flame improves the main flame stability. However, it has the drawback of increasing the amount of NO_x emissions. Thus, a question that naturally arises is what could be the difference between non-premixed and premixed pilot flames in terms of

emission. Furthermore, pilot flames are expected to improve the main flame stability by being able to burn as a stable flame. However, under turbulent conditions, pilot flames can experience fluctuation concerning the injection nozzle. Pilot flame stability is not thoroughly investigated.

- Although the recent increasing interest in using alternative fuels, such as hydrogen and syngas, for gas-turbine applications, few works in literature investigated their impact on the burner operability range [58, 106, 107]. Based on the discussion in the previous section, the different levels of hydrogen-enriching and inert dilution in the fuel mixture result in a wide range of possible flames. However, there is a lack of information on the flame structure distribution and the flow-flame interaction that motivates the work of this thesis.

Objective and Scope

The main objective of this thesis is to provide a deeper insight into the impact of using different fuels on turbulent premixed flames. This is accomplished from a fundamental standpoint using a numerical approach and on a more applied level in a model gas turbine combustor employing optical diagnostics. The scope and goals of the thesis throughout each paper are presented as follows.

In **Paper I**, a new set of equations describing the evolution of displacement speed, $\check{s}_d$, previously derived for constant density premixed flames under the assumption that (i) the reaction rate only depends on the progress variable describing the flames and (ii) the product between density and diffusivity is constant (see Ref. [101, 102]), is extended to density-varying premixed flames and numerically implemented. Furthermore, new equations describing flame dilatation and stretch rate are derived. The newly derived equations are used in DNS of a set of premixed turbulent flames having the same flame and turbulence characteristics with the exception of the density ratio between the fresh reactants and the exhaust gases. The goal is to isolate and understand the impact of thermal expansion caused by the density variations across the flames on the flame structures and displacement speed.

In **Paper II**, the pilot-main flame interaction as well as the impact of hydrogen-enriching of a turbulent premixed methane/air flame in a gas turbine-like swirl combustor is investigated under atmospheric pressure conditions. Two types of pilot flame configurations are employed: a non-premixed and a partially premixed pilot, both arranged in an annular shape around the main flame. The

fuel is premixed, and both pure and hydrogen-enriched (50% in vol.) methane /air mixtures are investigated. Laser-based experimental techniques are used in the investigations. The burner stability map is defined for each mixture with or without pilot flame employed, identifying the lean blow-off (LBO) and flashback (FBC) limits while varying the equivalence ratio. OH* Chemiluminescence images are used to extract quantitative statistics to assess how the flow and fuel composition affect the fluctuations of the pilot flame. Differences in the flame structure and stabilization in the combustor liner are qualitatively highlighted with simultaneous detection of OH and CH_2O radical species at stable main flame conditions. Furthermore, emissions at the burner exhaust are probed and analyzed.

Paper III is a continuation of **Paper II** and focuses on the flow details and a more detailed analysis of the flames. Here, the investigation of the effect of pilot and fuel composition is mainly concentrated on close-to-LBO conditions based on the findings shown in the previous paper. Furthermore, two different fuel and air flow rates are compared using a fully premixed pilot flame configuration. A qualitative and quantitative analysis using Particle Image Velocimetry (PIV) is performed to evaluate the impact of different pilot configurations on the velocity field. Furthermore, the pilot impacts on the flame structures are quantified regarding flame curvature and surface density, derived from OH Planar Induced Fluorescence (OH-PLIF) images. This investigation aims mainly to understand the behavior of different fuels under critical flame stabilization conditions.

In **Paper IV**, the surface temperature of the pilot flame nozzles used in **Paper II** and **III** was measured using lifetime phosphor thermometry with the ZnS:Ag phosphor. Three types of pilot flame configurations are employed: non-premixed and partially premixed (**Paper II**), and fully premixed (**Paper III**) pilot flames. Five combinations of pilot air and fuel flow rates routed from the main flame are investigated. The burner is operated with two levels of H_2 enrichment in methane/air mixture equal to 0% and 50% in volume basis. Due to the differences in stability limits, a comparison between the two mixtures is performed considering a value of equivalence ratio for each mixture located approximately at the same position in the stability map. This paper aims to understand the impact of fuel mixture and pilot flame control strategy on the burner nozzle temperature. This is achieved by accumulating sufficient samples on 33 points distributed at three different nozzle heights, spanning a quarter of the circular nozzle sector.

Paper V aims to provide a better understanding of the effect of carbon dioxide (CO_2) dilution on syngas flame combustion in a gas turbine-like combustion chamber. The burner employed in this investigation is the same as the one used

in Papers II, III and IV; however, no pilot flame is used here. The original composition of the syngas is 53% H_2 + 44% CO + 3% CH_4. Two different levels of CO_2 dilution (15% and 34% in volume basis) are studied. The CO_2 effect is analyzed primarily through its impact on the burner operability regime. Then, the dilution influence on the overall flame position in the combustion chamber and on the flame structure is investigated in more detail using optical techniques. Furthermore, a quantitative analysis of the exhaust emissions is performed. The explanation of the phenomena observed experimentally is supported by an extensive analysis of data from 1-D flame simulations.

The thesis is organized as follows. Chapter 2 presents the details of the numerical part of the work focusing on the impact of density variations on flame propagation. It defines the displacement speed parameter for a progress variable describing a premixed flame front. Furthermore, it introduces the isosurface-following derivative for the displacement speed, sub-terms, and the corresponding form for a density-varying flame. A description of the numerical methods and the performed simulations is also included. Chapter 3 summarizes the experimental techniques used in this thesis, briefly mentioning the fundamental principles behind them. Next, a general introduction to gas turbines and the lab-scale model investigated in this thesis is given in Chapter 4. Chapter 5 summarizes the key findings for each included paper. Conclusions and a future outlook are presented in Chapter 6, followed by Appendix A, containing the numerical definition of statistical tools, and Appendix B, describing how the quantitative data from OH-PLIF images have been extracted. Finally, the research papers included in this thesis are attached.

Chapter 2

Mathematical Description of Turbulent Premixed Flames

The propagation of a premixed flame (a reacting wave) in a turbulent environment is commonly modelled using a system of partial differential equations (PDEs). Depending on the type of problem that needs to be studied, a flame can be modelled differently. In this thesis, the flame is represented by a reaction front of nonzero thickness. An essential feature of premixed flames, for which there has been a surge of interest, is the displacement speed, S_d, and its decomposed terms. Here, a set of evolution equations for these quantities is used to investigate the role of thermal expansion on the propagation of a reaction surface. Direct numerical simulations (DNS) are used for diagnostics. Thus, the PDEs are solved numerically without using filters and averages. This chapter is divided into two sections. First, a mathematical description of the constitutive equations and the analytical derivation of the diagnostic equations are introduced. Next, the numerical approach and the simulated case setup are described.

Mathematical Description of Flow Governing Equations

The flow of Newtonian fluids is governed by a set of conservation equations for mass, momentum, and energy. The well-known Navier-Stokes equations describe

the conservation for the first two quantities as

$$\frac{\partial \rho}{\partial t} + \frac{\partial \rho u_i}{\partial x_i} = 0, \tag{2.1}$$

and

$$\frac{\partial \rho u_i}{\partial t} + \frac{\partial \rho u_i u_j}{\partial x_j} = -\frac{\partial p}{\partial x_i} + \frac{\partial \tau_{ij}}{\partial x_j}, \tag{2.2}$$

where t, u, and p denote time, velocity, and hydrodynamic pressure, respectively. The viscosity stress term, τ_{ij}, is expressed by

$$\tau_{ij} \equiv \mu \left(\frac{\partial u_i}{\partial x_j} + \frac{\partial u_j}{\partial x_i} - \frac{2}{3}\delta_{ij}\frac{u_k}{x_k} \right), \tag{2.3}$$

with μ being the dynamic viscosity and δ_{ij} the Kronecker delta. The energy conservation equation, written in terms of temperature [39], is expressed as follows

$$\rho C_p \frac{\partial T}{\partial t} + \rho C_p u_i \frac{\partial T}{\partial x_i} = \frac{\partial}{\partial x_i} \left(\rho C_p \mathcal{D}_T \frac{\partial T}{\partial x_i} \right) + E_T + \mathbb{W}_T \tag{2.4}$$

where T, C_p, $\mathcal{D}_T$, E_T and $\mathbb{W}_T$ represent temperature, heat capacity at constant presume, the thermal diffusivity, the heat transfer due to species diffusion and the reaction rate term, respectively.

Mathematical Description of Turbulent Premixed Flames

Simulation of a premixed flame required the description of the combustion process. A possible way is to use a finite-thickness flame that propagates due to chemical reactions. The description of the local chemical state often employs a reaction progress variable, c, [108] whose transport equation can be defined by the following convection-diffusion-reaction equation:

$$\frac{\partial c}{\partial t} + \boldsymbol{u} \cdot \frac{\partial c}{\partial x_i} = \mathbb{D} + \mathbb{W}, \tag{2.5}$$

where t, $\boldsymbol{u}$, $\mathbb{D}$, and $\mathbb{W}$ denote time, velocity, diffusion term, and reaction rate term, respectively. The last two terms need to be modelled depending on the complexity of the problem.

In this thesis, the chemistry related to the combustion is described by a single-step reaction, meaning that the chemical conversion from reactants to products occurs without passing through intermediate radicals. Under this assumption, the reaction progress variable introduced above varies from 0 for pure reactants

and 1 for products, and it depends only on the spatial coordinates, $\boldsymbol{x}$, and the time, t. In Eq. 2.5, the diffusion term is modelled using Fick's law

$$\mathbb{D} = \frac{1}{\rho}\frac{\partial}{\partial x_i}\left(\rho\mathcal{D}\frac{\partial c}{\partial x_i}\right), \tag{2.6}$$

where ρ and $\mathcal{D}$ are the density and diffusivity, respectively. The reaction term is represented by the following expression:

$$\mathbb{W} = \frac{1}{(1+\theta)^s}\frac{1-c}{\tau_R}\exp\left[-\frac{Ze(1+\theta)^2}{\theta(1+\theta c)}\right], \tag{2.7}$$

where τ_R is a time scale, Ze the Zeldovich number, and s and θ are two constants set as follows:

$$s = \begin{cases} 1, & \text{if } \Theta = 1 \\ 0, & \text{if } \Theta > 1 \end{cases} \quad \text{and} \quad \theta = \begin{cases} 6, & \text{if } \Theta = 1 \\ \Theta - 1, & \text{if } \Theta > 1 \end{cases}. \tag{2.8}$$

where Θ is the density ratio between the unburned and burned side of the mixture, ρ_u/ρ_b. The equation 2.7, already used in Ref. [102], represents the general form for density varying reacting waves of the corresponding expression introduced by Elperin et al. [109], and used for constant density waves simulations. This equation is selected to mimic the highly nonlinear dependence of the reaction rate term on the progress variable, c, in a premixed flame, for constant density simulations. The Zeldovich number is defined as $Ze = E_a(T_b - T_u)/RT_b^2$, where E_a, T_b, T_u and R representing the activation energy of the fuel, the temperature of the burned mixture, the temperature of the fresh reactants and the ideal gas constant, and it is set equal to 6 in this thesis, following the value used in Ref. [109]. The time scale τ_R is determined in a pre-simulation of a planar 1D laminar reaction wave and it is set equal to constant. The assumption of $Le = 1$, implying that $\mathcal{D}_T/\mathcal{D} = 1$, gives the opportunity to discard one between the energy and transport equations for c, if there are no other sources of heat than the chemical reactions.

Derivation of the Displacement Speed Surface-Following Evolution Equation

The displacement speed, S_d represents a relevant quantity in combustion literature. This is a local quantity that describes the self-propagation speed of a local scalar isosurface due to the effect of diffusion and reaction at any point

$(\boldsymbol{x}, t)$ with $0 < c(\boldsymbol{x}, t) < 1$ [110, 111]. Based on [112], the displacement speed can be defined as

$$S_d = \frac{\mathbb{D} + \mathbb{W}}{|\nabla c|} \tag{2.9}$$

where $|\nabla c|$ is the surface-averaged flame thickness marker. Furthermore, S_d represents a key part of the "total" velocity

$$\boldsymbol{u}^* = \boldsymbol{u} - S_d \boldsymbol{n} \tag{2.10}$$

where $\boldsymbol{u}$ is the local velocity, $S_d \boldsymbol{n}$ is self-propagation velocity, and $\boldsymbol{n} \equiv \nabla c / |\nabla c|$ is normal to a c isosurface passing the local point $(\boldsymbol{x}, t)$. The "total" velocity traces a moving point on an isosurface. Furthermore, it is possible to define the isosurface-following time derivative operator for a generic quantity $\phi(x, t)$ as

$$\partial_t^* \phi = \frac{\partial^* \phi}{\partial^* t} = \frac{\partial}{\partial t}\phi + \boldsymbol{u}^* \frac{\partial \phi}{\partial x_i} \tag{2.11}$$

The displacement speed is usually defined as the sum of four different terms [113–116], as

$$S_d = \frac{\mathbb{D} + \mathbb{W}}{|\nabla c|} = S_d^c + S_d^n + S_d^W + S_d^o \tag{2.12}$$

These terms are defined as:

- Contribution from tangential (curvature) diffusion

$$S_d^c = \mathcal{D} \nabla \cdot \boldsymbol{n} = \frac{\mathcal{D}(\nabla^2 c - \nabla_n \nabla_n c)}{|\nabla c|} \tag{2.13}$$

- Contribution from normal diffusion

$$S_d^n = \frac{\mathcal{D} \nabla_n \nabla_n c}{|\nabla c|} \tag{2.14}$$

- Contribution from reactions

$$S_d^{\mathbb{W}} = \frac{\mathbb{W}}{|\nabla c|} \tag{2.15}$$

- Contribution from the variation of viscosity across the flame

$$S_d^o = \frac{1}{\rho} \nabla_n (\rho \mathcal{D}) \tag{2.16}$$

with $\nabla \cdot \boldsymbol{n} = \nabla c/|\nabla c|$ representing the local curvature. This thesis assumes that the term $\rho\mathcal{D}$ is constant. As a consequence, the last contribution vanishes.

Noticing that $|\nabla c|$ appears at the denominator of each quantity within the group $\phi \in \Phi = \{1/|\nabla c|, \nabla \cdot \boldsymbol{n}, S_d^n/\mathcal{D}, S_d^W, S_d\}$, it is possible to define the isosurface-following derivative for each of the quantity ϕ using the general form of

$$\partial_t^* \phi = \underbrace{-\phi \partial_t^*(ln|\nabla c|)}_{\mathbb{A}(\phi)} + \underbrace{\frac{1}{|\nabla c|}\partial_t^*(\phi|\nabla c|)}_{\mathbb{B}(\phi)} \tag{2.17}$$

where $\mathbb{A}$ is the contribution from the surface-following rate of change, i.e., the increase/decrease of the distance between the neighbouring isosurfaces in the denominator $|\nabla c|$, and $\mathbb{B}$ is the effect of the isosurface surface-following rate of change in diffusion inside of $\phi|\nabla c|$ [117]. Term $\mathbb{A}(\phi)$ can be further divided into three parts as follows:

$$\mathbb{A}(\phi) = -\phi\mathcal{K} + \phi\nabla \cdot \boldsymbol{u} - \phi\nabla \cdot S_d\boldsymbol{n}, \tag{2.18}$$

obtained plugging the following transport equation from Ref. [39, 82] for $|\nabla c|$

$$\partial_t^*(ln|\nabla c|) = \frac{1}{|\nabla c|}\partial_t^*(|\nabla c|) = \mathcal{K} - \nabla \cdot \boldsymbol{u} + \nabla(\cdot S_d\boldsymbol{n}), \tag{2.19}$$

into the first term of 2.17. Here, $\mathcal{K} = a_t - S_d\nabla \cdot \boldsymbol{n}$ identifies the stretch rate [82, 118], $a_t = \nabla \cdot \boldsymbol{u} - a_n$ the tangential strain rate and $a_n = n_i n_j \nabla_j u_i$ is the normal strain rate.

On the other hand, the term $\mathbb{B}(\phi)$ represents the effect of the isosurface following the rate of change in the "diffusion" contained inside $(\phi|\nabla c|)$. It is shown [102] that the term $\mathbb{B}$ for the quantities $\nabla\boldsymbol{n}$, $S_d^n/\mathcal{D}$ and $S_d^{\mathbb{W}}$ can be written respectively as,

- Contribution from tangential (curvature) diffusion

$$\mathbb{B}(\nabla\boldsymbol{n}) = -\boldsymbol{n}\cdot\nabla^2\boldsymbol{u} - 2S_{ij}\nabla_j n_i + \nabla_n a_n + \nabla^2 S_d - n_i n_j \nabla_i \nabla_j S_d + S_d \nabla_i n_j \nabla_j n_i \tag{2.20}$$

- Contribution from normal diffusion

$$\mathbb{B}(S_d^n/\mathcal{D}) = -2S_{ij}n_j\nabla_i \ln|\nabla c| - \nabla_n a_n + n_i n_j \nabla_i \nabla_j S_d + 2\nabla S_d \cdot \nabla(\ln|\nabla c|) + S_d(\nabla_i n_j - \nabla_j n_i)\nabla_i n_j \tag{2.21}$$

- Contribution from reactions

$$\mathbb{B}(S_d^{\mathbb{W}}) = 0 \tag{2.22}$$

this due to the assumption $\mathbb{W}$ inside Eq. 2.15 solely depends on c, see Eq. 2.7.

Regarding the remaining quantity S_d, assuming $\rho\mathcal{D}$ = constant and $\mathcal{D}$ solely depending on c, $\mathbb{B}(S_d)$ can be written as

$$\mathbb{B}(S_d) = \frac{\mathcal{D}}{|\nabla c|}\partial_t^*(\nabla^2 c) = -\mathcal{D}\boldsymbol{n}\cdot\nabla^2\boldsymbol{u} - 2\mathcal{D}\frac{\nabla\nabla c : \boldsymbol{\nabla u}}{|\nabla c|} + \mathcal{D}\nabla^2 S_d - 2\mathcal{D}\nabla S_d\cdot\nabla(\ln|\nabla c|) - \mathcal{D}S_d\boldsymbol{n}\cdot\nabla^2\boldsymbol{n}. \tag{2.23}$$

However, under the assumption of $\rho\mathcal{D}$ = constant, the simplified decomposition introduced in Eq. 2.12, also holds for terms $\mathbb{A}$ and $\mathbb{B}$ as

$$\begin{aligned}\mathbb{A}(S_d) &= \mathcal{D}\mathbb{A}(\nabla\cdot\boldsymbol{n}) + \mathcal{D}\mathbb{A}(S_d^n/\mathcal{D}) + \mathbb{A}(S_d^W)\\ \mathbb{B}(S_d) &= \mathcal{D}\mathbb{B}(\nabla\cdot\boldsymbol{n}) + \mathcal{D}\mathbb{B}(S_d^n/\mathcal{D}) + \mathbb{B}(S_d^W).\end{aligned} \tag{2.24}$$

Density-Weighted Displacement Speed, Dilatation and Curvature Induced Stretch Rate Definitions

It is important to notice that the decomposition introduced in equation 2.17, as well as the definitions of $\mathbb{A}(\phi)$ and $\mathbb{B}(\phi)$, are still valid [102] for any quantity that can be written in the form of $\psi = F(c)\phi_1 + G(c)\phi_2$, thus $\mathbb{A}(\psi) = F(c)\mathbb{A}(\phi_1) + G(c)\mathbb{A}(\phi_2)$ and $\mathbb{B}(\psi) = F(c)\mathbb{B}(\phi_1) + G(c)\mathbb{B}(\phi_2)$. Within this framework, it is possible to define the density-weighted displacement speed, which represents a useful parameter to discuss the thermal-expansion-enabled flames. From the assumption of $\rho\mathcal{D}$ = constant, thus $\rho_u\mathcal{D}_u$ = constant, with ρ_u and $\mathcal{D}_u$ being density and diffusivity of the unburned reactant mixture, a decomposition similar to Eq. 2.12 holds as

$$\check{s}_d = \mathcal{D}_u\nabla\cdot\boldsymbol{n} + \check{s}_d^n + \check{s}_d^W, \tag{2.25}$$

where the density-weighted displacement speed and its parts are defined as $\check{s}_d \equiv \frac{\rho}{\rho_u}S_d$, $\check{s}_d^n \equiv \frac{\rho}{\rho_u}S_d^n$ and $\check{s}_d^W \equiv \frac{\rho}{\rho_u}S_d^W$, and assuming ρ a function of solely c (thus,

$\mathcal{D}$ being inversely proportional to ρ and also solely depending on c as well), Equation 2.17 is valid for $\check{s}_d$ and its parts, $\phi \in \Phi \cup \{\check{s}_d, \check{s}_d^n, \check{s}_d^W, \check{s}_d^n + \check{s}_d^W\}$.

Holding the assumption of $\rho = \rho(c)$, it appears that

$$\nabla \cdot \boldsymbol{u} = -\frac{1}{\rho}\left(\frac{\partial \rho}{\partial t} + \mathbf{u}\nabla\rho\right) = -\frac{1}{\rho}\frac{\partial \rho}{\partial c}(\mathbb{D} + \mathbb{W}), \tag{2.26}$$

that can be used to link $\mathbb{B}(\check{s}_d) = \frac{\rho}{\rho_u}\mathbb{B}(S_d)$ to the rate of change in dilatation, through

$$\partial_t^*(\nabla \cdot \boldsymbol{u}) = -\left(\frac{|\nabla c|}{\rho_u}\frac{\partial \rho}{\partial c}\right)\mathbb{B}(\check{s}_d). \tag{2.27}$$

This expression vanishes whereas a constant-density flame is considered, since $\partial\rho/\partial c = 0$.

Based on the definition of the curvature-induced stretch rate as

$$\mathcal{K}_c = -\check{s}_d \nabla \cdot \boldsymbol{n} = \mathcal{K} - a_t \tag{2.28}$$

the related transport equation becomes

$$\partial_t^* \mathcal{K}_c = -\check{s}_d \partial_t^*(\nabla \cdot \boldsymbol{n}) - (\nabla \cdot \boldsymbol{n})\partial_t^* \check{s}_d \tag{2.29}$$

Note that the right-hand side of Eq. 2.29 contains the isosurface-following time derivatives of $\nabla \cdot \boldsymbol{n}$ and $\check{s}_d$. So, the latter can be further expanded by substituting the corresponding forms of Eq. 2.17 in it. It is worth pointing out that the stretch rate represents the rate of change in an area of an infinitesimal small element ($\mathrm{d}s$) of an iso-scalar surface

$$\mathcal{K} = \frac{1}{\mathrm{d}s}\partial_t^*(\mathrm{d}s). \tag{2.30}$$

Thus, values of $\mathcal{K} > 0$ can be related to the creation of small isosurface elements, while values of $\mathcal{K} < 0$ to the destruction event of them [119].

Numerical Methods

The governing equations for mass (Eq. 2.1) and momentum (Eq. 2.2) and the evolution equation for the progress variable c (Eq. 2.5) are solved using an in-

house DNS code for low Mach number reacting flows. A detailed description can be found in Ref. [120].

The Cartesian grid approach is used for spatial discretization, defining the scalar at the center of each cell and the velocity at the surface. All the terms involving spatial derivatives are discretized using a 6^{th}-order polynomial interpolation, with the only exception of the convection term for which a 5^{th}-order weighted essentially non-oscillatory (WENO) scheme [121] is used to avoid numerical overshooting. The Poisson equation for pressure differences is solved using Gauss-Seidel iterations with a multi-grid acceleration approach [122]. Temporal integration is performed explicitly. Time advancement proceeds using multiple ($K > 1$) sub-time steps ($\Delta t/K$), starting from an initial Runge-Kutta step and followed by Adam-Bashfort steps, as described in Ref. [102]. The overall time step is limited by the CFL condition.

To keep the computational cost reasonable, turbulence in DNS solvers is generated and maintained through an artificial source term added at the right-hand side of the momentum equation. Two are the most commonly used: the linear [123, 124] and the low-wavenumber [125] forcing. In this thesis, the second approach is used, which is based on the injection of energy to the large turbulence scales at the same rate at which the smaller turbulence eddies dissipate it. In this way, the turbulent kinetic energy is maintained. The forcing term is defined as $\boldsymbol{f}_u(\boldsymbol{x}, t) = \sum_k \hat{\boldsymbol{f}}_k(t) \exp(i\boldsymbol{k} \cdot \boldsymbol{x})$ [126], where

$$\hat{\boldsymbol{f}}_k(t) = \frac{\langle \epsilon \rangle \boldsymbol{l}_{\boldsymbol{k}-\boldsymbol{k_r(t)}}}{2k_f(t)} \hat{\boldsymbol{u}}_{\boldsymbol{k}}(t) \tag{2.31}$$

where $\epsilon = 2\nu S_{ij} S_{ji}$ represents the dissipation rate, the brackets $\langle \cdot \rangle$ are the averaging over the entire domain and $\hat{\boldsymbol{u}}_{\boldsymbol{k}}(t)$ represents the Fourier transform of the velocity. The function $\boldsymbol{l}_{\boldsymbol{k}-\boldsymbol{k_r(t)}}$ is stochastic; at each time step, it is 1 for a randomly selected wavenumber in the range $|k| \leq k_f$ and 0 elsewhere. The k_f parameter represents the cut-off wavenumber which is the largest wavenumber that receives energy from the forcing. The denominator in expression 2.31, $k_f(t) = \sum_{|k| \leq k_f} \hat{u}_{\boldsymbol{k}} \cdot \hat{u}_{\boldsymbol{k}}/2$, express the kinetic energy contained in modes having wave numbers $|k| \leq k_f$. The inverse Fourier transform of Eq.2.31 returns the forcing source term in physical space.

To take into account the density variation across the flame, the aforementioned forcing factor is multiplied by a density coefficient as $\boldsymbol{f} \equiv (\rho/\rho_u)\, \boldsymbol{f}_u$, where ρ and ρ_u represent the density of the gas at a generic location of the flow and of the unburned gas. The factor (ρ/ρ_u) reduces the amount of energy injected at low wavenumbers on the burned side of a density-varying flame. This retains (i)

the turbulence decay due to the increased kinematic viscosity ($\nu \equiv \mu/\rho$) toward the combustion products and (ii) the thermal-expansion turbulence inhibition.

DNS Set-up

DNS simulations are designed to let the flame front evolve in a rectangular box (size $\Lambda_x \times \Lambda \times \Lambda$), discretized on a uniform Cartesian grid. In addition to the density-varying reaction front, a data set for constant density flame is acquired as a reference. For this simulation, periodic boundary conditions are described in the transverse direction as well as in the stream-wise direction. This since the flow is not affected by the wave propagation. Therefore, when the wave reaches the left boundary of the computational domain, as identical reaction wave enters the domain through its right boundary. This method greatly improves sampling of statistics by several cycles of the wave propagation through the computational domain. Since this method is valid for constant density reaction waves only, for all the density-varying cases, periodic boundary conditions are described in the transverse direction, while inlet and outlet conditions are used in the stream-wise direction. An initial turbulent field is synthesized with an rms velocity u_0 and an integral length scale $l_0 = \Lambda/4$, inside the bold-line box in Figure 2.1 (i.e., $\forall x, y, z \in [0, \Lambda]$) till reaching the homogeneous-isotropic state, and then let it freed to propagate throughout the computational domain. The flow inside the cubic-box region always resembles a standalone simulation of periodic constant-density turbulence during the run ($\rho = \rho_u$ and $c = 0$, here). Turbulence is maintained integrating Eq. 2.2 keeping the same rms velocity $u'(t) \approx u_0$. A pre-computed planar premixed flame is released at $x_0 = X_T = 0.6\Lambda_x$ within the turbulent environment at the beginning of each simulation. To keep the flame staying inside the computational domain, equations 2.1, 2.2, and 2.5 are solved on an observation coordinate moving with an adjustable x-component velocity. This value is controlled using so-called proportional-integral-derivative (PID) methods. Further details can be found in Refs. [102, 127].

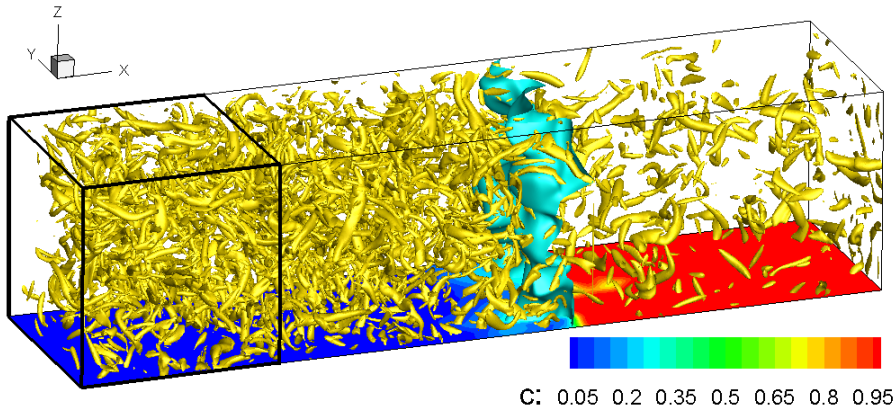

Figure 2.1: 3D snapshots of case B. The c-field is shown on the bottom plane with an isosurface of $\hat{c} = 0.3$ (cyan) and rotating flow structures are visualized using yellow iso-contours of the second eigenvalue of the flow strain rate tensor (also referred to as "Lambda2-vortex method" [128]).

Chapter 3

Experimental Methodology

In this thesis, several experimental techniques are used to characterize premixed combustion under gas turbine-like conditions. This chapter overviews the optical diagnostic techniques used in this work, briefly introducing their physical background and the equipment employed.

Planar Laser Induced-Fluorescence (PLIF)

Laser-induced fluorescence (LIF) is a resonant optical spectroscopic technique widely used in the combustion diagnostic field mainly for the detection of species concentration but also for temperature measurements [129]. The principle of LIF is generally composed of two different steps. In the first, atoms and molecules are excited from the ground energy state to a higher energy state (excited state) by an external energy source (laser). In the second step, several processes can take place, i.e., molecules can absorb the energy and reach an even higher energy state, or they can lose energy due to collisions between each other or even absorb energy and dissociate into small fragments. However, a phenomenon detected and used for combustion diagnostic purposes is the emitted fluorescence from the excited atoms or molecules when returning to their ground state. A schematic representing the LIF process for a diatomic molecule (e.g., NO, NH, OH, etc.) is shown in Figure 3.1. Further details can be found in Ref. [130].

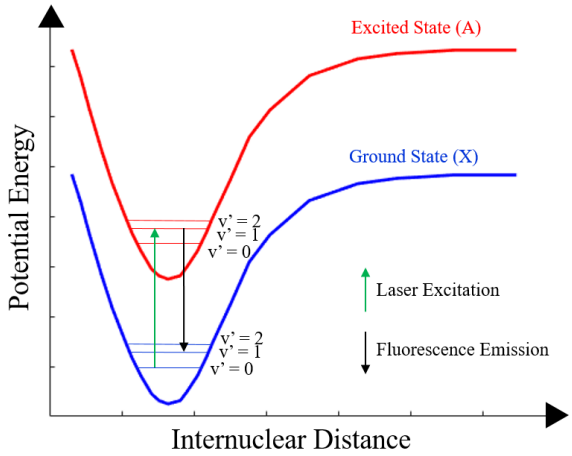

Figure 3.1: Schematic for laser-induced fluorescence process for diatomic molecules.

For 2D visualization, the laser beam is expanded through a sheet forming optics made of a series of optical lenses aiming to collide with the target area of investigation. The fluorescence signal may have the same or a longer wavelength than the exciting laser beam. Such a shift is used to avoid or reduce the scattered light. However, the gated intensified CCD camera used to collect the LIF signal is often equipped with a filter placed in front of it to suppress the acquisition of scattered light.

Thanks to the high spatial (up to $\approx 40\ \mu m$) and temporal ($\approx 10\ ns$) resolution [131], this technique represents a useful diagnostic tool for combustion experiments. However, since it is a species-specific technique, the exciting signal must be tuned to a specific wavelength for the selected species. Based on chemical kinetic results (see Figure 1.1) and experimental observations [132, 133], there exist several intermediate species whose distribution can provide helpful insight into the flame structure. It is well known that the OH concentration is highest in the reaction layer of a premixed flame, decaying in the post-flame zone. Thus, it represents a good marker for the flame front and the post-flame region. At the same time, CH_2O is mainly detected in the preheat and the heat release zones [131]. Therefore, the overlap between the detected signals from these two species can provide the overall spatial distribution of the investigated premixed flame front.

Within the frame of this thesis, both OH (in **Papers II-V**) and CH_2O (in **Paper II**) -PLIFs are used as diagnostic tools. Regarding OH, this represents a spectroscopically well-characterized radical for which the two schemes $A^2\Sigma^+(v' =$

1) $\leftarrow X^2\Pi(v'' = 0)$ (also called Q1(8)) and $A^2\Sigma^+(v' = 0) \leftarrow X^2\Pi(v'' = 0)$ are mainly used to excite the energy state transition and to collect the resulting fluorescence. In this thesis, the Q1(8) transition is excited with a laser beam tuned at a wavelength of 283 nm. A proper laser beam is generated using a frequency-double (532 nm) Nd:YAG laser pumping a dye laser tuned at 283 nm. The Q1(8) transition is usually chosen in the combustion framework due to its strong signal and almost temperature-insensibility over a temperature range from 1400 K to 2500 K. The resulting signal is collected using an ICCD camera with an extended pass filter. Regarding the CH_2O-PLIF, formaldehyde spectroscopy is relatively complicated due to the different possible vibrational states and the geometrical changes of molecules in excited states. Formaldehyde has several suitable bands for excitation within the range of 270 nm and 360 nm. Furthermore, the excitation states are more populated as the temperature increases. Therefore, due to the complexity of the absorption spectrum, in this thesis, the technique relies on the excitation at the 355 nm wavelength of the 4_0^1 band of the electronic transition $A^1A_2 \rightarrow X^1A_1$. The same approach is used in previous works [131, 134, 135]. A laser beam of 355 nm wavelength is produced using the third harmonic of an Nd:YAG laser, and the fluorescence signal is collected using an ICCD camera equipped with a long pass filter.

Particle Image Velocimetry (PIV)

The study of the flow field is of relevant interest to better understand the flame-flow interaction. In most practical combustors, e.g., gas turbines or internal combustion engines, there exists a need to quantify the flow field to understand processes like flame stabilization [136]. Furthermore, experimental data showing the flow field are needed for CFD validation. Within this framework, Particle Image Velocimetry (PIV) represents a typical, suitable technique for velocity field measurements in both gaseous and liquid fluids. Furthermore, the data provided by PIV is extra valuable if it is collected simultaneously with other methods, e.g., OH-PLIF, for simultaneous visualization of flow and species fields. Figure 3.2 shows a generic schematic for PIV measurement. The technique involves acquiring a sequence of the Mie scattered signals from an illuminated flow seeded with proper particles. In principle, all strong enough light sources are suitable, but dual-pulsed laser systems are often used for illumination. The delay between the two pulses should be adjusted based on the velocity range of interest, and it needs to be unable to detect a substantial motion of the particles. The velocity field is derived by tracking the movement of particles between two consecutive frames. Each of these is firstly divided into

small sub-windows called interrogation areas (IA). The IA are cross-correlated pixel by pixel for each couple of consecutive frames that identify the particle displacement. Then, by repeating the procedure for each IA over the image frame and knowing the time delay between the frame, it is possible to derive the 2D velocity distribution [137]. In set-ups similar to the work presented in this thesis, the laser sheet thickness is between 0.5 and 1 mm, while the laser pulse is $\approx$ 10 ns. Another relevant parameter to consider is the size of the seeding particles; their size should be sufficiently small to follow the flow motion but big enough to be detected and recorded. The particle density should be relatively high and uniform. To ensure good results, the number of particles in each AI should be approximately fifteen [138].

In this thesis, the PIV system consists of a high-speed dual cavity Nd:YLF laser tuned at a wavelength of 527 nm with a frequency of 1 kHz. Similarly to OH- and CH_2O-PLIF, the laser beams are expanded through laser forming optics and guided toward the flame center line. A PIV post-processing algorithm is selected to adjust the IA size best to handle varying local particle densities.

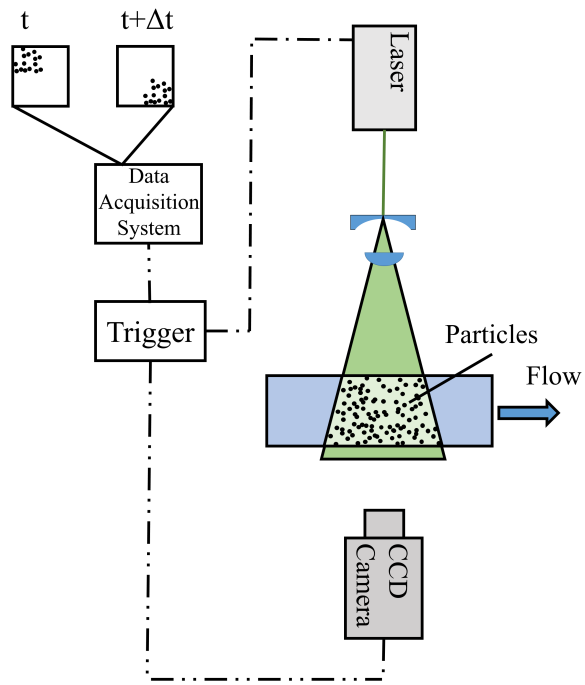

Figure 3.2: Schematic for a generic particle image velocimetry (PIV) set-up.

OH* Chemiluminescence

Chemiluminescence represents one of the possible ways through which a flame can spontaneously emit electromagnetic radiation [139]. Atoms, molecules, or radicals excited by the chemical reactions emit this radiation when decaying from the excited state to the ground state. The emitted radiation is characterized by a radiation spectrum that is relatively continuous for complex molecules. However, in the case of simple molecules, e.g., diatomic molecules, the spectrum shows a distinctive peak (and a few smaller ones). For example, the OH species in the excited state (OH*) indicates a dominant peak at 310 nm in the UV region. The strength of the radiation at a specific wavelength is proportional to the concentration of the related excited molecules. Thus, measuring the emitted radiation can indicate the concentration of the excited molecules. Furthermore, since chemiluminescence originates from the reaction zone, it should be possible to acquire the signal to characterize the heat release of the flame [140]. However, due to the line-of-sight nature of this technique, it is difficult to get reliable values for concentration and heat release. Nevertheless, flame chemiluminescence represents a suitable way to visualize the flame position and fluctuation. In this thesis, flame chemiluminescence is acquired using a high-speed CCD camera equipped with an intensifier and an OH^* filter. The repetition rate is set to 1 kHZ to capture the flame dynamics.

Combustion Emission Species Detection

The analysis of the species emitted at the exhaust represents a reliable technique to understand the impact of using different fuels on pollutant emissions. Furthermore, coupled with other methods, it can provide a complete overview of the proceeding of the combustion process (see **Paper II** and **V**). In this thesis, emissions are collected at the exhaust of the burner with a sampling rate of 1Hz. A water-cooled gas sample probe equipped with eight holes is used to extract gases after combustion. The probed gases pass through a condenser to remove the water before reaching an emission rack calibrated adequately before each acquisition. Here, emission levels are analyzed and displayed in real-time. More details about the gas sample probe can be found in the user manual [141].

Chapter 4

Gas Turbine Model Combustor – CeCOST Burner

Gas turbines for stationary applications (electricity generation) consist of a sequence of three main sections: a compressor, a combustor and a turbine. The intake air compressed to a high pressure by the compressors enters the combustion system, mixed with fuels and combusted. The exhaust gases enter the turbine, where they expand. The resulting mechanical energy is used to drive the compressor and to move a generator for electric energy production. This chapter provides an overview of the characteristic features of gas turbine combustors, focusing mainly on swirl burners. After the theoretical framework, the model gas turbine burner studied in this thesis, also called CeCOST Burner, is introduced.

Swirl Combustor Characteristics

The flame anchoring and stabilization in the liner play a crucial role in the correct operation of gas turbine combustors. Several possible flame-holding approaches exist, e.g., swirl pilot flames and bluff bodies [39]. The burner discussed in this thesis uses the swirl stabilization process, widely used for premixed flames in modern gas turbine combustor applications [142–144]. This method leads to a compact flame, fast mixing process, no flow counteract with solid surfaces and to potentially reduced emissions. The latter advantage is possible since swirl burners give the opportunity to burn premixed fuel/air mixtures at lean flame conditions. However, due to the complexities related to the flow structure and to

turbulence–flame interactions, swirling flames tend to be more prone to stabilization problems. Figure 4.1 shows the time-averaged flow streamlines overlapped with the time-averaged velocity field from planar PIV measurements, representing the typical flow structure in a gas turbine swirling flame. The mechanism behind the flame stabilization through swirling flows is the formation of a central toroidal recirculation zone (also called Inner Recirculation Zone - IRZ) downstream of the burner nozzle, which recirculates active chemical species and heat to the flame root, helping the ignition of the fresh mixture. As a results of the recirculation zone, a region with zero or nearly zero axial velocity is formed. Here is where the turbulent flame velocity can match the flow velocity and where the flame may stabilize. The incoming (swirling) fuel/air radially expands, causing a pressure gradient along the centre line. This, together with the conservation of angular momentum, creates a recirculation of the flow in the center, forming the IRZ. If the flame is confined, an Outer Recirculation Zone (ORZ) becomes very visible. Shear layers are formed at the edge between the IRZ and the ORZ, indicated by the colour gradients in Figure 4.1. The vortex breakdown phenomenon may lead to a precessing vortex core (PVC), a 3D large-scale unsteady structure localized either at the edge of the IRZ or in the center (vortex core) [145]. The central recirculation zone strength and its position are found to be essential for flame stabilization [143, 146].

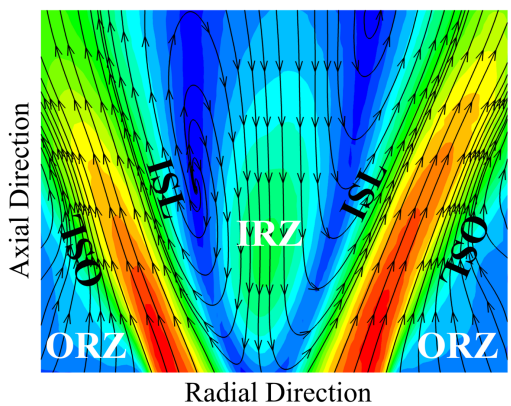

Figure 4.1: 2D time-averaged velocity streamlines overlapped to the mean velocity field showing the flow typical reversed cone shape in swirl burners. IRZ, ORZ, ISL, and OSL indicate the location of the inner and outer recirculation zones and the inner and outer shear layers, respectively.

It is important to mention that the occurrence of vortex breakdown is strongly related to the swirl level, which needs to be sufficiently high. This is estimated using the reduced swirl number, S, [147] defined as the ratio between the axial flux of tangential momentum and the axial flux of axial momentum normalized by the radius, Eq. 4.1,

$$S = \frac{\int_0^R \bar{U}_{ax}(r)\bar{U}_{\theta}(r)r^2 dr}{R\int_0^R \bar{U}_{ax}^2(r)r dr} \tag{4.1}$$

where R, $\bar{U}_{ax}$, $\bar{U}_{\theta}$ represent the nozzle radius, the time-averaged radial profile of axial and tangential velocity components, respectively.

Burner stability

Modern gas turbines are requested to operate within a wide range of parameters that vary depending on operating demands. Furthermore, one should not exceed the allowed emission levels. Nowadays, to minimize the emissions of NO_x species, running the burner under lean premixed combustion conditions is desirable. However, this type of flame is prone to stabilization problems.

Lean blow-off (LBO) represents a key issue of gas turbine flames. Based on the theory developed by Kedia et al. [148], this phenomenon mainly occurs when the fresh reactant flow speed becomes higher than the flame-burning velocity. Under such conditions, the mixture can not be ignited, and the flame quenches. Understanding this phenomenon is extremely important since the desire is to operate the burner as lean as possible. Furthermore, the occurrence of LBO leads to a huge increase in carbon monoxide (CO) and unburned hydrocarbon emissions since the fuel does not complete the oxidation process [149]. Any variable able to affect the flame or the flow can consequently affect the LBO limit (equivalence ratio). Essential parameters affecting the equivalence ratio are the fuel composition [150], the dilution with inert species [151, 152], and the bulk axial velocity [51]. The first two aspects will be discussed later in this thesis (**Papers II-III, and V**, respectively).

In a gas turbine engine, a higher gas temperature at the inlet of the turbine is strongly desired to increase the engine efficiency. However, as mentioned earlier, this would increase the NO_x production and emission. A possible solution is to dilute the fuel with inert gases capable of decreasing the overall flame temperature. However, this can have the drawback of affecting the burner operability range and the flame characteristics (see **Paper V**). A feasible solution to extend the operability range and mitigate the flame stabilization issues is to use a pilot flame at the bottom of the main flame to sustain it. There exist several possible pilot flame configurations in the literature. This thesis investigates a ring with a multi-injection pilot configuration arranged around the main flame. The details of the burner are provided in the next section. The pilot flame aims

to provide a consistent amount of radical species and heat at the main flame root to promote the flame anchoring [104, 153].

Another flame instability that can affect the burner's regular operation is the flashback (FBC). This phenomenon occurs when the flame propagates upstream of the combustor liner toward the fresh reactant mixture. There exist several explanations for flashbacks. However, none of them can be considered "universal". Four are the most important mechanisms driving the flashback: (i) turbulent flame speed higher than the flow speed, (ii) flashback induced by the vortex breakdown [154], (iii) flashback due to combustion instabilities inducing velocity fluctuations [60] and (iv) flashback in the boundary layer caused by the velocity gradient at the wall [155]. The understanding of the flashback process is of crucial need since its occurrence can physically damage the combustor.

Emissions in Gas Turbine Burners

The exhaust gases from a gas turbine burner are of strong interest due to the increasing demand for low-emission levels. The main exhaust products are carbon dioxide (CO_2), water (H_2O), carbon monoxide (CO), unburned hydrocarbons (UHC), and nitrogen oxide (NO_x). Among these, CO_2 represents the main concern due to its impact on the surge of the greenhouse effect. However, this represents an inevitable combustion product, and it can be reduced only by consuming a lower amount of fuel or by replacing the fuel with a carbon-free variant. CO and NO_x represent emissions of primary concerns due to their toxic nature for humans and the environment. CO is mainly formed due to incomplete combustion [156]. This can occur due to either poor mixing between air and fuel or the presence of inert species in the fuel mixture. Furthermore, their formation can be related to the low flame speed under lean combustion conditions or too short residence times. NO_x expresses the sum of nitrogen dioxide (NO_2) and nitric oxide (NO). Several mechanisms are found to produce NO_x [157]:

- NO: it is produced in the regions of high flame temperature (above 1800K) following the Zeldovich mechanism [158] and through the reaction between NH and O_2 at low-temperature [159].
- N_2O: The N_2O-intermediate is relevant to the overall NO_x emissions under lean conditions and at low temperature.

The most effective method to minimize the overall NO_x emission level is to

keep the maximum temperature in the combustion zone low, thus running the burner under lean or rich conditions. On the other hand, to keep the overall CO production low, the flame temperature should be sufficiently high. At lean conditions, the temperature does not allow the complete oxidation of the fuel, while at rich conditions, fuel does not receive enough oxygen to complete the combustion process. Therefore, the optimal emission level of NO_x and CO is achieved in a very small range of temperatures, as visible in Figure 4.2.

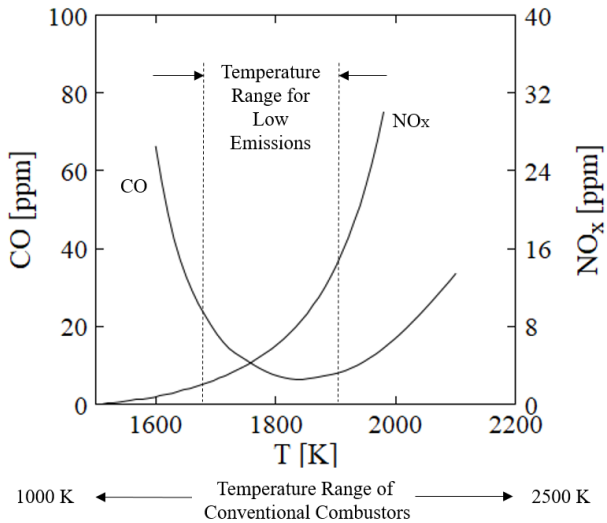

Figure 4.2: Diagram showing the CO and NO_x trends with temperature. Minimum CO and NOx emission levels are achieved in a small range of temperatures.

The CeCOST Burner

The burner investigated in this thesis was initially designed by Hodzic [160, 161] and later optimized [129] and developed (**Paper II-V**) to faithfully reproduce the characteristic features of typical gas turbine swirler combustors. A schematic of the latest version of the lab-scale CeCOST burner is shown in Figure 4.3, along with some extra details presented in Fig. 4.4. The burner is mounted vertically in the atmospheric pressure rig at Lund University.

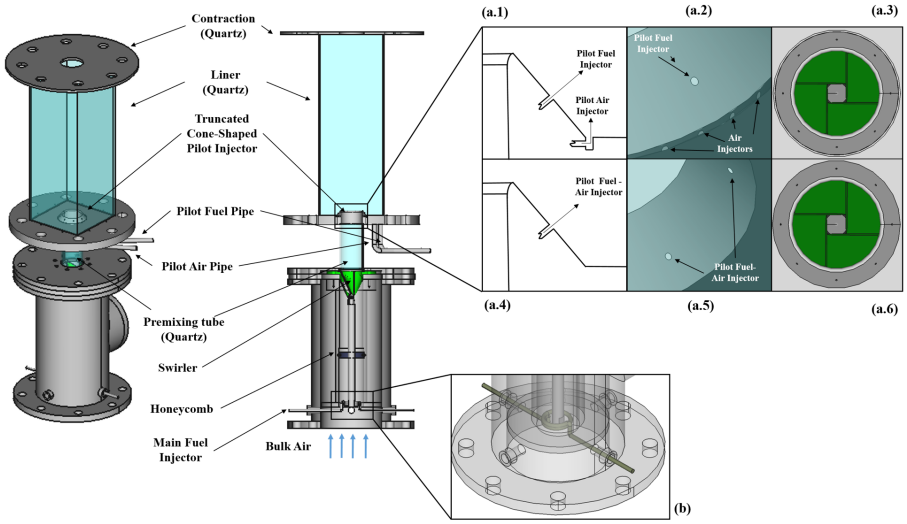

Figure 4.3: Isometric and cross-sectional view of the lab-scale CeCOST burner assembly; (a.1) details of the section of non-premixed pilot injectors, (a.2) isometric view of non-premixed pilot injectors, (a.3) top view of non-premixed pilot injectors, (a.4) premixed/partially premixed pilot injectors, (a.5) isometric view of the premixed/partially premixed pilot injectors, (a.6) top view of premixed/partially premixed pilot injector, isometric view of the main fuel injectors (b).

Dry air is supplied by a blower whose rotational frequency can be adjusted to control the mass flow rate. The air enters a plenum connected to the blower, directing the flow to the vertical direction [162]. Downstream of the plenum, fuel is injected through a spiral injection system [129], see Figure 4.3.b. Air and fuel start to mix, passing inside a mixing pipe (220 mm long and 54 mm in diameter) and a honeycomb plate that breaks up potential large flow structures. Then, a swirling motion is provided by a counter-clockwise swirl generator made by four quarter-cones; the half-angle of the cones is around 25 degrees, and the blades are approximately 2 mm thick. Mixing is further enhanced by a premixing tube (100 mm in length and 50 mm in inner diameter) located above the swirler. At the exit of the mixing pipe, a combustion chamber (cross-section side length of 140 mm) is mounted above a metallic dump plate. The combustion chamber is manufactured in quartz to ensure full optical access for diagnostics. A truncated cone-shaped pilot injector is placed above the dump plate, around the main flame nozzle; see Figure 4.3.a 1-6. In this thesis, three different pilot injectors are investigated: non-premixed, partially premixed (**Paper II**), and fully premixed (**Paper III**) injectors. The non-premixed pilot injector consists of 8 holes (1 mm in diameter) for pilot fuel injection located around the outer truncated cone surface, surrounded by 36 holes (1 mm in diameter) for pilot air injection, placed at the bottom of the truncated cone-shape (Figure 4.3.a 1-3). The premixed and the partially-premixed pilot flame arrangements are equipped

with eight holes (1 mm in diameter) through which the mixture of fuel and air is injected, see Figure 4.3.a 4-6. Finally, a quartz contraction section is placed at the top of the combustor liner.

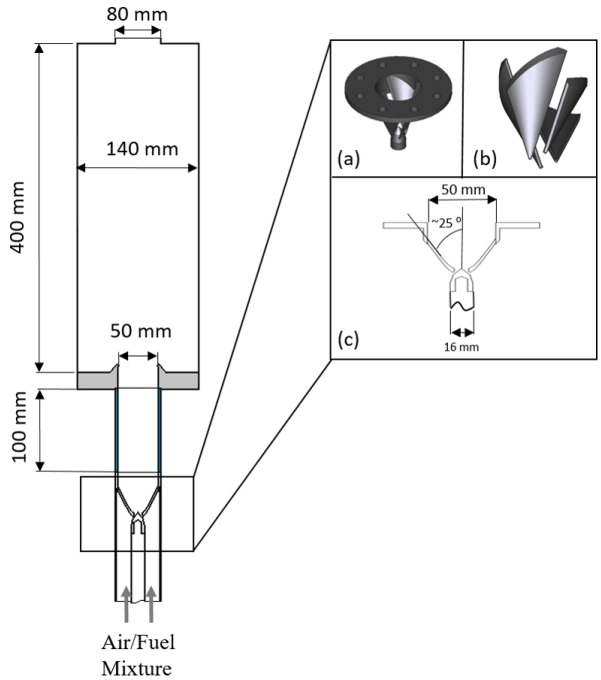

Figure 4.4: A schematic drawing of the CeCOST burner. The swirler is mounted on a lance of 16 mm diameter. The upstream mixing tube has a length of 220 mm and an inner diameter of 54 mm. (a) and (b) show isometric views of the swirler and the swirling blades, respectively. (c) shows the cross-section of the swirler

Chapter 5

Summary of Results

The results obtained in this thesis project are described in detail in **Papers I-V**, attached to this thesis. Highlights of the results from the papers are presented in this chapter. First, the DNS results of the displacement speed analysis of statistically planar turbulent premixed flames (**Paper I**) are presented. Then, the impacts of pilot flames and hydrogen enrichment on the swirling premixed methane/air flames in a gas turbine model combustor (GTMC) with a swirl-burner (known as the CECOST burner) (**Papers II** and **Papers III**) and on the burner surface temperature in the GTMC (Paper **IV**) are presented. Last, the CO_2 dilution effects on syngas flames in the GTMC (**Paper V**) are highlighted.

DNS of Planar Turbulent Premixed Flames

DNS of four premixed flame cases is carried out to investigate the impact of density ratio (closely related to the amount of heat released across the flame) on the structure and propagation of turbulent premixed flames. As shown in Table 5.2, Case A assumes a constant density across the flame (which is referred to as reacting wave in **Papers I**), i.e., with a density ratio between the unburned gas to the burned gas (Θ) of 1 (i.e., without heat release across the flame), and Cases B–D have Θ of 2, 5 and 7, respectively. All the investigated cases are designed to share the same major characteristics (see Table 5.2). Here, $Da = \tau_t/\tau_F$ and $Ka = \tau_F/\tau_\eta$ refer to the Damköhler and the Karlovitz numbers, respectively, with τ_t being the integral flow scale, τ_F the chemical scale and τ_η the Kolmogorov time scale. $Pe = u_0 L_{11}/\mathcal{D}$ refers to the turbulent Péclet number as the ratio

between the rate of advective and diffusion transport. L_{11} is the integral of the longitudinal auto-correlation function. The ratio of $\delta_F/\Delta x$ characterizes the grid resolution in terms of the number of grid points per laminar flame thickness. To inhibit the development of Darrieus-Landau (DL) instability [163, 164], the domain size, $\Lambda \approx 11\delta_F$, is kept below the cutoff wavelength, $\lambda_c \approx 20\delta_F$ (at $\Theta = 7$), above which the DL instability arises. Table 5.2 shows a summary of major parameters.

Table 5.1: Key parameters of the four DNS cases.

Case	$\frac{\rho_u}{\rho_b}(=\Theta)$	$\frac{\Lambda_x}{\Lambda}$	N_x	$\frac{u_0}{S_L}$	$\frac{L_{11}}{\delta_F}$	$\frac{\delta_F}{\Delta x}$	Da	Ka	Pe
A	1	4	1024	6	1.2	24	0.2	39	6.95
B	2	4	1024	6	1.2	24	0.2	39	6.95
C	5	4	1024	6	1.2	24	0.2	39	6.95
D	7	4	1024	6	1.2	24	0.2	39	6.95

The analysis of the numerical results relies on fully-developed statistics, which is performed following a "global" and a "local" statistical sense. In the first approach, the analysis involves statistical quantities extracted at different locations as indicated by the reaction progress variable $c(\mathbf{x}, t) = \hat{c} \in (0, 1)$ across the flame, while in the second, the assessment of the correlation between relevant quantities focuses on two specific values of $\hat{c}$, representing the preheat and the post-flame zone of the flame.

The equations described in Chapter 2 are applied to characterize flame propagation in a turbulent environment. The mathematical description of the statistical tools used in this section is provided in Appendix A of this thesis. Bearing in mind that $\langle \partial_t^* \phi \rangle_s = \langle \mathbb{A}(\phi) \rangle_s + \langle \mathbb{B}(\phi) \rangle_s$, Fig. 5.1 shows a combination of terms for each of the four cases A–D, across the entire flame brush ("global" sense). The surface-averaged values of acceleration/deceleration, $\langle \partial_t^* \check{s}_d \rangle_s |_{\hat{c}}$, attain positive values across the flame. At the same $\hat{c}$, the value of $\langle \partial_t^* \check{s}_d \rangle_s |_{\hat{c}}$ drops as the density ratio increases, especially at $\hat{c} > 0.5$. Furthermore, this acceleration/deceleration term is close to its surface-averaged curvature contribution part, $\langle \partial_t^* \nabla \cdot \boldsymbol{n} \rangle_s |_{\hat{c}}$, in the preheat zone ($\hat{c} < 0.3$). However, the differences between these two terms increase across the flame. Nevertheless, this difference decreases as the density ratio across the flame, Θ, increases. Bearing in mind the relation $\langle \mathbb{A}(\phi) \rangle_s = \langle \partial_t^* \phi \rangle_s - \langle \mathbb{B}(\phi) \rangle_s$ and $\langle \mathbb{B}(S_d^W) \rangle_s = 0$, Fig. 5.1(b) shows the $\mathbb{B}$ terms for the displacement speed, $\check{s}_d$, and the curvature, $\nabla \cdot \boldsymbol{n}$. It is evident that the trend for $\langle \partial_t^* \nabla \cdot \boldsymbol{n} \rangle_s |_{\hat{c}}$ observed in Fig. 5.1(a) mainly comes from $\langle \mathbb{B}(\nabla \cdot \boldsymbol{n}) \rangle_s$. On the other hand, $\langle \mathbb{B}(\check{s}_d) \rangle_s$ shows a huge difference as compared to $\langle \partial_t^* \check{s}_d \rangle_s |_{\hat{c}}$. The reaction contribution to $\check{s}_d$, $\check{s}_d^W$, is studied through $1/|\nabla c|$ (see definition in Eq. 2.15 in Section 2 and the assumption that $\mathbb{W}$ solely depends on c) in Fig. 5.1(c).

The latter shows that $\langle \partial_t^*(1/|\nabla c|)\rangle_s|_{\hat{c}}$ is positive for all possible $\hat{c}$, meaning that the flame experiences a net thickening. Furthermore, the surface-averaged rate of change in thickness decreases with higher density ratio due to the stronger turbulence inhibition for higher density ratios, Θ. Flow dilatation, $\nabla\cdot\boldsymbol{u}$, directly contributes to $\partial_t^*\phi$ through the product term $(\phi\nabla\cdot\boldsymbol{u})$ inside $\mathbb{A}(\phi)$, in Eq. 2.18. The surface-average of this quantity, $\langle\phi\nabla\cdot\boldsymbol{u}\rangle_s$, is shown in Figures 5.1(d) and (c), for $\phi \in (\check{s}_d, \nabla\cdot\boldsymbol{n}, 1/|\nabla c|)$. Interestingly, all the terms remain positive across the flame brush and attain higher values as the density ratio increases, for the density-varying flame cases. Profiles of $\langle\nabla\cdot\boldsymbol{u}/|\nabla c|\rangle_s|_{\hat{c}}$ appear flat for all $\hat{c} \in (0,1)$, while the two terms $\langle\nabla\cdot\boldsymbol{n}\nabla\cdot\boldsymbol{u}\rangle_s|_{\hat{c}}$ and $\langle\check{s}_d\nabla\cdot\boldsymbol{u}\rangle_s|_{\hat{c}}$ grow to a peak in the middle $\hat{c}$.

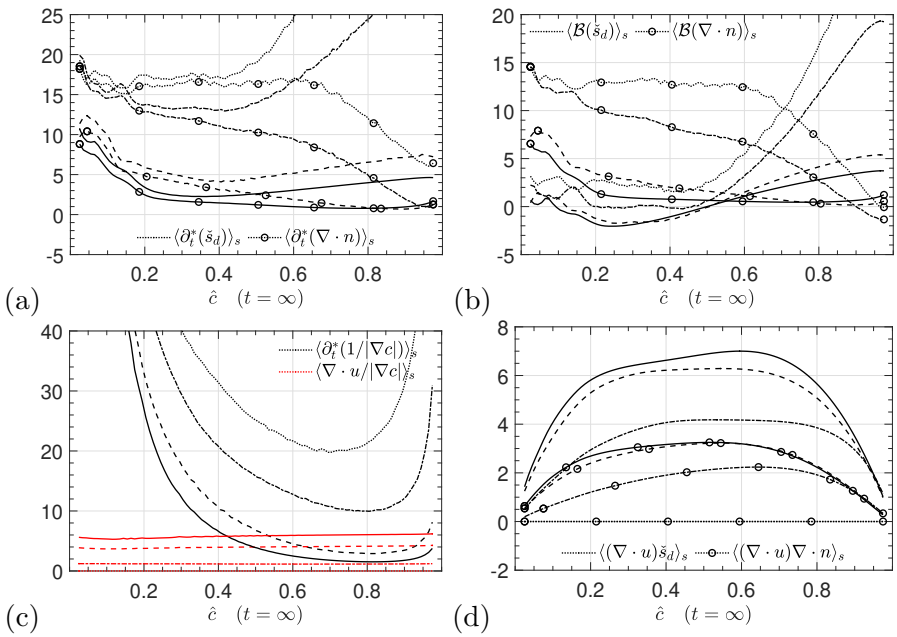

Figure 5.1: Surface-averaged terms of (a) $\langle\partial_t^*\check{s}_d\rangle_s|_{\hat{c}}$ and $\langle\partial_t^*(\nabla\cdot\boldsymbol{n})\rangle_s|_{\hat{c}}$, (b) $\langle\mathbb{B}(\check{s}_d)\rangle_s|_{\hat{c}}$ and $\langle\mathbb{B}(\nabla\cdot\boldsymbol{n})\rangle_s|_{\hat{c}}$, (c) $\langle\partial_t^*(1/|\nabla c|)\rangle_s|_{\hat{c}}$ and $\langle\nabla\cdot\boldsymbol{u}/|\nabla c|\rangle_s|_{\hat{c}}$, and (d) $\langle(\nabla\cdot\boldsymbol{u})\check{s}_d\rangle_s|_{\hat{c}}$ and $\langle(\nabla\cdot\boldsymbol{u})\nabla\cdot\boldsymbol{n}\rangle_s|_{\hat{c}}$ plotted against $\hat{c} \in (0,1)$ for fully developed flame. In all sub-figures, four lines styles of dot, dash-dot, dash and solid represent cases A, B, C and D respectively.

The "local" statistical analysis is performed using area-weighted two-quantities joint probability density functions (jpdf) and conditioned surface-averages, selecting relevant combination of physical quantities across two isosurfaces of $\hat{c}$ = 0.3 and 0.87 representing the preheat zone and reaction zone, respectively, for two DNS cases B and D (having Θ = 2 and 7, respectively). The definitions of jpdf and conditioned surface-average are given in the Appendix A of the thesis. Figure 5.2 shows the $\check{s}_d$-conditioned surface-averages, $[\partial_t^*\phi]_s|_{\check{s}_d,c}$ for

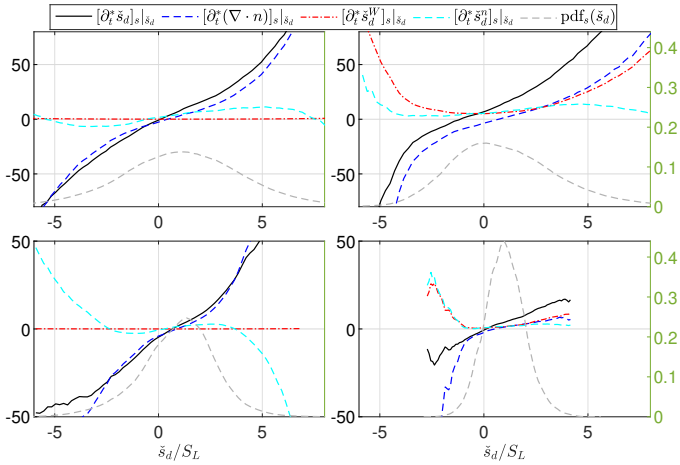

Figure 5.2: Fully developed $[\partial_t^* \phi]_s|_{\check{s}_d,\hat{c}}$ for four quantities $\phi \in (\check{s}_d, \nabla\cdot\boldsymbol{n}, \check{s}_d^W, \check{s}_d^n)$ (labeled on left axis) and $\mathrm{pdf}_s(\check{s}_d)|_{\hat{c}}$ (labeled on right axis). Results refer to $\Theta = 2$ (case B, top) and 7 (case D, bottom) at $\hat{c}$=0.3(left) and 0.87 (right). All dimensioned quantities are normalized based on speed unit S_L and length unit δ_F.

the displacement speed and its three components, $\phi \in (\check{s}_d, \nabla\cdot\boldsymbol{n}, \check{s}_d^W, \check{s}_d^n)$ for cases B (top) and D (bottom) for $\hat{c} = 0.3$ (left) and 0.87 (right). These have been computed based on $\mathrm{jpdf}_s(\phi, \check{s}_d)$. Here, this quantity is show in Fig. 5.3 for density-weighted displacement speed, $\check{s}_d$, only. However, the corresponding $\mathrm{jpdf}_s(\phi, \check{s}_d)$ for the three components of $\check{s}_d$ are available in the Supplementary Material of **Paper I**. It is clear from Figure 5.2 as well as 5.3 that $[\partial_t^* \check{s}_d]_s|_{\check{s}_d,c}$ monotonically increases from negative to positive values in a range of negative to positive values of $\check{s}_d$. This indicates that surface elements having a more negative $\check{s}_d$ tend to retreat faster. Similarly, elements having a more positive $\check{s}_d$ tend to move faster. These results are in line with the observations reported in Ref. [101] for constant density flames. However, this acceleration effect is lower at higher density ratio, when moving toward the reaction zone.

Looking at the three contributions to $[\partial_t^* \phi]_s|_{\check{s}_d,c}$ to the conditional average of displacement speed in Figure 5.2, it is visible that the effect of curvature, $[\partial_t^*(\nabla\cdot\boldsymbol{n})]_s|_{\check{s}_d}$, is dominant in the preheat zone with the exception of large $|\check{s}_d|$, where the contribution from the normal diffusion becomes relevant, $[\partial_t^* \check{s}_d^n]_s|_{\check{s}_d}$. Furthermore, its effect significantly increases in the reaction zone (left side of the figures), along with the effect of the reaction term, $[\partial_t^* \check{s}_d^W]_s|_{\check{s}_d}$. However, $[\partial_t^* \check{s}_d^n]_s|_{\check{s}_d}$ affects only a range of $\check{s}_d$ with low probability density and while it is always positive for $\hat{c} = 0.87$, it becomes positive at far end negative values of $\check{s}_d$, for $\hat{c} = 0.3$. This trend suggests that in the preheat zone, the curvature effect causing a negative acceleration on retreating surfaces is counteract by the normal-diffusion effect.

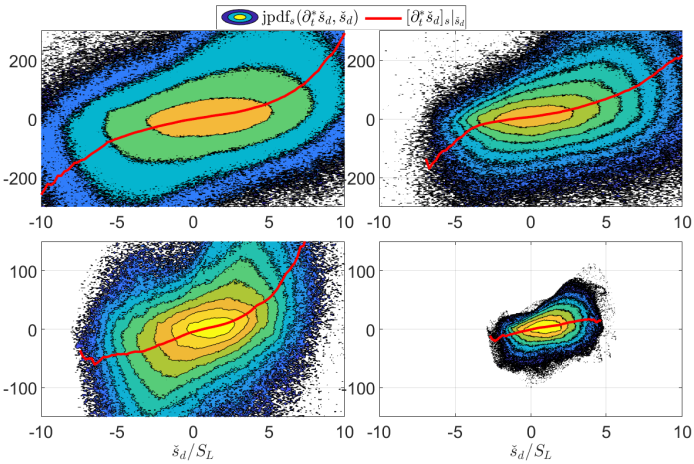

Figure 5.3: Fully developed jpdf$_s(\partial_t^* \check{s}_d, \check{s}_d)|_{\hat{c}}$ and $[\partial_t^* \check{s}_d]_s|_{\check{s}_d,\hat{c}}$ (in red). Results refer to $\Theta = 2$ (case B, top) and 7 (case D, bottom) at $\hat{c}$=0.3(left) and 0.87 (right). All dimensioned quantities are normalized based on speed unit S_L and length unit δ_F.

The local curvature in Figure 5.2 has shown a strong correlation with the displacement speed. Fig. 5.4 shows that $[\partial_t^*(\nabla\cdot\boldsymbol{n})]_s|_{\nabla\boldsymbol{n},\hat{c}}$ attains high positive values toward positive curvature with significant magnitude. Furthermore, $[\partial_t^*(\nabla\cdot\boldsymbol{n})]_s|_{\nabla\boldsymbol{n},\hat{c}}$ is negative for high negative values of $\nabla\cdot\boldsymbol{n}$. The corresponding contributions on the rate of change on curvature, $\mathbb{A}(\nabla\cdot\boldsymbol{n})$ and $\mathbb{B}(\nabla\cdot\boldsymbol{n})$, have almost the same impact on $[\partial_t^*(\nabla\cdot\boldsymbol{n})]_s|_{\nabla\boldsymbol{n},\hat{c}}$. By looking at the pdf$_s(\nabla\cdot\boldsymbol{n})$ related to the reaction zone ($\hat{c}$=0.87), it is visible how their peak shifts more toward negative values of $\nabla\cdot\boldsymbol{n}$ than ones in the preheat zone ($\hat{c}$=0.3). The dilatation-product term $[\nabla\cdot\boldsymbol{u}\nabla\cdot\boldsymbol{n}]_s$ is always positive for all the possible $\nabla\cdot\boldsymbol{n}$ values, and its effect is to resist to the curvature acceleration toward the negative side.

Large values of $|\nabla\cdot\boldsymbol{n}|$ are related to a highly curved isosurface element subjected to a high tangential diffusion that smear out the spatial gradient of c, thus highly curved flame elements for which $1/|\nabla c| >> 1/|\nabla c|_L$. A similar behaviour is also visible when considering the phenomenon of flame thickening acceleration. In fact, from Figure 5.5, one can notice that large values of $[\partial_t^*(1/|\nabla c|)]_s|_{1/|\nabla c|,\hat{c}}$ are related to large $1/|\nabla c|$ values. Furthermore, values for $[\partial_t^*(1/|\nabla c|)]_s|_{1/|\nabla c|,\hat{c}}$ tend to be lower in the reaction zone and for higher values of Θ. Thus, the turbulence inhibits the flame surface to be more thickened. This may be also confirmed by looking at the dilatation-product term, $[\nabla\cdot\boldsymbol{u}/|\nabla c|]_s|_{1/|\nabla c|}$, that is almost constant with $1/|\nabla c|$. Moreover, Figure 5.5 shows that $[\mathcal{K}]_s|_{1/|\nabla c|,\hat{c}}$ stays positive on $|\nabla c_L|/|\nabla c| < 1$ and negative on $|\nabla c_L|/|\nabla c| > 1$. This indicates that the creation of new surface elements (associated to $\mathcal{K} > 0$) favors locally thinned flame zones ($|\nabla c_L|/|\nabla c| < 1$). Similarly, the destruction of surface elements (happening for

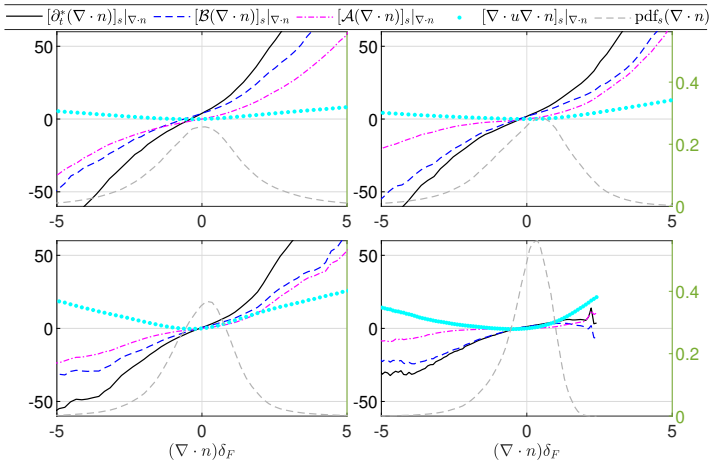

Figure 5.4: Fully developed $[\phi]_s|_{\nabla\boldsymbol{n},\hat{c}}$ for four quantities $\phi \in [\partial_t^*(\nabla\cdot\boldsymbol{n}), \mathbb{B}(\nabla\cdot\boldsymbol{n}), \mathbb{A}(\nabla\cdot\boldsymbol{n}), \nabla\cdot\mathbf{u}\nabla\cdot\boldsymbol{n}]$ and $\mathrm{pdf}_s(\nabla\cdot\boldsymbol{n})|_{\hat{c}}$ (labeled on right axis). Results refer to $\Theta = 2$ (case B, top) and 7 (case D, bottom) at $\hat{c}$=0.3(left) and 0.87 (right). All dimensioned quantities are normalized based on speed unit S_L and length δ_F.

$\mathcal{K} < 0$) occurs at thickened flame zones.

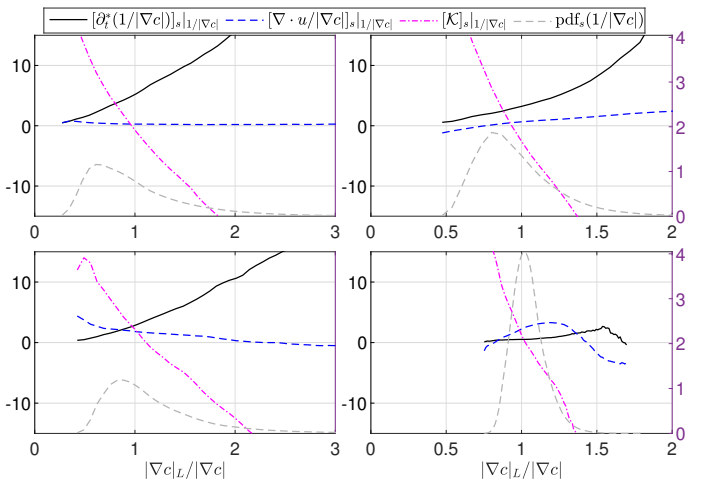

Figure 5.5: Fully developed $[\phi]_s|_{1/|\nabla c|,\hat{c}}$ for three quantities $\phi \in [\partial_t^*(1/|\nabla c|), \nabla\cdot\mathbf{u}/|\nabla c|, \mathcal{K}]$ (left axis) and $\mathrm{pdf}_s(1/|\nabla c|)|_{\hat{c}}$(right axis). Results refer to $\Theta = 2$ (case B, top) and 7 (case D, bottom) at $\hat{c}$=0.3(left) and 0.87 (right). All dimensioned quantities are normalized based on speed unit S_L and space unit δ_F.

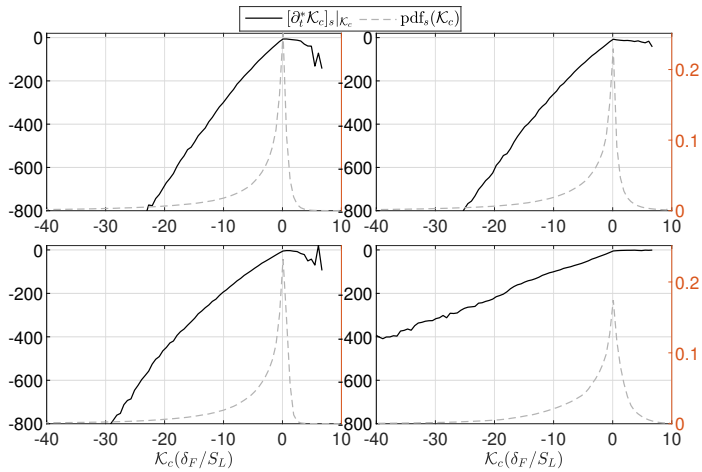

Figure 5.6: Fully developed $[\partial_t^* \mathcal{K}_c]_s|_{\mathcal{K}_c,\hat{c}}$ (left axis) and $\mathrm{pdf}_s(\mathcal{K}_c)|_{\hat{c}}$ (right axis). RFesults refer to $\Theta = 2$ (case B, top) and 7 (case D, bottom) at $\hat{c}$=0.3 (left) and 0.87 (right). All dimensioned quantities are normalized based on speed unit S_L and length δ_F.

The correlation between $\check{s}_d$ and $\nabla \cdot \boldsymbol{n}$, together with the aforementioned acceleration behaviors toward large $|\check{s}_d|$ and large $|\nabla \cdot \boldsymbol{n}|$, results in a clear acceleration toward negative values of curvature-induced stretch rate, $\mathcal{K}_c$ (see Equation 2.29 in Section 2). Figure 5.6 shows a positive slope of $[\partial_t^* \mathcal{K}_c]_s|_{\mathcal{K}_c,\hat{c}}$ in the negative branch of $\mathcal{K}_c$. Large negative values of $\mathcal{K}_c$ are related to the destruction event of surface elements. Therefore, based on the above observation, elements tend to accelerate while vanishing. This acceleration does not exist for positive values of $\mathcal{K}_c$, and it refers to elements whose $\check{s}_d$ has a different sign from $\nabla \cdot \boldsymbol{n}$. These elements can be considered to "live" briefly after being formed. Although the thermal expansion reduces the slope in the negative branch, the acceleration event to the destruction is still visible.

Hydrogen-Enriched Methane/Air Flames in a Gas Turbine Model Combustor

Operability Limits and Flame Structure

The potential of pilot flame usage to achieve better flame stabilization at lean operating conditions is studied in the GTMC with the CeCOST swirl burner for two levels of hydrogen enrichment of the methane/air mixture (0% and 50% in volume fraction). A non-premixed and a partially premixed pilot flame are

investigated. The stability regime is determined experimentally by varying three parameters: the global equivalence ratio (Φ_g), the ratio of the pilot to the global mass flow rates ($\dot{m}_p/\dot{m}_g$) and the Reynolds number (Re). The experiments are performed varying one parameter while keeping the other two constant. Two different values of Re (10000 and 20000) are investigated. The pilot fuel and air are routed from the main to maintain the same global equivalence ratio of Φ_g. Two different pilot flow rates, $\dot{m}_p/\dot{m}_g = 2\%$ and 4% are selected. A summary of the selected cases is shown in Table 5.2.

Table 5.2: Properties of the investigated cases.

Case	Pilot Flame Type	Re	$\dot{m}_p/\dot{m}_g$
$R_{10}P_0$	No Pilot	10000	0%
$R_{20}P_0$	No Pilot	20000	0%
$R_{10}P_{N,2}$	Non-premixed Pilot	10000	2%
$R_{20}P_{N,2}$	Non-premixed Pilot	20000	2%
$R_{10}P_{N,4}$	Non-premixed Pilot	10000	4%
$R_{20}P_{N,4}$	Non-premixed Pilot	20000	4%
$R_{10}P_{P,2}$	Partially Premixed Pilot	10000	2%
$R_{20}P_{P,2}$	Partially Premixed Pilot	20000	2%
$R_{10}P_{P,4}$	Partially Premixed Pilot	10000	4%
$R_{20}P_{P,4}$	Partially Premixed Pilot	20000	4%

The burner operability map is shown in Figure 5.7. The LBO and FBC equivalence ratio detection is repeated three times to ensure repeatability. Two different flashback conditions are distinguished: in the first, the main flame enters the premixing tube (FPMT), while in the second the flame is attached to the swirler (FAS).

Pilot flames improve the flame stability, extending the LBO global equivalence ratio to leaner conditions. Here, two different effects of the pilot flame are expected. Firstly, the pilot flame provides hot gas and radicals that are recirculated in the inner and in the outer recirculation zone (IRZ and ORZ, respectively) toward the flame root, helping the re-ignition process at extremely lean conditions. Secondly, the pilot flame increases the local equivalence ratio leading to a higher local flame temperature compared with the flame without pilot involved. With the respect of flashback limits, the pilot does not lead to any improvement, due to the burner setup used in this investigation. In fact, once the main flame is in the premixing tube, there is no chance for the pilot to interact with it (see Figures 4.3 and 4.4 in Section 4).

Increasing Re results in a wider stability range, consistently with the findings from a previous investigation carried out on the previous generation of the present burner [57]. Regarding the LBO improvement, a possible explanation

is that an increase on Re leads to an increased level of flame wrinkling due to the higher turbulence intensity, thus a higher flame surface density and a higher turbulent flame speed. Consequently, the resulting flame is more stable and less affected by perturbations that can facilitate LBO. The flashback limit is quite sensitive to Re. A larger Reynolds number increases the turbulence levels, thus the turbulent flame speed as well as the flow rate. Therefore, an increase in Re leads to two opposite effects: enhancing of propensity of flashback due to a higher turbulent flame speed and a larger flow rate reducing the tendency to flashback. At Re = 20000, the pure methane/air flame propagates in the premixing tube without attaching to the top of the swirler (FPMT case).

The effect of hydrogen-enrichment is visible comparing the LBO and FBC limits. Consistently with previous experimental results [57, 165], the critical Φ_g for lean blow-off shifts to leaner mixtures due to a faster reaction rate, higher diffusivity, and higher burning velocity. On the other hand, a higher turbulent flame speed makes the flame more prone to flashback. Therefore, the stability range for hydrogen-enriched methane/air flame is smaller as compared with pure methane/air flame case.

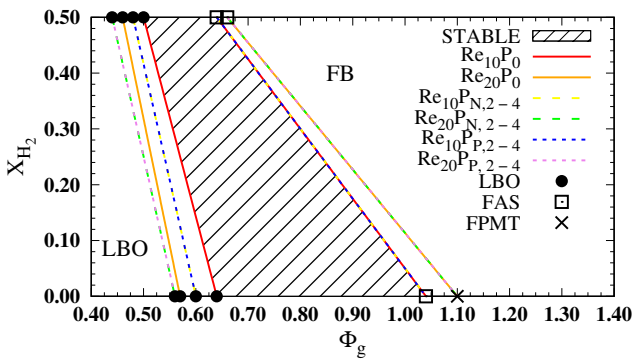

Figure 5.7: CeCOST burner operability map for no pilot (subscript 0), diffusion pilot (subscript N) and partially premixed pilot (subscript P) cases at $\dot{m}_p/\dot{m}_g = 2\%$ and 4% condition (subscript 2-4) at turbulence levels of Re=10000 and 20000, for H_2/CH_4: 0/100 and 50/50 in vol % fuel mixtures. Lean blow-off (LBO) and flashback (FB) regions are indicated.

Figure 5.8 shows the time-averaged OH* chemiluminescence for H_2-enriched methane flame at $\Phi = 0.52$ for $Re_{10}P_{N,2}$ (left) and $Re_{10}P_{P,2}$(right). The stability of pilot flames is analyzed based on the probability of pilot flames to be attached to the burner nozzle under different operating conditions. Statistics are computed extracting the signal intensity in the white frame shown in Figure 5.8 from each single-shot chemiluminescence image, integrated along the radial direction (r), and binarized at each time assigning a value of 1 when the intens-

ity is higher than the 10% of the maximum value, otherwise assigning a value of 0. The probability is then calculated based on the mean value of the binarized intensity in the first two pixels in the vicinity of the pilot flame orifice. The results are shown in Figure 5.9.

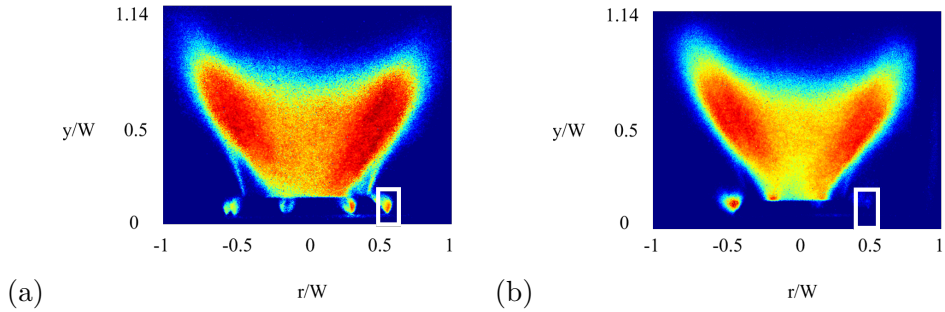

Figure 5.8: Time-averaged OH* chemiluminescence showing the H_2-enriched methane flame in case of pilot flame attached to the injector (a, $Re_{10}P_{N,2}$) and lifted pilot flame (b, $Re_{10}P_{P,2}$). One of the pilot flames in the vicinity of the pilot burner orifice is indicated using the white boxes.

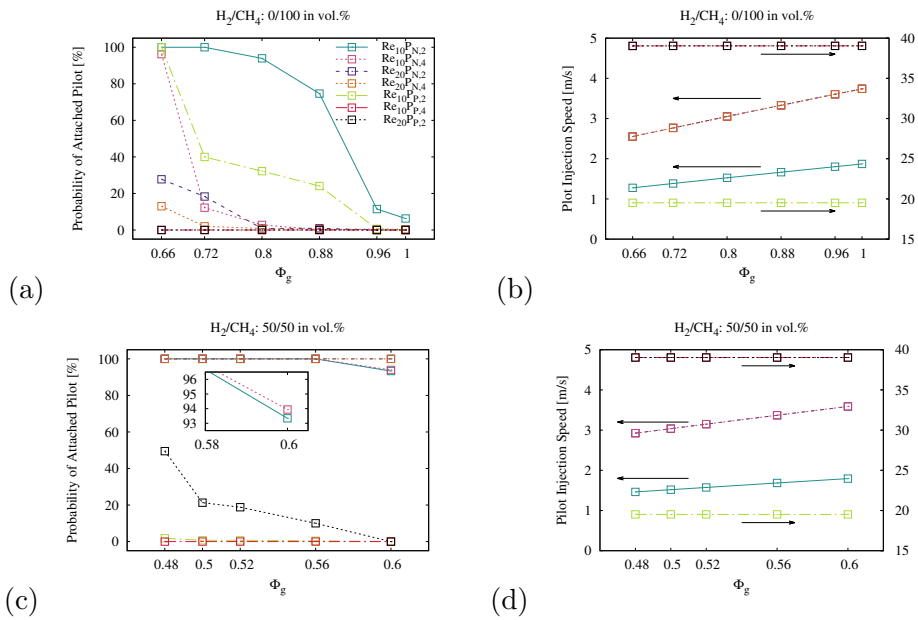

Figure 5.9: Probability of attached pilot flames in [%] (left column) and pilot injection speed in [m/s] (right column) for H_2/CH_4: 0/100 (top) and 50/50 (bottom) in vol.%. For the P_N cases only the fuel mass flow rate contributes to the jet velocity while for the P_P cases the mass flow rate of the partially premixed fuel/air mixture contributes to the jet velocity.

Considering the non-premixed pilot flame case at Re=10000 ($Re_{10}P_{N,2}$) for

methane flame (see Figure 5.9.a), it is visible that there exists a high probability of having a pilot flame attached to the orifice at low Φ_g. However, this probability decreases for richer conditions due to a higher amount of injected pilot fuel, thus a higher injection velocity (see Figure 5.9.b). This also explains why at higher Reynolds number ($Re_{20}P_{N,2}$) a higher tendency of pilot lift off is visible. A similar result is shown for an increased pilot air and fuel flow rate, at constant Re ($Re_{10}P_{N,4}$). Furthermore, a lower probability of seeing a pilot flame attached to the orifice is shown when the partially premixed pilot flame is used (e.g., case $Re_{10}P_{P,2}$) as compared with the non-premixed pilot case, under the condition of the same Re and Φ_g.

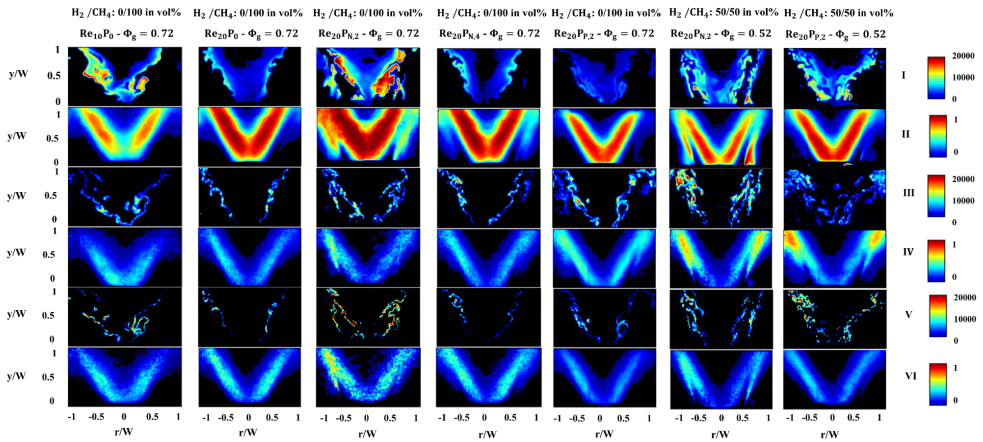

Figure 5.10: OH- and CH_2O-PLIF results for methane/air and hydrogen-enriched methane/air flames at stable flame conditions. From top row to bottom row: **I** single-shot of OH-PLIF; **II** PM of OH PLIF intensity; **III** single-shot of CH_2O-PLIF intensity; **IV** PM of CH_2O PLIF intensity; **V** heat release zone (OH $\times$ CH_2O); **VI** PM of heat release zone.

Flame structure investigation is performed through the processing of simultaneous OH- and CH_2O-PLIF images. Rows I, III and V in Fig. 5.10 show single-shot images of OH-PLIF, CH_2O-PLIF and the heat release zones, respectively, while their corresponding probability maps (PMs) obtained from the binarized single-shot images are shown in rows II, IV and VI. The PLIF single-shots show that the CH_2O (preheat zone marker) and thus the OH x CH_2O (heat release zone marker) signals are in a thin layer, meaning that the flames are in the flamelet regime [27]. The preheat zone in the H_2-enriched cases appears relatively thicker mainly owing to the M-shaped flame structure. Under such flame shape conditions, the two preheat zones can merge, increasing the overall thickness. The PMs (as indicator of the mean flame structure) show an M-shape both with or without pilot flames. Furthermore, for hydrogen-enriched flames,

the thickened preheat zone is more localized, which can be be due to the differential diffusion effect for these lean premixed flames. The flame leading front is placed along the burner axis, indicating that the flame is stabilized in the inner recirculation zone (IRZ) of the combustor. At higher Reynolds number, the flame front tip moves upstream as a result of the higher turbulent intensity, thus flame speed.

It is visible, comparing $Re_{20}P_0$ and $Re_{20}P_{N,2}$, that the non-premixed pilot flame slightly shifts the main flame average position downstream the combustion chamber. This can be assessed by the lower amount of main fuel and air mass flow rates injected when the pilot flame is used. Thus, the main flame stabilizes downstream the liner. Differences between the type of pilot flame used are visible comparing the $Re_{20}P_{N,2}$ with case $Re_{20}P_{P,2}$; the partially premixed pilot flame tends to be lifted off and the fresh fuel/air mixture does not properly ignite once injected in the liner. Thus, the fuel/air mixture mainly ignites in the IRZ by interacting with the main flame. Similar effect occurs when increasing the pilot air and fuel flow rate (see Case $Re_{20}P_{N,4}$). In both these cases, the overall flame shape experiences a shifting from attached to unattached M-shape.

As it is visible in Figure 5.7, the H_2-enrichment shifts the flame stability regime toward leaner mixture. Therefore, in this thesis, the comparison between the two different mixtures is done at similar main flame behaviour condition at $\Phi_g = 0.72$ for pure methane case and at $\Phi_g = 0.52$ for hydrogen-enriched/methane case. At this equivalence ratio, the H_2-enriched methane/air flame stabilises at approximately the same location as it does for $\Phi_g = 0.72$ for the methane flame. Furthermore, when non-premixed pilot flame is used (column 6 in Figure 5.10), the flame structure appears as an attached M-shape, since the non-premixed pilot flame has a higher probability to be attached to the pilot orifice, as shown in Figure 5.9.c.

NO_x and CO Emissions

Figure 5.11 shows the NO_x (left column) and CO (right column) levels in the exhaust gases for different pilot type, fuel mixture, Reynolds number, Φ_g as well as $\dot{m}_p/\dot{m}_g$. Numerical results from freely propagating adiabatic planar laminar premixed flames (1D) are added for comparison. The numerical simulations were carried out using the Cantera code [166] and the GRI-3.0 chemical kinetic mechanism [166]. All the reported vales are normalized to the 15% O_2 condition.

Trends show an increase of NO_x emission level with Φ_g as a consequence of the higher flame temperature for both methane/air and hydrogen-enriched meth-

ane/air flames. An increase of the attained values is also visible when moving from a Reynolds number of 10000 to 20000, due to a higher turbulent burning velocity, leading to lower heat losses through the wall, thus a higher flame temperature. The type of pilot flame has a low impact on NO_x emission. In fact, the methane/air flames without pilot ($Re_{20}P_0$) show a similar level of NO_x as the corresponding flame with partially premixed pilot ($Re_{20}P_{P,4}$). This is reasonably due to the fact that the pilot flames are lifted and the resulting flame structure is similar. It is expected that the non-premixed pilot flame would have a higher amount of NO_x produced due to the diffusion flame structure that gives rise to locally higher flame temperatures. However, since at high Φ_g the pilot flame tend to lift off, the mixing of pilot flame with the surrounding is improved and this lowers the temperature differences. Due to the shift in operability range toward leaner mixtures, the hydrogen-enriched methane/air flame has a lower amount of NO_x emitted.

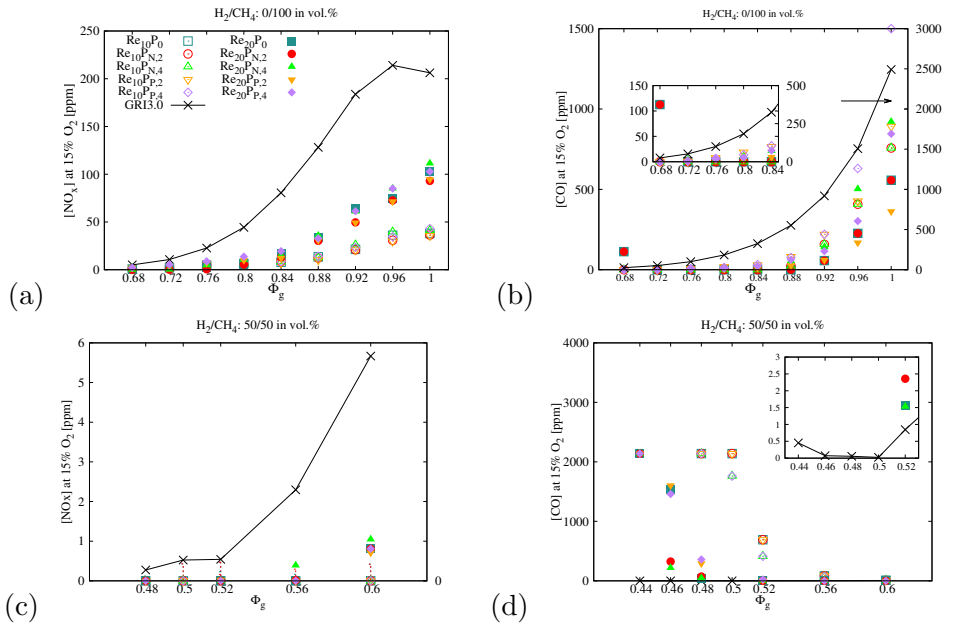

Figure 5.11: Emissions of NO_x (left column) and CO (right column) at 15% O_2 for methane/air flames (first row) and hydrogen-enriched methane/air flames (second row).

At $\Phi_g < 0.72$, the CO emissions in cases $Re_{20}P_0$ and $Re_{20}P_{N,2}$ show a minor increase with decreasing Φ_g, which can be related to the local flame extinction near LBO. However, for $\Phi_g > 0.88$, CO emissions rapidly increase with increasing Φ_g. In contrast to the NO_x trends, the CO emissions do not show a substantial variation with the Reynolds number. In fact, the CO emission levels at high

equivalence ratios span over a wider interval for the Re = 20000 case than for Re = 10000. For both Reynolds number, the non-premixed pilot flame CO emissions are found higher than the ones for partially premixed pilot and without pilot flames. As compared to methane/air flames, the hydrogen-enriched flames are characterized by a significantly higher amount of CO emissions that decrease as the Φ_g increases. The high CO levels can be attributed to the poor combustion at close-to-LBO conditions.

The differences between the NO_x and CO level predictions from the numerical model (continuous line in Figure 5.11) and the experimental results can be related to the assumption of adiabatic flame in the numerical model. The heat exchange between the hot burner and the surrounding cold air has a strong impact on the flame temperature and thus the emission levels. In fact, the impact of heat transfer phenomena makes the water-gas shift reaction in favor of reduction of CO.

In agreement with the experimental trends, the 1D model takes into account the differences between the different mixtures and it is able to predict a lower emission level for hydrogen-enriched/methane flames as compared with pure methane flames. Furthermore, the numerical model captures the increasing NO_x and CO emission levels with increasing Φ_g. However, for hydrogen-enriched methane fuel mixtures, the numerical results predict lower level of CO emissions at low Φ_g suggesting that if the hydrogen-enriched flames were investigated under adiabatic flame conditions, the CO emission for these flames would be much lower than that in the methane/air flames. Therefore, the high level of CO emissions is the result of local flame extinction at close-to-LBO conditions.

Structures of Flow and Reaction Zones under Stable and Close-to-LBO conditions

To gain deeper understanding of the flame stabilization process, laser-based diagnostics experiments were carried out to investigate the impact of fully premixed pilot flame and hydrogen enrichment on the structures and stabilization of turbulent premixed methane/hydrogen/air flames in GTMC with the CeCOST burner. Two fuels are tested: methane and hydrogen-enriched/methane with a dilution of 50%. Measurements of velocity field and OH radicals distribution in the combustor are conducted using particle imaging velocimetry (PIV) and planar laser induced fluorescence (PLIF) methods, respectively. Flame are studied under stable and close-to-LBO conditions, at constant Reynolds number of 20000. The total amount of fuel and air injected into the combustion chamber is kept constant for all operating conditions. Two different pilot-to-global fuel

ratio were investigated (2% and 6%), keeping the pilot-to-global air ratio constant at 2%. A summary of the investigated configurations is presented in Table 5.3.

Table 5.3: Investigated flame conditions. For all flames investigated, the reactant mixture has an initial temperature of 298 K and the combustor is operated under atmospheric pressure.

Flame ID	$\dot{m}_{p,air}/\dot{m}_{g,air}$	$\dot{m}_{p,fuel}/\dot{m}_{g,fuel}$	Re
F1	0%	0%	20000
F2	2%	2%	20000
F3	2%	6%	20000

Figure 5.12 shows the effect of the pilot flame and the fuel mixture composition on the lean blow-off limits. During the experiments, the critical LBO equivalence ratio has been defined as the one at which the main flame-quenching event occurs. Similarly to what is shown in Figure 5.7 in Section 5,the critical LBO equivalence ratio shifts towards lower values when hydrogen is added to the fuel due to a higher diffusivity and a higher laminar burning velocity. As visible in Figure 5.12, the main flame equivalence ratio, Φ_{main} decreases at LBO conditions as the pilot fuel mass flow rate increases, thus the pilot flames tend to extend the operability range of the burner. However, when increasing the pilot mass flow rate ($\dot{m}_{p,fuel}/\dot{m}_{main}$) while keeping the total mass flow ($\dot{m}_{pilot} + \dot{m}_{main}$), the global equivalence ratio, Φ_g, shows a non-monotonic variation with the fuel mass flow rate of the pilot flames. The F2 flame tend to extend the operability conditions showing the same critical Φ at LBO conditions, however the F3 flame appear to be sensitive to the mass ratio of the pilot flame to the main flame. In fact, compared with F2 flames, the pilot fuel mass flow rate is higher, but also the critical Φ_g at LBO. The flame configuration F3 is shown to be able to extend the LBO limits in the hydrogen-enriched methane case only and this may be due to the pilot flames lifted off the pilot injector.

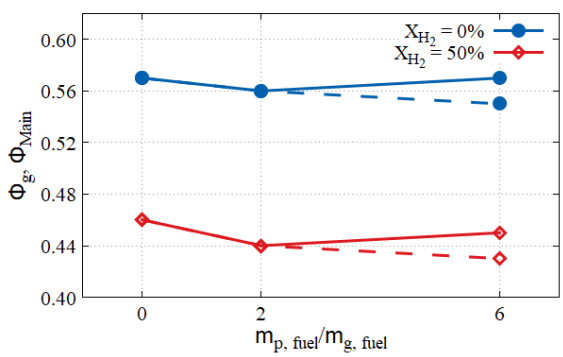

Figure 5.12: Lean blow-off limits for the investigated mixtures. The solid lines indicates results of the global equivalence ratio, Φ_g, and the dashed lines are for the main equivalence ratio, Φ_{Main}.

Based on the results from the stability map, optical diagnosis data were acquired for selected cases at stable and at close-to-LBO operating conditions. A summary of the selection is presented in Table 5.4. Due to the differences in operability ranges (see Figure 5.12), the global equivalence ratios are different for the two fuel mixtures.

Table 5.4: Investigated flame cases and experimental conditions. The laminar flame speed (S_L), laminar flame thickness (δ_L), adiabatic flame temperature (T_{ad}), and maximum OH radicals mass fraction ($Y_{OH,max}$) are calculated using Cantera [166] and the GRI-3.0 chemical kinetic mechanism [167] on the planar free propagating flame configuration for the corresponding mixture under conditions of Φ_g, initial temperature 298 K and 1 atm.

Cases	Flame ID	Operability	X_{H_2}	Φ_g	Φ_{Main}	Φ_{Pilot}	S_L [cm/s]	δ_L [mm]	T_{ad} [K]	$Y_{OH,max}$	Ka
SMF1	F1	Stable	0	0.72	0.72	-	20.88	0.64	1869	4.32×10^{-3}	0.84
SMF2	F2	Stable	0	0.72	0.72	0.72	20.88	0.64	1869	4.32×10^{-3}	0.84
SMF3	F3	Stable	0	0.72	0.69	2.16	20.88	0.64	1869	4.32×10^{-3}	0.84
LMF1	F1	close-to LBO	0	0.64	0.64	-	14.48	0.84	1732	2.91×10^{-3}	1.68
LMF2	F2	close-to LBO	0	0.64	0.64	0.64	14.48	0.84	1732	2.91×10^{-3}	1.68
LMF3	F3	close-to LBO	0	0.64	0.61	1.92	14.48	0.84	1732	2.91×10^{-3}	1.68
SHF1	F1	Stable	50%	0.52	0.52	-	10.83	1.04	1547	1.64×10^{-3}	2.88
SHF2	F2	Stable	50%	0.52	0.52	0.52	10.83	1.04	1547	1.64×10^{-3}	2.88
SHF3	F3	Stable	50%	0.52	0.50	1.56	10.83	1.04	1547	1.64×10^{-3}	2.88
LHF1	F1	close-to LBO	50%	0.46	0.46	-	5.82	1.71	1430	0.83×10^{-3}	9.42
LHF2	F2	close-to LBO	50%	0.46	0.46	0.46	5.82	1.71	1430	0.83×10^{-3}	9.42
LHF3	F3	close-to LBO	50%	0.46	0.44	1.38	5.82	1.71	1430	0.83×10^{-3}	9.42

Figure 5.13 shows a sequence of five instantaneous snapshots of OH-PLIF images for the CH_4/air flames under close-to-LBO (rows one to three) and stable (rows four to six) operating conditions. A lower OH-PLIF signal intensity is visible for the three close-to-LBO cases than the corresponding three stable flames. Furthermore, the discontinuities of the OH layer indicates a local extinction of the reaction zones, which is partly due to the leaner mixture at close-to-LBO conditions. Results from numerical simulations for the planar laminar premixed flame configuration (listed in Table 5.4) show that the peak of OH mass fraction, $Y_{OH,max}$, and the laminar flame speed, S_L, for the close-to-LBO case are about 33% and 30% respectively lower then the sable case. Furthermore, the laminar flame thickness, δ_L, for close-to-LBO flames is $\approx$ 31% higher than the corresponding for stable flame conditions. Therefore, the combined effect of lower reactivity, low flame temperature (cf. Table 5.7), low flame speed, and thicker flame explain why the close-to-LBO flames exhibit regions of local flame extinction.

The impact of pilot flame is also visible in Figure 5.13. At stable and close-to-LBO condition flames, the OH-PLIF signal is visible shortly downstream of the pilot flame nozzles. Due to the high injection speed, the OH radical formed by the pilot flames are transported downstream the injection nozzle, improving the main flame stabilization in the outer recirculation zone. The overall flame shape appears to be an M-shape flame structure. This flame structure is more evident in the in the piloted flames than in the non-piloted flame and this is why the

pilot flames can extend the operability of the main flame to lower equivalence ratios. In fact, at close-to-LBO conditions the OH radicals generated in the pilot flames tend to anchor the main flame in the ORZ.

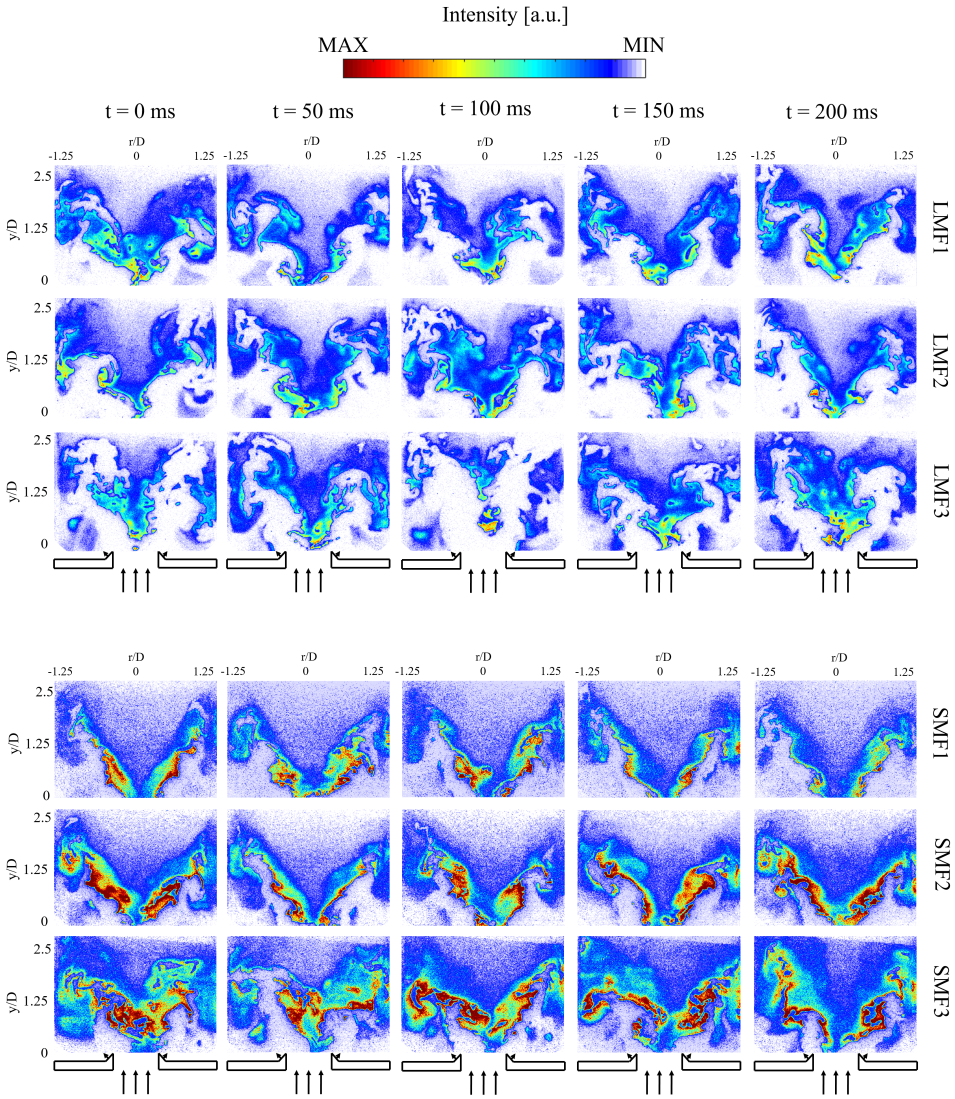

Figure 5.13: Instantaneous OH-PLIF snapshots for the close-to-LBO (LMF1, LMF2 and LMF3) and stable (SMF1, SMF2 and SMF3) cases for methane flames. r and y indicate radial and axial directions, respectively.

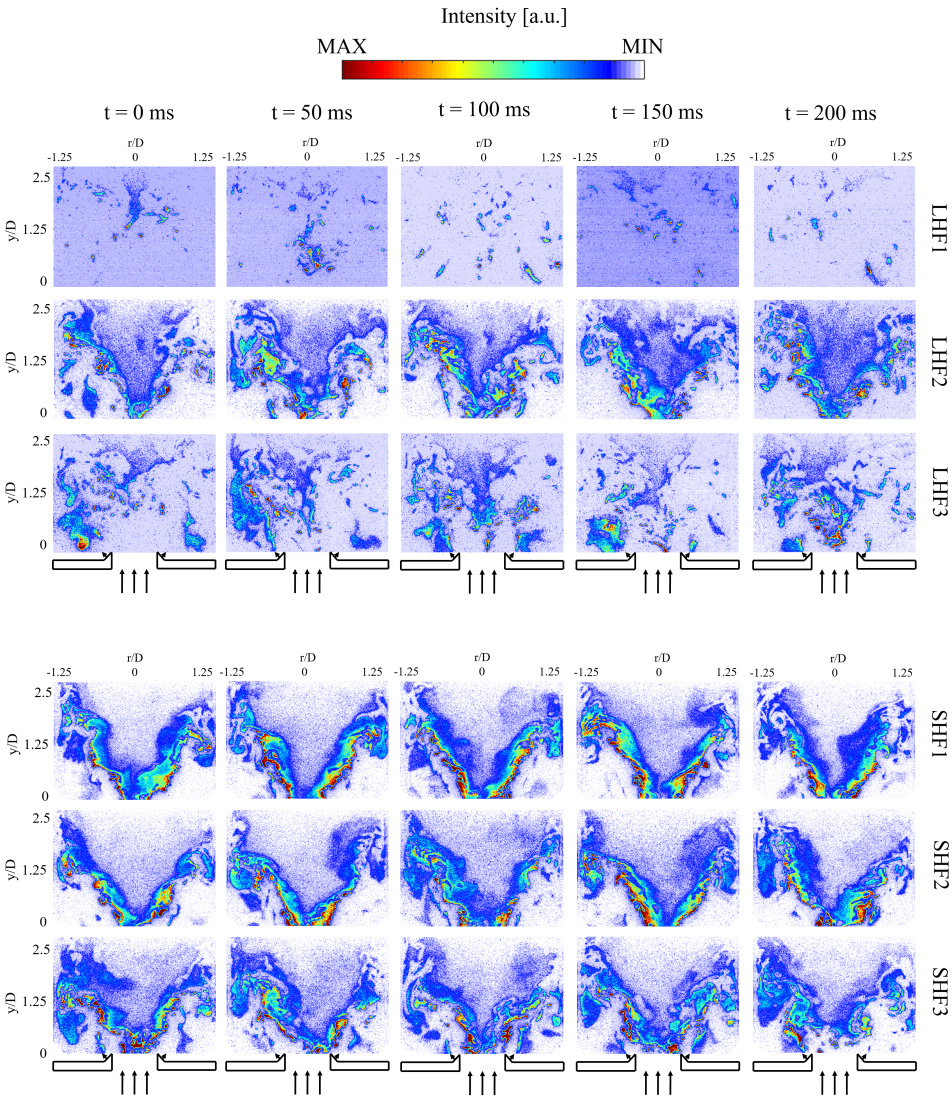

Figure 5.14: Instantaneous OH-PLIF snapshots for the close-to-LBO (LHF1, LHF2 and LHF3) and stable (SHF1, SHF2 and SHF3) cases for hydrogen-enriched methane flames. r and y indicate radial and axial directions, respectively.

Figure 5.14 shows a sequence of five instantaneous snapshots of OH-PLIF images for the H_2/CH_4/air flames under close-to-LBO (rows one to three) and stable (rows four to six) operating conditions. For LHF1, the OH signal is very weak and appears as small isolated OH pocket. When pilot flame is used (LHF2 and LHF3), the OH signal is visibly stronger. The hot gas and OH radicals generated by the pilot flame case are able to ignite the the main flame. In the

LHF3 case, the strong OH-PLIF signal in the outer recirculation zone is due to the fuel-rich mixture from the pilot mixing with the fuel-lean mixture from the main flame, forming a local close-to-stoichiometric pilot flame in the ORZ. However, the main flow is under ultra-lean conditions, thus the combustion of the main flame is rather low and it proceeds in isolated pockets.

Overall, the hydrogen-enriched flames show a rather discontinuous OH layers and it is likely due to a combined effect of turbulence and diffusive-thermal instability in lean premixed flame with hydrogen content in the mixture. By looking at Table 5.4, the hydrogen-enriched flames generally have a larger Karlovitz number than the corresponding methane cases, in a range from 2.88 and 9.42. Thus, these flames belong to the thin reaction zone regime, although the flame pocket structure is not predicted for this regime. Furthermore, due to the differential diffusion of hydrogen flames, the OH signal has stronger variations than the corresponding cases for methane.

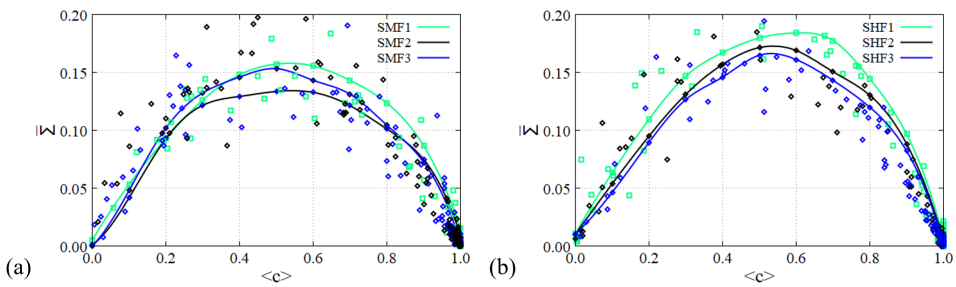

Figure 5.15: Mean flame surface density against mean progress variable for the stable CH_4/air flames (left) and H_2-enriched CH_4/air flames (right).

Figure 5.15 shows the mean flame surface density (FSD), $\bar{\Sigma}$, plotted versus the mean progress variable, $\langle c \rangle$. Details regarding how these quantities are computed are provided in Appendix B. Due to the tendency of flame front to be discontinuous, the analysis of this quantities is applied to the investigated stable flames only. It is visible that the mean FSD profiles are almost symmetric, reaching a maximum value at $\langle c \rangle \approx 0.5$, with the exception of case SHF1 having a maximum value is at $\langle c \rangle \approx 0.7$. Values decrease as the pilot fuel rate increases, highlighting an increase in the flame distribution area. This indicates that the FSD tends to be more disperse. Furthermore, the H_2-enrichment case attain higher values as compared to the corresponding methane case. This trend can be explained by the the generation of smaller-scale flame elements due to the hydrogen content in the mixture.

Figure 5.16 shows the probability density function(PDF) of flame front curvature.

The methodology used to extract the curvature values from the OH-PLIF data is discussed in the Appendix B. It is visible that the all the PDF trend are approximately symmetric with the PDF peak around 0, with the exception of case LHF1. In fact, the OH radicals form small pockets which tend to result in positive values of k. The PDF peaks of the hydrogen-enriched methane/air cases are lower than the corresponding methane/air cases. This due to flame wrinkling effect due to the hydrogen content in the mixture, spreading the PDF to larger curvature values, indicating the existence of smaller wrinkle scales for these flames. A similar effect on the PDF trend is given by the pilot flame employment.

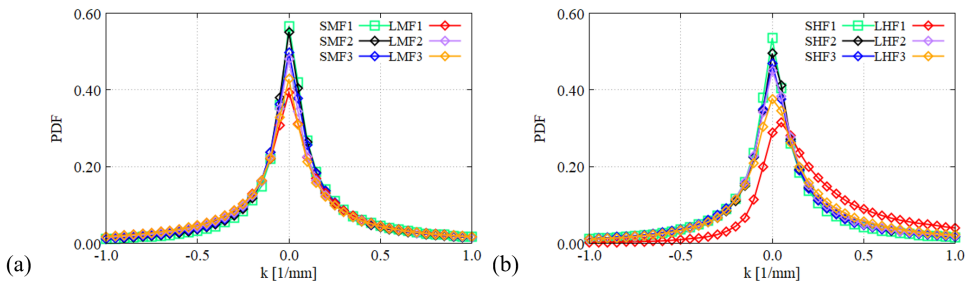

Figure 5.16: Probability density function (PDF) of flame front curvature for (a) pure methane and (b) hydrogen-enriched methane flames listed in Table 5.7.

Figure 5.17 and 5.18 show a sequence of three instantaneous snapshots of simultaneous PIV and OH-PLIF fields for CH4/air and H2-enriched CH4/air mixtures, respectively. The solid lines represent the IRZ (around the burner axis) and the ORZ (in the low-left and in the low-right corners of the combustor). In the LMF1 and LMF2 cases, the equivalence ratio of the main flame as well as the laminar flame speed (see Table 5.4) are high enough that the flame propagates upstream to the shear layer between the IRZ and ORZ. This is not visible in case LHF3 for which the OH-PLIF signal is primarily found in the IRZ and ORZ, due to the lower main flame equivalence ratio and the lower laminar flame speed. The pilot flame have a significant impact on the flow field. In fact, the IRZ size decreases as the mass flow rate of pilot flames increases. It seems that when the OH radicals moves upstream to the shear layer, the hot gas expansion may affect the pressure field, which consequently affects the vortex breakdown process. This is visible for stable flames SMF1, SMF2 and SMF3. In these cases, due to the higher equivalence ratio and thus higher laminar flame speed than the close-to-LBO flames, the reaction zone moves further upstream into the high-speed shear layer between the IRZ and ORZ. This results in an IRZ larger than the one in the close-to-LBO flames.

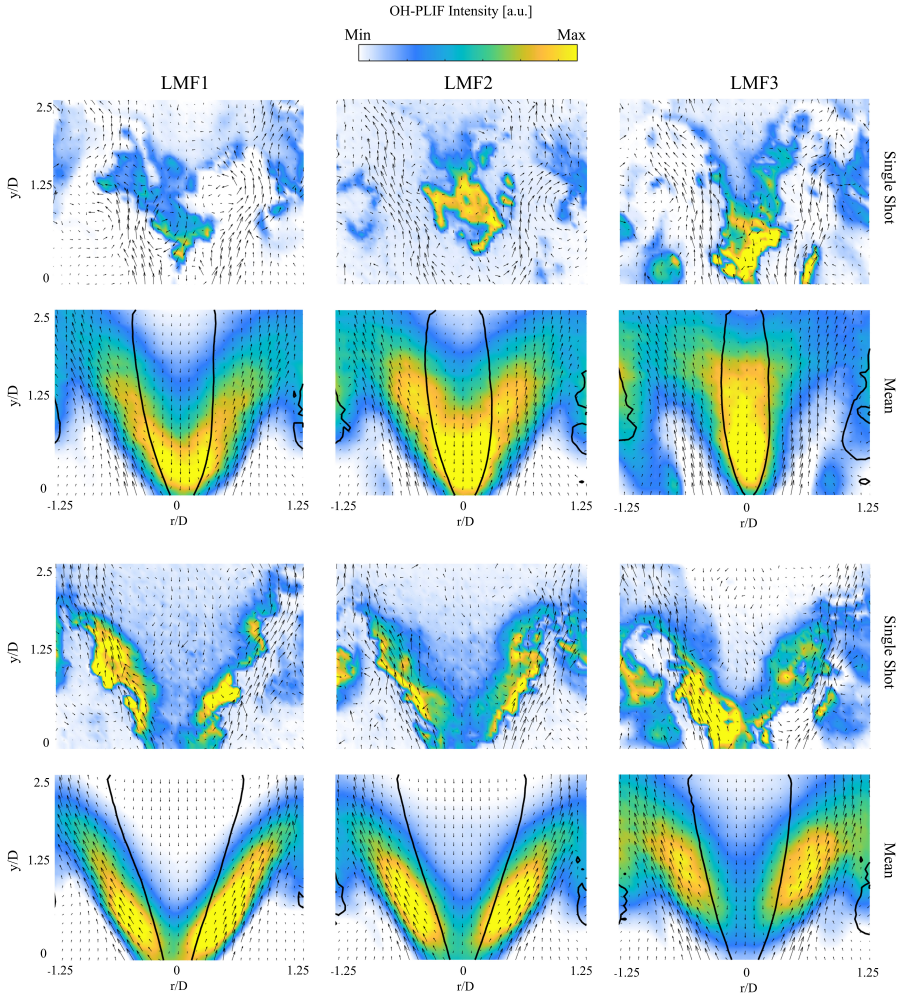

Figure 5.17: Snapshots of simultaneous velocity vectors and OH PLIF signal intensity (first and third rows), and ensemble averaged velocity and OH PLIF fields (second and fourth rows), for the stable and close-to-LBO methane flames. r and y indicate the cross-flow and axial directions, respectively. The solid lines indicate zero velocity iso-contours.

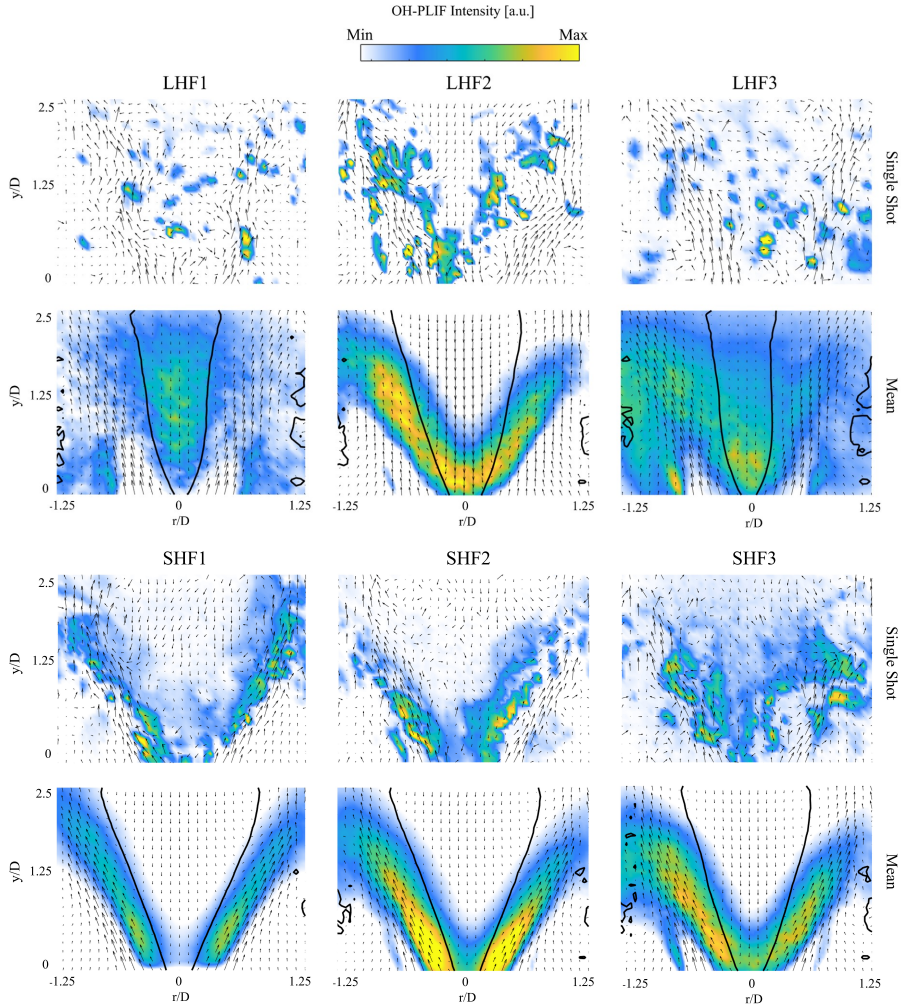

Figure 5.18: Snapshots of simultaneous velocity vectors and OH PLIF signal intensity (first and third rows), and ensemble averaged velocity and OH PLIF fields (second and fourth rows), for the stable and close-to-LBO methane/hydrogen flames. r and y indicate the cross-flow and axial directions, respectively. The solid lines indicate zero velocity iso-contours.

The instantaneous OH field and velocity vector are highly correlated. This indicates a strong flo/flame interaction. The local velocity is followed by the OH layer wrinkling. By looking at the close-to-LBO mean flame/flow fields, it is visible that the LBO process starts with the reaction zone moving from the upstream shear layer to the downstream IRZ. Then, the concentration of the OH radical, and therefore the reaction rate and the heat release, further decreases as the equivalence ratio decreases. Although the OH layer is stabilized in the IRZ, the eventual local extinction of the flame in this region leads to the extinction

of the flame.

The flame structure of the hydrogen-enriched methane flames is significantly different. At close-to-LBO conditions, the OH is spread in a wider region, in the IRZ but also in the shear layers. The OH signal appear discontinuous and as isolated pockets in the close-to-LBO conditions but also for the stable flame cases. The size of the IRZ is strongly correlated to the heat release zone; in fact, due to the upstream propagation of the heat release zone in the shear layer, the size of the IRZ becomes larger.

Impact of Pilot Flames on Nozzle Temperature

In this paper, the surface temperature of the pilot nozzle of the CeCOST burner (see Figure 4.3 in Section 4) is measured using lifetime phosphor thermometry with ZnS:Ag phosphor [168]. Three pilot nozzle configurations including a non-premixed (DP1), a partially premixed (PP2) and a fully premixed (PP3) pilot flames are investigated. Furthermore, the burner is operated at constant Reynolds number (equal to 20000), at stable flame conditions with pure methane and hydrogen-enriched methane (50% in volume). The differences in stability map shown in Figure 5.7 does not allow the comparison at the same equivalence ratio. Therefore, by defining the global equivalence ratio, Φ_g, based on the total amount of fuel ($\dot{m}_{main,fuel}+\dot{m}_{pilot,fuel}$) and air ($\dot{m}_{main,air}+\dot{m}_{pilot,air}$) injected in the combustion chamber, the comparison between the two mixture is conducted at Φ_g equal to 0.72 for the pure methane case and to 0.52 for H_2-enriched case. At these two Φ_g the corresponding flames are found to be stable in the combustion chamber. Experiments are performed while keeping the total amount of fuel and air injected into the combustion chamber constant and routing air and fuel from the main into the pilot flame at different percentages. The selected percentages are shown in Table 5.5

Table 5.5: Properties of the investigated pilot injection strategies. The equivalence ratio of pilot and main flames is also included.

Injection Strategy	Pilot Air (%)	Pilot Fuel (%)	Φ_{main,CH_4}	Φ_{pilot,CH_4}	$\Phi_{main,CH_4/H_4}$	$\Phi_{pilot,CH_4/H_2}$
A1F6	1	6	0.68	4.32	0.49	3.12
A2F6	2	6	0.69	2.16	0.50	1.56
A2F2	2	2	0.72	0.72	0.52	0.52
A2F0	2	0	0.74	0	0.53	0
A0F0	0	0	0.72	0	0.52	0

Figure 5.19 shows the location of the 33 investigated points distributed in three rows at the same azimuthal angle of the pilot nozzle. Two pilot nozzles are included in the field of view at -22.5° (left nozzle) and 22.5° (right nozzle).

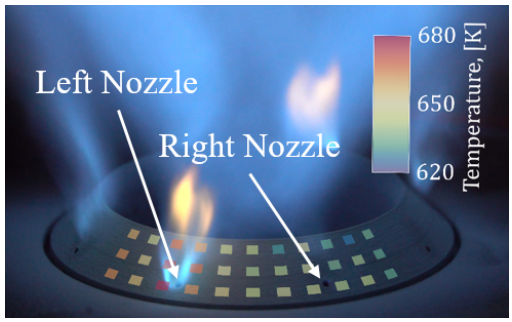

Figure 5.19: Distribution of the 33 investigated points located in three rows at the same azimuthal angle of the pilot nozzle. Furthermore, indications of the left and the right nozzles are included.

Figure 5.20 shows the surface temperature results for DP1, PP2 and PP3, for the CH_4 (left) and H_2/CH_4 (right) fuel mixtures and for all the injection strategies listed in Table 5.5.

For DP1 pilot flame configuration, the highest temperature is reached by A0F0 and A1F6 cases for pure methane and hydrogen-enriched methane fuels, respectively. The difference in which case shows the highest temperature between the two mixtures can be attributed to the heat output of pure methane case mainly dominated by the main flame, whereas for the hydrogen-enriched case the heating from the pilot plays a relevant role. This is also supported by Figure 5.21 where it is visible that the pilot flame in the hydrogen-enriched case tend to be more attached to the nozzle than in the pure methane case. This also explains why the temperature in the points around the pilot nozzles in Figure 5.20 are higher than the ones further from the injectors in the H_2-enriched case. The pure methane results are approximately at the same temperature since the pilot flames are in general lifted off, and the air and fuel flowing in the nozzle cool down the walls.

The surface temperature of the non-premixed pilot flame configuration decreases from the left nozzle to the right by more than 20 K for all the cases involving the injection of pilot air (injection strategies A1F6, A2F6, A2F2 and A2F0) for both the fuels considered in this thesis. Reasonably, this trend is due to the cooling effect by the pilot air flowing through the air channels inside the burner nozzle. In fact, pilot air and fuel enter the burner nozzle plate at room temperature in separate pipelines as in Figure 4.3 in Section 4. The air flowing through the inner channel of the pilot nozzle is heated up as it travels to the left (from the perspective of Figure 5.21). Thus, the cooling effect from pilot air is more effective on the right side of the burner. So, the design of the pilot piping is important to achieve uniform temperatures.

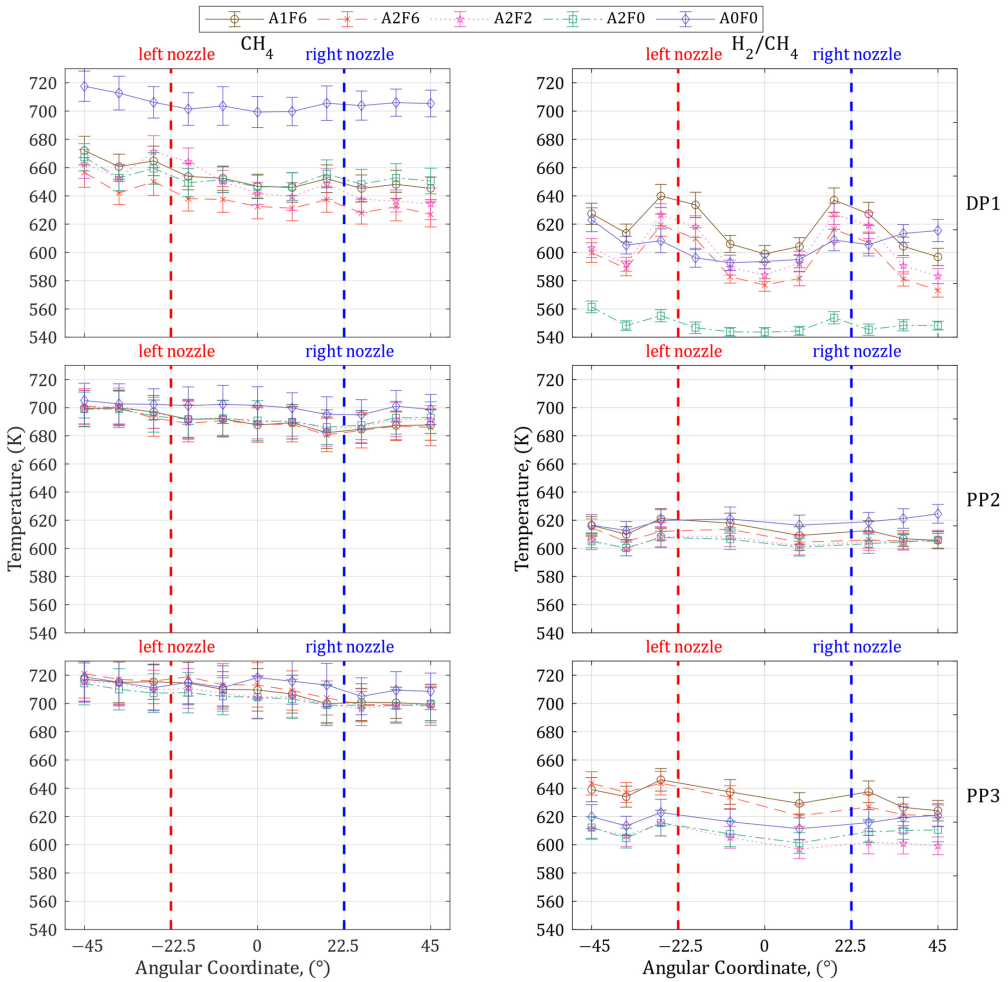

Figure 5.20: Surface temperatures trends for DP1, PP2, and PP3 pilot flame configurations for methane (left) and hydrogen-enriched methane (right) mixtures. The red-dashed vertical lines represent the position of the left nozzle in the field of view of the temperature measurement, while the blue vertical line indicates the right nozzle. The pilot injection strategy listed in Table 5.5 is shown by the legend.

According to Figure 5.20, the lowest temperature for the pure methane case is A2F6, while the one for hydrogen-enriched methane is A2F0. In the first case, the high pilot air and fuel flow reduces the heat load from the main combustion nozzle, while in the second case the pilot air decreases the nozzle temperature and the absence of fuel injected results in no pilot flame able to heat up the nozzle. The generally lower temperature of the hydrogen-enriched methane case is related to the lower heat output of the burner due to the lower equivalence ratio.

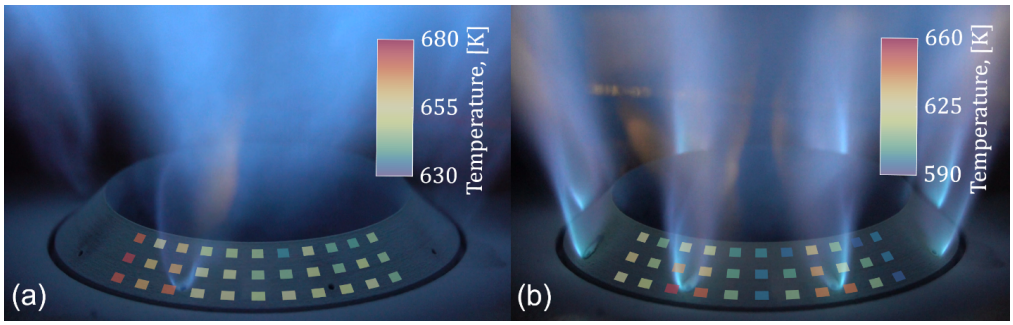

Figure 5.21: Time averaged images of the non-premixed pilot flame nozzle (DP1) and measured surface temperature for injection strategy A1F6 for (a) pure CH_4 and (b) H_2-enriched/CH_4 fuel mixtures.

Figure 5.20 shows that the range of spread in surface temperature for the different pilot injection cases for PP2 and PP3 is smaller as compared to the DP1 pilot configuration. This is due to the lower cooling effect of pilot air for PP2 and PP3 as compared to DP1 configuration because the pilot air injection is more uniform and it is injected from a lower position in DP1, as visible in Figure 4.3. The lower injection point of the air forms an air film over the DP1 nozzle which is absent for PP2 and PP3. Furthermore, as visible in Figure 5.22, the pilot flames do not attach to the nozzle surface for PP2 and PP3 pilot flame configurations when operated with CH_4. This results in the main flame dominating the surface heating and therefore the surface temperature is rather insensitive to the amount of pilot air and fuel for the PP2 and PP3 cases. The low level of premixing of the PP2 pilot flame configuration leads to a small impact of the pilot flame on the surface temperature of the nozzle in the H_2-enriched/methane case as well. As it is visible in Figure 5.22.c, the pilot flames are relatively distant from the nozzle, thus the heating by the pilot is lower than the PP3 pilot configuration in Figure 5.22.d.

Based on the results in Figure 5.20, the highest temperature for methane flames for PP2 and PP3 is observed in case A0F0. This result is in line with the findings from the DP1 pilot flame configuration. Due to the smaller contribution of the pilot flame on heating the PP2 nozzle, the hottest condition with H_2/CH_4 mixture is found for the no pilot case A0F0. For PP3, the A1F6 is the hottest case. This results in a surface temperature being $\approx$ 20 K higher than in the PP2 configuration when comparing the A1F6 and A2F6 pilot cases. This can be explained by the higher degree of fuel/air mixing of PP3 configuration. The pure methane fuel results related to DP1 are found approximately 40 K cooler than the PP2 configuration, for all the cases involving pilot air injection. This is due to the strong cooling effect that the air flow has on the nozzle walls since the pilot flames are lifted off in the DP1 case. This cooling air film is not as effective

in the partially premixed pilot flame configurations. In hydrogen-enriched cases, the differences between DP1 and PP2 are found less that 20 K for cases involving pilot flames. This is due to the increased heating counteracting the cooling from the pilot air injections.

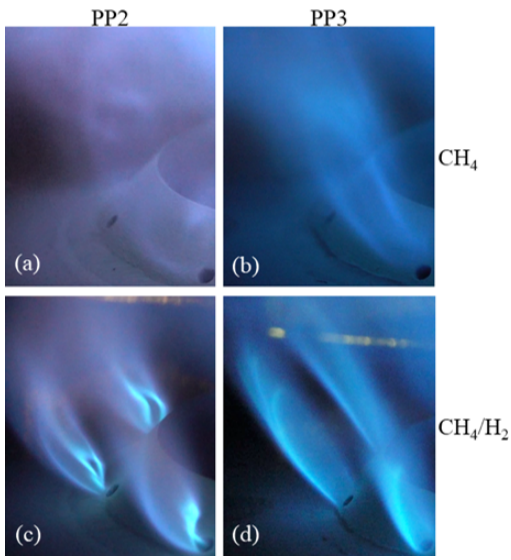

Figure 5.22: Instantaneous snapshots of pilot flames for the injection strategy A1F6 of CH_4 fuel (top row) and of H_2/CH_4 fuel mixture (bottom row) for PP2 (left) and PP3 (right).

CO_2 Diluted Syngas/Air Flames in a Gas Turbine Model Combustor

The impact of CO_2 dilution on the combustion of a syngas mixture is investigated experimentally in the CeCOST burner under atmospheric pressure conditions, operating the burner at constant Reynolds number of 10000. The optical techniques here employed are simultaneous OH-PLIF and PIV and OH* Chemiluminescence. Table 5.6 lists the composition of the three CO_2-enriched syngas mixtures investigated in this thesis. The baseline mixture (SYN0) consists of 0% CO_2, 3% CH_4, 44% CO and 53% H_2 and it is referred to as pure "syngas". The mixtures denoted as SYN15 and SYN34 consist of the pure syngas diluted with 15% and 34% CO_2, respectively.

Table 5.6: Compositions and stoichiometric fuel/air mole ratios ($FA_{mole,s}$) of the three investigated syngas mixtures.

Mixtures	CH_4 [%]	CO [%]	H_2 [%]	CO_2 [%]	$FA_{mole,s}$
SYN0	3	44	53	0	0.3855
SYN15	2.55	37.4	45.05	15	0.4233
SYN34	2	29	35	34	0.5836

Figure 5.23 shows .a the laminar flame speed (S_L), .b the adiabatic flame temperature (T_{ad}), and the maximum mole fractions of .c H, O, and .d OH radicals for different equivalence ratios Φ. Numerical results refer to a freely propagating planar laminar premixed flame under adiabatic conditions performed using the Cantera code [166] coupled with the GRI-3.0 mechanism [167] for the chemistry representation. It is visible that the laminar flame speed and the adiabatic flame temperature increase with the equivalence ratio while they decrease with increasing CO_2 dilution. Furthermore, the mass fraction peak of H, O and OH decreases with the carbon dioxide content in the mixture. These results are related to the CO_2 suppression of the chemical reactivity of the mixture due to the reduced heat of combustion of the syngas mixture, which leads to a lower adiabatic flame temperature and lower concentrations of radicals. This decreases the laminar flame speed also. The high content of H_2 and CO in the mixture shifts the laminar flame speed peaks at fuel-rich mixtures and, therefore, it increases with the H_2 content in the mixture [65, 66].

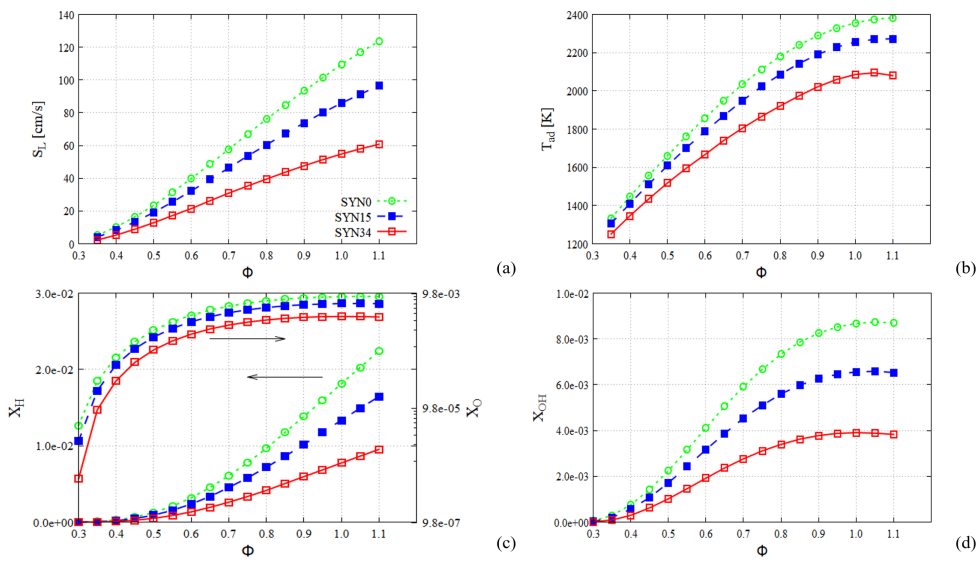

Figure 5.23: 1D numerical predictions of (a) Laminar flame speed (S_L), (b) adiabatic flame temperature (T_{ad}), (c) maximum mole fraction of H (X_H) and O (X_O, plotted in logarithmic scale) and (d) maximum mole fraction of OH (X_{OH}) as functions of the equivalence ratio, Φ, at atmospheric pressure and room temperature (1 bar and 298K) for the syngas mixtures in Table 5.6.

Figure 5.24 shows that the burner stability range shifts toward rich mixtures as the CO_2 dilution increases, see also Table 5.7. Due to the combined thermal and chemical effects of carbon dioxide dilution on the mixture, the LBO and flashback limits do not vary linearly. Based on 5.23.b, the adiabatic flame temperature at Φ_{LBO} for 0% and 15% CO_2 are rather close and this suggests that the thermal effect is the one that mainly controls the LBO process at low level of CO_2 dilution.

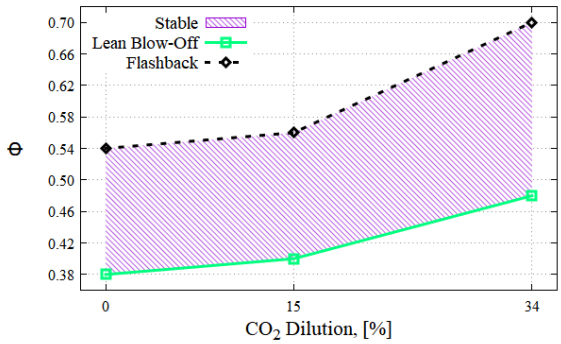

Figure 5.24: Operability limits for the three different CO_2 dilutions.

The chemical effect is visible at 34% CO_2 dilution, where the adiabatic flame temperature at LBO is significantly higher than the one for low CO_2 dilution content. The chemical effect is related to the capability of CO_2 to participate in the chemical reactions, mainly in the reaction CO + OH = CO_2 + H [169, 170], decreasing the concentrations of OH and O radicals, thus the reactivity of the H + O_2 + M → HO_2 + M recombination reaction, reducing the level of available H radicals and affecting the branching reaction H + O_2 ↔ O + OH [60, 70, 72].

Table 5.7: Numerical prediction of laminar flame speed [cm/s], adiabatic flame temperature [K], and maximum mole fraction of OH for the experimentally measured equivalence ratios at lean blow-off limit and flashback limit for different syngas mixtures.

Mixtures	Φ_{LBO}	$S_{L,LBO}$	$T_{ad,LBO}$	$X_{OH,LBO}$	Φ_{FB}	$S_{L,FB}$	$T_{ad,FB}$	$X_{OH,FB}$
SYN0	0.38	8.08	1402	$0.60*10^{-3}$	0.54	30.51	1751	$3.01*10^{-3}$
SYN15	0.40	8.22	1410	$0.56*10^{-3}$	0.56	26.84	1717	$2.61*10^{-3}$
SYN34	0.48	11.25	1484	$0.85*10^{-3}$	0.70	30.87	1804	$2.72*10^{-3}$

The CO_2 dilution effect is visible also on the flame luminescence, as it is visible on Figure 5.25 where a sequence of instantaneous flame luminescence images are shown, for the SYN0 and SYN34 flames for an equivalence ratio of $\Phi = 0.53$. It is visible how the intensity of the flame luminosity is significantly lower in the 34% CO_2 case than in the pure syngas case, consistently with the decrease

in H, O and OH radical concentration. The flame structure is quite fine and the leading front position of the flame appears to oscillate in the axial direction. This can be related to the local flame extinction and re-ignition due to the high-level of CO_2 dilution suppressing the fuel/air mixture reactivity making the flame vulnerable to local extinction.

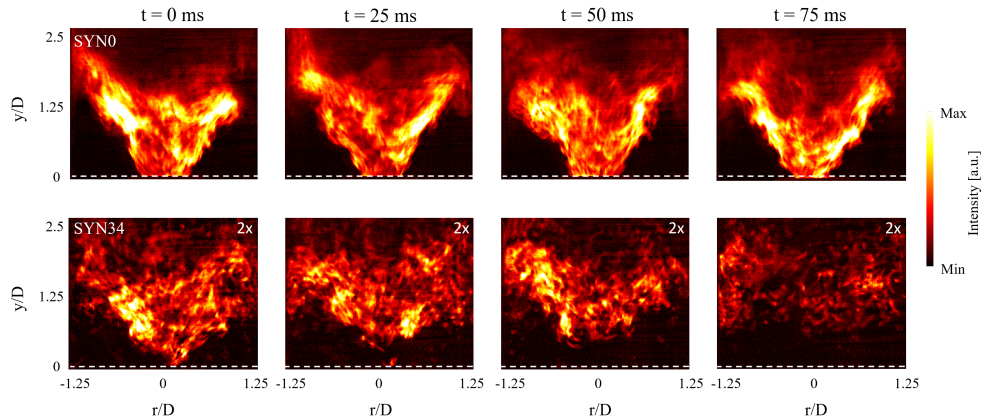

Figure 5.25: Instantaneous flame luminescence sequence for SYN0 (top) and SYN34 (bottom) mixtures under the condition of $\Phi = 0.53$. The luminosity of the SYN34 flames has been amplified by a factor of 2. r and y indicate radial and axial directions, respectively.

Due to the differences in the operability range, PIV and OH-PLIF data were acquired for three syngas mixtures under conditions of similar adiabatic flame temperature (T_{ad}) and laminar flame speed (S_L). Figure 5.26 shows the variation of the adiabatic flame temperature as a function of the laminar flame speed. The selected flame conditions consisted in $T_{ad} = 1600$ K with a maximum difference between the SYN0 and SYN34 mixtures of 9.61 K. The selected laminar flame speed varied between 0.181 m/s and 0.191 m/s. Under these conditions, the equivalence ratios are equal to 0.47, 0.50 and 0.56 for SYN0, SYN15 and SYN34 mixtures, respectively.

Figure 5.27 shows a sequence of four instants of time related to the selected three syngas flames. It is visible that the mixture without any CO_2 dilution, exhibits a rather continuous OH radical distribution. The OH structure becomes more discrete as the CO_2 dilution in the mixture increases, and it is found forming isolated combustion pocket regions. This flame structure is caused by the local quenching of reactions in the presence of high level of CO_2. In the SYN0 flames, the OH signal is quite low, however it shows high intensity islands connected to the low intensity regions. This can be attributed to the diffusional-thermal flame instability that can be observed in lean hydrogen premixed flames [171].

Since the hydrogen diffusion coefficient is higher than the one of the other major species in the flame, the hydrogen molecules tend to diffuse to rich fuel pockets islands where the local reaction activity is significantly high. As the level of CO_2 in the mixture increases, the originally weak OH regions are further suppressed and local extinction occurs in a wide region, leaving the burning pockets isolated.

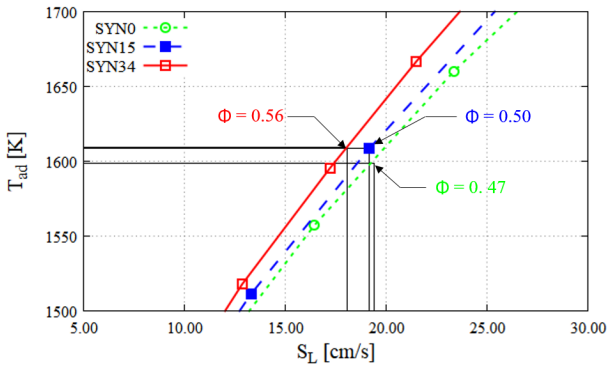

Figure 5.26: Adiabatic flame temperature (T_{ad}) as a function of laminar flame speed S_L based on the numerical results shown in Fig. 5.23. The arrows indicate the PIV and OH PLIF experimental points.

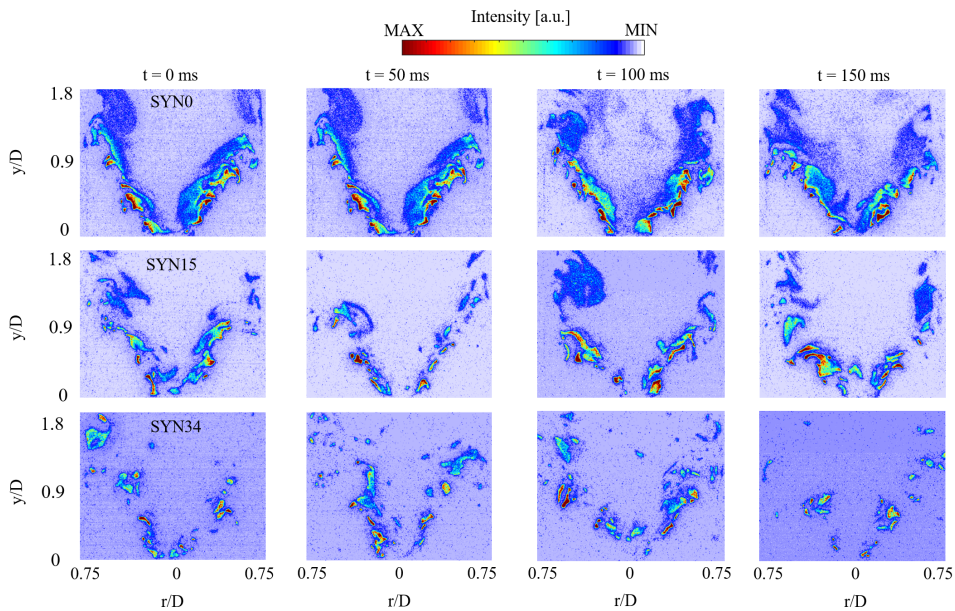

Figure 5.27: Instantaneous OH-PLIF snapshots for the SYN0 flames at $\Phi = 0.47$ (top), the SYN15 flames at $\Phi = 0.50$ (middle) and the SYN34 flames at $\Phi = 0.56$ (bottom). r and y indicate radial and axial directions, respectively.

Based on the definition of Peters [27] and the PIV data collected, an estimation of the Karlovitz (Ka) number indicates values of 0.489, 1.06 and 1.16 for the SYN0, SYN15 and SYN34 flames, respectively, meaning that the flames investigated here belong to the flamelet regime [27]. However, the flame structure shown in Fig. 5.27 significantly differ from the common structure of flamelet combustion.

The PIV field shows the IRZ around the centerline of the combustor, as well as the outer recirculation zones (ORZ) in the lower-left and lower-right corners of the combustor. The reaction regions indicated by the OH-PLIF signal are located in the inner shear layer between the main flow stream and the inner recirculation zone. It can be observed that the strain rate field does not correlate neither with the reaction region of the flame nor with the quenched region. Therefore, the local extinction can not be due to the high strain rate. Therefore, the onset of flame pocket structure is due to the diffusional-thermal flame instability which is amplified by the suppression of reactivity by CO_2 dilution.

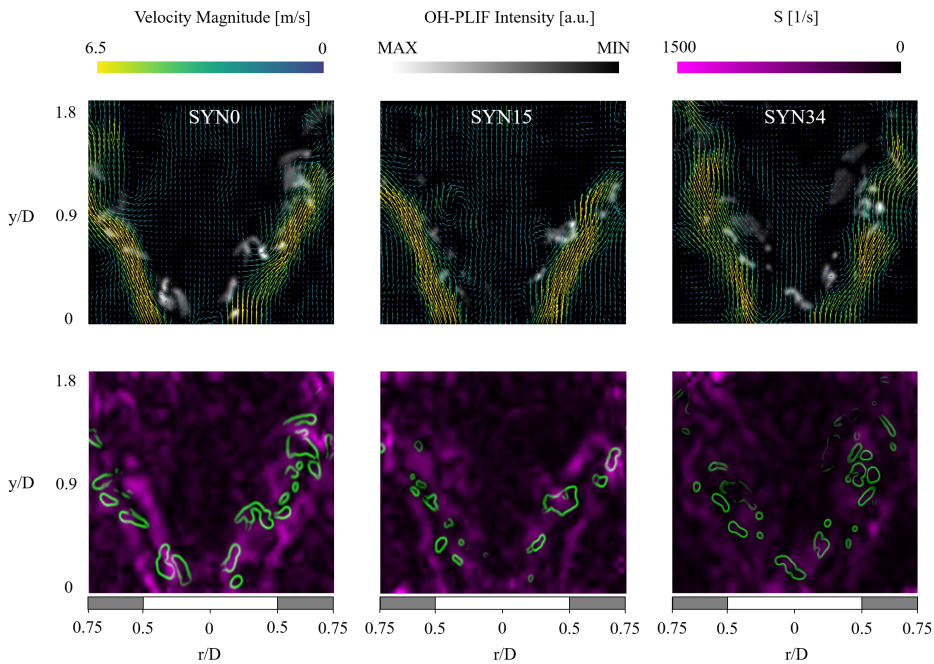

Figure 5.28: Instantaneous flow field (colored with the velocity magnitude) superimposed to the corresponding instantaneous OH-PLIF snapshot (top row), and OH-PLIF maximum gradient field overlapped to the corresponding strain field (bottom row) for the SYNO flame at $\Phi = 0.47$, SYN15 flame at $\Phi = 0.50$ and SYN34 flame at $\Phi = 0.56$, respectively. r and y indicate radial and axial directions, respectively.

Chapter 6

Conclusions and Future Outlook

6.1 Conclusions

In this thesis, direct numerical simulation (DNS) and laser-based diagnostics experiments have been carried out to investigate the propagation of turbulent premixed flames in a generic configuration and a gas turbine model combustor. The aim is to gain a deeper understanding of flame propagation, flame/turbulence interaction, and the impact of different fuels on flame stabilization and pollutant emissions in gas turbine engine-relevant combustors.

In the first part of this thesis (**Paper I**), the effect of the thermal expansion due to heat release on the propagation of the premixed reacting wave is studied. The analysis mainly focuses on the density-weighted displacement speed ($\check{s}_d$) and its related contributions (curvature, normal diffusion, and reaction). A set of the diagnostic equation is applied to a DNS database composed of four statistically-planar reaction waves propagating into a homogeneous turbulence field. The main findings can be listed as follows:

- Positive and negative displacement speeds are detected. It is visible that a premixed flame (also referred to as a deflagration wave or a wave) propagating at a large positive/negative displacement speed, i.e., advancing/retreating with respective to unburned reactant mixture, tends to accelerate towards more positive/negative flame speeds. These processes are highly dependent on the curvature contribution that also partially

counteract the resisting contributions due to normal diffusion and reaction. Surface elements having a large positive or a large negative curvature are found to be curved more positively or negatively, respectively. Furthermore, a thickened surface element tends to increase its thickness, and surface elements likely to lose their area tend to accelerate till vanishing.

- The turbulence inhibition toward the product side due to flow dilatation and viscosity increasing across the reacting wave reduces the extent of the detected acceleration processes in the reaction zone and at a high-density ratio. The turbulence inhibition is also found as the main reason for surface curvature to skew toward negative values in the reaction zone.

- The surface-averaged rate-of-change term for displacement speed, curvature, and wave thickness remains positive across the reaction wave in all the investigated conditions. The attained values are found to drop with an increase in density ratio. The averaged dilation-product term also remains positive; however, its value increases with a rise in density ratio. In the preheat zone, the surface-averaged rate-of-change in displacement speed is primarily contributed by curvature.

In the second part of the thesis (**Paper II**, **Paper III** and **Paper IV**), the effects of pilot flames and hydrogen-enrichment in methane fuel on the flame structures and stabilization in a lab-scale swirl burner (the CeCOST Burner) are investigated using experimental diagnostic techniques. The following conclusions are drawn:

- The full operability range extends with increasing Reynolds number and at higher methane content in the fuel mixture. The stable operability conditions shift toward leaner mixtures when H_2 is added to the methane/air mixture. The pilot flames are found to extend the burner's lean blow-off (LBO) limits. The impact of the pilot flame is found to be more evident when the pilot and main flames burn at the same equivalence ratio. However, due to the location of pilot flames in the combustion chamber with respect to the main flame, these cannot influence the flashback process.

- Pilot flames are found to lift off the pilot burner orifice. Statistics reveal that the probability of pilot flame burning attached to the pilot nozzle orifice decreases for higher values of equivalence ratio, for higher Reynolds number, and when premixed pilot flame is used. The onset of lift-off needs to be attributed to a higher pilot jet velocity. Furthermore, the H_2-enrichment leads to a better pilot flame attachment when a non-premixed

pilot flame configuration is used due to its higher reactivity than methane fuel. This is found to have a substantial impact on the pilot nozzle surface temperature, which is governed by the balance between the cooling effect of the pilot air and fuel streams and the heating from the main and the pilot flames. Thus, the H_2-enriched methane/air flame provides high local heating. For this mixture, nozzle surface temperatures are lower than methane/air flames due to the lower stable equivalence ratio. Compared with the partially and fully premixed configuration, the pilot air forms a cooling film above the non-premixed pilot flame nozzle, lowering the local surface temperature. The surface temperature of the fully premixed nozzle is overall higher than partially premixed for both the methane and the hydrogen-enriched/methane fuels. This is due to the higher degree of fuel/air mixing compared to the partially premixed pilot flame, which improves the flame anchoring. The inner channel flows also show a relevant impact on the surface temperature.

- Qualitative analysis of simultaneous OH- and CH_2O-PLIF data highlighted that the flame front tip is pushed upstream in the higher Reynolds number flames due to the higher turbulent flame speed and turbulence intensity. At stable conditions, the flame stabilizes, forming an M-shape flame, and when the pilot flame is used, the structure shifts from unattached to attached M-shape. This is more visible for non-premixed pilot flame configuration and for H_2-enriched mixtures. Furthermore, instantaneous OH layer images are found to be more discontinuous and wrinkled when hydrogen is added to the methane/air mixture. The reactants tend to burn in isolated pockets at close-to-LBO conditions. This can be attributed to the differential diffusion effect due to the mixture's high diffusivity of H_2. A similar effect is visible when pilot flames are used. The results from optical images are quantitatively confirmed by flame surface density and curvature assessments. The wrinkling effect visible when pilot flames are employed can be attributed to the lower main flow stream since the total amount of fuel injected through the pilot and the main flame have been kept constant.

- Results from the mean flow field show that the H_2-enrichment expands the inner recirculation zone. On the other hand, pilot flames led the IRZ to move closer to the combustor axis due to the reduced fuel in the main flow stream. A contraction of the inner recirculation zone is also visible when comparing the close-to-LBO flames with the stable flames. For both methane and hydrogen-enriched flames, it is visible that the OH layer is pushed from the upstream high-speed shear layer in the stable flame conditions to the IRZ at close-to-LBO conditions.

- The NO_x emissions increase with an increase in Reynolds number and equivalence ratio, while they decrease with H_2 dilution due to the ultra-lean operation range. These trends are found to correlate well with flame temperature variations. The partially premixed pilot flames yield slightly lower NO_x emissions levels than the non-premixed ones. This can also be attributed to the local higher local flame temperature in the non-premixed pilot flames. A not-clear correlation was found between CO emissions and the Reynolds number or the pilot flame configurations. However, hydrogen enrichment leads to a significant increase in CO levels. This is likely due to the local extinction of the ultra-lean hydrogen-enriched flames near the lean blow-off limit.

The third part of the thesis (**Paper V**) investigates the effects of CO_2 dilution in a syngas mixture (3% CH_4, 44% CO and 53% H_2) on the flames in the CeCOST Burner using experimental diagnostic techniques. The main findings are:

- The stable operability range (in terms of equivalence ratio) shifts towards a richer mixture as the CO_2 dilution increases due to the chemical and thermal effect of CO_2.
- At constant equivalence ratio, the flame luminescence decreases with an increase in CO_2 dilution. This indicates that the chemical reactions are suppressed by the CO_2 dilution. Furthermore, the OH radicals distribution in the syngas flame without CO_2 dilution appears as continuous but non-homogeneous. This can be attributed to the diffusional-thermal instability due to the high hydrogen concentration in the fuel mixture. At high CO_2 dilution, the syngas flames exhibit quite significantly different flame structures, with combustion taking place in isolated pockets surrounded by unburned fuel/air mixtures. The detected flame significantly differs from flamelet combustion typically found in premixed methane/air flames under similar Karlovitz numbers.
- At constant adiabatic flame temperature, the flow field results show that the mean flow field deviates from the pure syngas mixture when CO_2 is diluted in the mixture. In fact, under these conditions, the inner recirculation zone moves closer to the combustor center axis. This is likely due to the lower mean heat release in the recirculation zone.
- An increase on CO_2 dilution decreases the NO_x emissions. On the other hand, the opposite trend is detected for CO emissions. This trend is different from premixed methane/air flames in the same burner, likely due to the flame-pocket structure detected in syngas flames.

6.2 Future Outlook

Further investigations are needed to provide a more complete and comprehensive understanding of the different topics studied in this thesis. Some suggestions for future work are:

- The effect of thermal expansion on the evolution equation for displacement speed and its decomposed components has been studied at a constant Karlovitz (Ka) number. However, more simulations predicting the impact of Ka are needed for a complete assessment of the displacement speed and related parameters.
- The DNS code used in this thesis can be improved by modifying the governing equations to describe nonunity Lewis number gaseous species. This can allow simulation of the behaviour of fuels like hydrogen.
- Several amounts of pilot mass flow rates routed from the main have been tested, keeping the global equivalence ratio constant. However, seeing if the burner stability limits can benefit from other control strategies can be interesting. For example, the impact of keeping the amount of pilot fuel and air constant can be tested while varying the main flame equivalence ratio.
- The level of hydrogen dilution in methane investigated in this thesis was limited to 50% in volume due to the impossibility of varying the hydrogen content in the mixture during experiments. However, further measures of different hydrogen content in the fuel mixtures are required to have a complete operability map of the burner.
- Extensive experimental data were collected to characterize the hydrogen-enriched flame in the CeCOST burner in the most detailed way. However, due to the limitations in terms of the number of information that can be extracted by experimental analysis, numerical simulation should be performed to gain a more profound knowledge of the resulting flame.
- Experimental observations on the effect of Reynolds number for different syngas mixtures are needed to understand if a higher thermal load can compensate for the thermal and chemical inhibition from CO_2 dilution.
- Existing numerical models need to be developed/improved to predict the fuel pocket flame structure revealed by the syngas mixtures at high CO_2 dilution.

- The differences between 1D numerical predictions and the experimental observations on the emission profiles highlight the importance of the heat transfer process between the liner and the surrounding environment. Therefore, measurements of the liner temperature are needed to improve the accuracy of the existing model.

Appendix A

Numerical Definition of Statistical Tools

The qualification of statistical fluctuations used in Chapter 5 can be made clear through the introduction of a number of qualification measures.
In fully-developed (t_∞) reacting flow system, starting from a point-wise, multi-conditioned probability density function $\mathrm{pdf}(\psi, \phi, |\nabla c|, c; \boldsymbol{x})$ involving two arbitrary quantities, defined here ψ and ϕ, an area-weighted two-quantities joint pdf can be defined as

$$\mathrm{jpdf}_s(\psi, \phi)|_c \equiv \frac{1}{n_s''} \int_0^{+\infty} \iiint_V |\nabla c| \cdot \mathrm{pdf}(\psi, \phi, |\nabla c|, c; \boldsymbol{x}) \, \mathrm{d}\boldsymbol{x} \, \mathrm{d}|\nabla c|. \tag{A.1}$$

Then, an "area-weighted" single-quantity pdf can be defined as,

$$\mathrm{pdf}_s(\psi)|_c \equiv \frac{1}{n_s'} \int_{-\infty}^{+\infty} \mathrm{jpdf}_s(\psi, \phi)|_c \, \mathrm{d}\phi, \tag{A.2}$$

as well as an "un-weighted" one as [172]

$$\mathrm{pdf}_v(\psi)|_c \equiv \frac{1}{n_v'} \iint_{-\infty}^{+\infty} \iiint_V \mathrm{pdf}(\psi, \phi, |\nabla c|, c; \boldsymbol{x}) \, \mathrm{d}\boldsymbol{x} \, \mathrm{d}\phi \, \mathrm{d}|\nabla c|, \tag{A.3}$$

where n_s', n_s'' and n_v' are constants to normalize the corresponding pdfs. Then, a ψ-conditioned surface-average can be introduced as

$$[\phi]_s|_{\psi,c} = \int_{-\infty}^{\infty} \phi \cdot \mathrm{jpdf}_s(\psi, \phi)|_c \, \mathrm{d}\phi / \int_{-\infty}^{\infty} \mathrm{jpdf}_s(\psi, \phi)|_c \, \mathrm{d}\phi, \tag{A.4}$$

which is related to the average over entire isosurface, $\hat{c}$ as

$$\langle \phi \rangle_s|_{\hat{c},t_\infty} = \int_{-\infty}^{+\infty} \mathrm{pdf}_s(\psi)|_{\hat{c}} \cdot [\phi]_s|_{\psi,\hat{c}} \, \mathrm{d}\psi. \tag{A.5}$$

Appendix B

Flame Fronts Data Extraction

B.1 Progress Variable and Flame Surface Density

The spatial location of the reaction zone represents an important parameter when studying the interaction between turbulence an flame. Since the OH intensity is higher in the reaction zone and it decreases in the post-flame zone [72, 173], OH-PLIF images represent a suitable type of data to extract the flame front location. Although a detectable amount of OH radicals is visible in the post-flame zone due to the only slight decrease in OH species, the OH concentration varies with temperature, and it is reasonable to have a sharp temperature gradient between the cold reactants and the hot combustion products [174]. Furthermore, as proven by experiments using techniques like Raman and LIF as well as kinetic modeling [158, 175], the reaction zone is characterized by the OH super equilibrium concentration. Thus, the latter phenomenon, coupled with the aforementioned substantial temperature gradient, results in a strong OH-PLIF signal gradient between reactants and products. Here a brief introduction of the well known flame front edge extraction procedure technique[150, 176–179] is reported.

For each raw OH-PLIF image, the signal-to-noise ratio is increased by removing the background noise first and, then, binning it using a (2x2) window (Figure B.1.a). Subsequently, the resulting image is converted into grayscale (not shown here) and later binarized setting an appropriate threshold. This is found based on the Otsu's method [180], able to minimize the interclass variance of the threshold pixel [150]. Thus, a value of 1 is assigned to regions containing a signal intensity above the aforementioned threshold to represent the burned

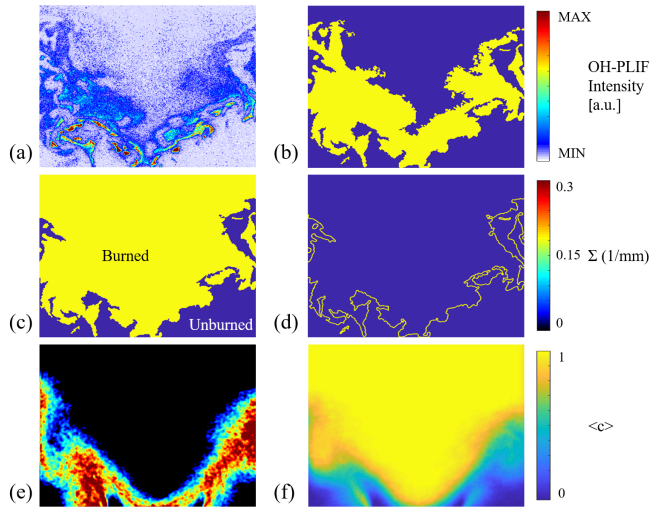

Figure B.1: (a) Background subtracted and binned single shot OH-PLIF; (b) binarized image using Otsu's method; (c) identification of unburned and burned zone; (d) extracted flame front; (e) 2D Flame Surface Density field and (f) 2D ensemble averaged progress variable $\langle c \rangle$.

gas, while a value of 0 for regions containing a signal intensity below that for the unburned gases (Figure B.1.b). As visible in Figure B.1.b, some regions containing a value of 0 are placed in the post-flame zone, right downstream of the reacting front due to the low OH signal intensity there. However, these regions are artificially replaced with ones since they are indeed inside the post-flame zone characterized by low OH signal gradient (Figure B.1.c). Next, the flame front is extracted (Figure B.1.d). The flame front obtained from 500 OH-PLIF snapshots are overlapped to obtain the flame brush [181, 182]. Later, the 2-D flame surface density (Σ) is derived using the Equation B.1 [183, 184] (Figure B.1.e):

$$\Sigma = \lim_{\Delta x \to 0} \frac{\bar{L_f}}{\Delta x^2} \tag{B.1}$$

where $\bar{L_f}$ is the time-averaged pixel length in a Δx^2 = 1.2 x 1.2 mm. Experiments have shown that the size of the pixel box has little influence on the results [183]. Thus, the selection is made based on values found in the literature on a swirl burner operated under similar working conditions [185]. Simultaneously the mean progress variable field is computed using the definition from Kobayashi et al. [186]. Once the binary images are obtained as in Figure B.1.c, the mean progress variable, $\langle c \rangle$, is computed overlapping the 500 instantaneous images (Figure B.1.f) and applying Equation B.2:

$$\langle c \rangle = \frac{1}{N} \sum_{i=1}^{N} c_i(x, y) \tag{B.2}$$

where $c_i(x, y)$ is the progress variable of the i^{th} instantaneous binarized flame at location (x, y).

B.2 Flame Front Curvature Calculation

The curvature of the flame front extracted from the OH-PLIF images can be used to characterize flame wrinkling. The statistics of wrinkling scales can be described using a probability density function (PDF). Similarly to previous experimental works [177, 182, 187, 188], the flame curvature, k, is computed based on the flame front as in Figure B.1.d. This is extracted in the Cartesian r and y coordinates for cross-flow and axial directions, respectively, and it is discretized and reconstructed to eliminate the noise based on a path length parameter (s) denoting the flame front measured from a fixed point of the contour. The curvature is computed using Eq. (B.3) [182]:

$$k = \frac{\dot{r}\ddot{y} - \dot{y}\ddot{r}}{(\dot{r}^2 + \dot{y}^2)^{3/2}} \tag{B.3}$$

where $\dot{r}$, $\ddot{r}$, and $\dot{y}$, $\ddot{y}$ denote the first and second derivative of the cross-flow and axial directions, respectively, with respect to the path length parameter, s. The PDF shown in Section 5 are computed from a set of 500 OH-PLIF images.

References

[1] IEA. World energy outlook 2022. 2022.

[2] BP. bp statistical review of world energy 2022. 2022.

[3] H. Saravanamuttoo, G. Rogers, H. Cohen, and P. Straznicky. *Gas Turbine Theory. 2nd ed.* London: Longman, 1972.

[4] M. Aldén, J. Bood, Z. Li, and M. Richter. Visualization and understanding of combustion processes using spatially and temporally resolved laser diagnostic techniques. *Proceedings of the Combustion Institute*, 33(1):69–97, 2011.

[5] M. S. Mansour, N. Peters, and Y.-C. Chen. Investigation of scalar mixing in the thin reaction zones regime using a simultaneous ch-lif/rayleigh laser technique. *Symposium (International) on Combustion*, 27(1):767–773, 1998.

[6] Z. S. Li, B. Li, Z. W. Sun, X.-S. Bai, and M. Aldén. Turbulence and combustion interaction: High resolution local flame front structure visualization using simultaneous single-shot plif imaging of ch, oh, and ch2o in a piloted premixed jet flame. *Combustion and Flame*, 157(6):1087–1096, 2010.

[7] J. Kiefer, Z. Li, J. Zetterberg, X.-S. Bai, and M. Aldén. Investigation of local flame structures and statistics in partially premixed turbulent jet flames using simultaneous single-shot ch and oh planar laser-induced fluorescence imaging. *Combustion and Flame*, 154(4):802–818, 2008.

[8] J. Sjöholm, J. Rosell, B. Li, M. Richter, Z. Li, X.-S. Bai, and M. Aldén. Simultaneous visualization of oh, ch, ch2o and toluene plif in a methane jet flame with varying degrees of turbulence. *Proceedings of the Combustion Institute*, 34(1):1475–1482, 2013.

[9] B. Zhou, C. Brackmann, Z. Li, M. Aldén, and X.-S. Bai. Simultaneous multi-species and temperature visualization of premixed flames in the distributed reaction zone regime. *Proceedings of the Combustion Institute*, 35(2):1409–1416, 2015.

[10] B. Zhou, C. Brackmann, Q. Li, Z. Wang, P. Petersson, Z. Li, M. Alden, and X.-S. Bai. Distributed reactions in highly turbulent premixed methane/air flames: Part i. flame structure characterization. *Combustion and Flame*, 162(7):2937–2953, 2015.

[11] B. Zhou, C. Brackmann, Z. Wang, Z. Li, M. Richter, M. Aldén, and X.-S. Bai. Thin reaction zone and distributed reaction zone regimes in turbulent premixed methane/air flames: Scalar distributions and correlations. *Combustion and Flame*, 175:220, 2017.

[12] H. G. Im. *Direct Numerical Simulations for Combustion Science: Past, Present, and Future*, pages 99–132. Springer Singapore, Singapore, 2018.

[13] A. J. Aspden, M. S. Day, and J. B. Bell. Turbulence-flame interactions in lean premixed hydrogen: Transition to the distributed burning regime. *Journal of Fluid Mechanics*, 680:287, 2011.

[14] H. Carlsson, R. Yu, and X.-S. Bai. Direct numerical simulation of lean premixed CH 4 /air and H 2 /air flames at high Karlovitz numbers. *International Journal of Hydrogen Energy*, 39(35):20216, 2014.

[15] H. Carlsson, R. Yu, and X.-S. Bai. Flame structure analysis for categorization of lean premixed CH4/air and H2/air flames at high Karlovitz numbers: Direct numerical simulation studies. *Proceedings of the Combustion Institute*, 35(2):1425–1432, 2015.

[16] T. Nilsson, H. Carlsson, R. Yu, and X.-S. Bai. Structures of turbulent premixed flames in the high karlovitz number regime – dns analysis. *Fuel*, 216:627, 2018.

[17] H. Wang, E. R. Hawkes, and J. H. Chen. Turbulence-flame interactions in dns of a laboratory high karlovitz premixed turbulent jet flame. *Physics of Fluids*, 28(9):095107, 2016.

[18] H. Wang, E. R. Hawkes, J. H. Chen, B. Zhou, A. Li, and M. Aldén. Direct numerical simulations of a high karlovitz number laboratory premixed jet flame - an analysis of flame stretch and flame thickening. *Journal of Fluid Mechanism*, 815:511, 2017.

[19] R. Benzi. *Lewis Fry Richardson*, page 187–208. Cambridge University Press, 2011.

[20] O. Reynolds. Iv. on the dynamical theory of incompressible viscous fluids and the determination of the criterion. *Philosophical Transactions of the Royal Society of London. (A.)*, 186:123–164, 1895.

[21] P. Domingo and L. Vervisch. Triple flames and partially premixed combustion in autoignition of non-premixed turbulent mixtures. *Symposium (International) on Combustion*, 26(1):233–240, 1996.

[22] R. W. Bilger, S. B. Pope, K. N. C. Bray, and J. F. Driscoll. Paradigms in turbulent combustion research. *Proceedings of the Combustion Institute*, 30(1):21–42, 2005.

[23] K. J. Nogenmyr, J. Kiefer, Z. S. Li, X.-S. Bai, and M. Aldén. Numerical computations and optical diagnostics of unsteady partially premixed methane/air flames. *Combustion and Flame*, 157(5):915–924, 2010.

[24] M. D. Smoke and V. Giovangigli. *Formulation of the premixed and non premixed test problems*, pages 1–28. Springer Berlin Heidelberg, Berlin, Heidelberg, 1991.

[25] R. Borghi. Turbulent combustion modelling. *Progress in Energy and Combustion Science*, 14(4):245–292, 1988.

[26] K. Seshadri and N. Peters. The inner structure of methaneair flames. *Combustion and Flame*, 81(2):96–118, 1990.

[27] N. Peters. *Turbulent combustion*. Cambridge University Press, 2000.

[28] R. Borghi. *On the Structure and Morphology of Turbulent Premixed Flames*, pages 117–138. Springer US, Boston, MA, 1985.

[29] F.A. Williams. *Combustion Theory. 2nd Edition*, pages 1–28. Benjamin Cummings, California, 1985.

[30] T. Poinsot, D. Veynante, and S. Candel. Quenching processes and premixed turbulent combustion diagrams. *Journal of Fluid Mechanics*, 228: 561–606, 1991.

[31] N. Peters. Laminar flamelet concepts in turbulent combustion. *Symposium (International) on Combustion*, 21(1):1231–1250, 1988. Twenty-First Symposium (International on Combustion).

[32] N. Peters. The turbulent burning velocity for large-scale and small-scale turbulence. *Journal of Fluid Mechanics*, 384:107–132, 1999.

[33] A. M. Steinberg and J. F. Driscoll. Straining and wrinkling processes during turbulence–premixed flame interaction measured using temporally-resolved diagnostics. *Combustion and Flame*, 156(12):2285–2306, 2009.

[34] A. M. Steinberg and J. F. Driscoll. Stretch-rate relationships for turbulent premixed combustion les subgrid models measured using temporally resolved diagnostics. *Combustion and Flame*, 157(7):1422–1435, 2010.

[35] Y.-C. Chen, N. Peters, G. A. Schneemann, N. Wruck, U. Renz, and M. S. Mansour. The detailed flame structure of highly stretched turbulent premixed methane-air flames. *Combustion and Flame*, 107(3):223–IN2, 1996.

[36] J. F. Driscoll. Turbulent premixed combustion: Flamelet structure and its effect on turbulent burning velocities. *Progress in Energy and Combustion Science*, 34(1):91–134, 2008.

[37] H. Pitsch and L. D. De Lageneste. Large-eddy simulation of premixed turbulent combustion using a level-set approach. *Proceedings of the Combustion Institute*, 29(2):2001–2008, 2002.

[38] H. Pitsch. Large-eddy simulation of turbulent combustion. *Annual Review of Fluid Mechanics*, 38(1):453–482, 2006.

[39] T. Poinsot and D. Veynante. *Theoretical and Numerical Combustion*. R.T. Edwards, Philadelphia, PA, 2001.

[40] M. S. Mansour Y.-C. Chen. Investigation of flame broadening in turbulent premixed flames in the thin-reaction-zones regime. *Symposium (International) on Combustion*, 27(1):811–818, 1998. Twenty-Seventh Sysposium (International) on Combustion Volume One.

[41] R. Sankaran, E. R. Hawkes, J. H. Chen, T. Lu, and C. K. Law. Structure of a spatially developing turbulent lean methane–air bunsen flame. *Proceedings of the Combustion Institute*, 31(1):1291–1298, 2007.

[42] L.P.H. de Goey, T. Plessing, R.T.E. Hermanns, and N. Peters. Analysis of the flame thickness of turbulent flamelets in the thin reaction zones regime. *Proceedings of the Combustion Institute*, 30(1):859–866, 2005.

[43] J. Rosell, X.-S. Bai, J. Sjoholm, B. Zhou, Z. Li, Z. Wang, P. Pettersson, Z. Li, M. Richter, and M. Alden. Multi-species plif study of the structures of turbulent premixed methane/air jet flames in the flamelet and thin-reaction zones regimes. *Combustion and Flame*, 182:324–338, 2017.

[44] J. Temme, T. M. Wabel, A. W. Skiba, and J. F. Driscoll. Measurements of premixed turbulent combustion regimes of high reynolds number flames. In *53rd AIAA Aerospace Sciences Meeting*, page 0168, 2015.

[45] T. M. Wabel, A. W. Skiba, J. E. Temme, and J. F. Driscoll. Measurements to determine the regimes of premixed flames in extreme turbulence. *Proceedings of the Combustion Institute*, 36(2):1809–1816, 2017.

[46] J. F. Driscoll, J. H. Chen, A. W. Skiba, C. D. Carter, E. R. Hawkes, and H. Wang. Premixed flames subjected to extreme turbulence: Some questions and recent answers. *Progress in Energy and Combustion Science*, 76:100802, 2020.

[47] Q. Fan, X. Liu, L. Xu, A. A. Subash, C. Brackmann, M. Aldén, X.-S. Bai, and Z. Li. Flame structure and burning velocity of ammonia/air turbulent premixed flames at high karlovitz number conditions. *Combustion and Flame*, 238:111943, 2022.

[48] Q. Fan, X. Liu, X. Cai, C. Brackmann, M. Alden, X.-S. Bai, and Z. Li. Structure and scalar correlation of ammonia/air turbulent premixed flames in the distributed reaction zone regime. *Combustion and Flame*, 241:112090, 2022.

[49] L. Xu, Q. Fan, X. Liu, X. Cai, A. A. Subash, C. Brackmann, Z. Li, M. Aldén, and X.-S. Bai. Flame/turbulence interaction in ammonia/air premixed flames at high karlovitz numbers. *Proceedings of the Combustion Institute*, 2022.

[50] T. Nilsson. *Direct numerical simulation of turbulent premixed flames at high Karlovitz numbers: structure and modelling*. PhD thesis, 2019.

[51] R. W. Schefer, D. M. Wicksall, and A. K. Agrawal. Combustion of hydrogen-enriched methane in a lean premixed swirl-stabilized burner. *Proceedings of the Combustion Institute*, 29(1):843–851, 2002. Proceedings of the Combustion Institute.

[52] R. W. Schefer, D. M. Wicksall, and A. K. Agrawal. Combustion of hydrogen-enriched methane in a lean premixed swirl-stabilized burner. *Proceedings of the combustion institute*, 29(1):843–851, 2002.

[53] R. W. Schefer. Combustion of hydrogen-enriched methane in a lean premixed swirl burner. In *Proceedings of the 2001 US DOE hydrogen program review*, 2001.

[54] D. M. Wicksall, A. K. Agrawal, R. W. Schefer, and J. O. Keller. Fuel composition effects on the velocity field in a lean premixed swirl-stabilized combustor. In *Turbo Expo: Power for Land, Sea, and Air*, volume 36851, pages 539–548, 2003.

[55] S. Taamallah, K. Vogiatzaki, F. M. Alzahrani, E. M. A. Mokheimer, M. A. Habib, and A. F. Ghoniem. Fuel flexibility, stability and emissions in premixed hydrogen-rich gas turbine combustion: Technology, fundamentals, and numerical simulations. *Applied Energy*, 154:1020–1047, 2015. ISSN 0306-2619.

[56] W. Zhang, J. Wang, R. Mao, W. Lin, B. Lin, Y. Wu, M. Zhang, and Z. Huang. Experimental study of compact swirl flames with lean premixed ch4/h2/air mixtures at stable and near blow-off conditions. *Experimental Thermal and Fluid Science*, 122:110294, 2021. ISSN 0894-1777.

[57] X. Liu, M. Bertsch, A. A. Subash, S. Yu, R.-Z. Szasz, Z. Li, P. Petersson, X.-S. Bai, M. Aldén, and D. Lörstad. Investigation of turbulent premixed methane/air and hydrogen-enriched methane/air flames in a laboratory-scale gas turbine model combustor. *International Journal of Hydrogen Energy*, 46(24):13377–13388, 2021.

[58] M. Abdulsada, N. Syred, A. Griffiths, and P. Bowen. Effect of swirl number and fuel type upon the flashback in swirl combustors. 01 2011. ISBN 978-1-60086-950-1.

[59] P. Chiesa, G. Lozza, and L. Mazzocchi. Using hydrogen as gas turbine fuel. *Journal of Engineering for Gas Turbines and Power*, 127(1):73–80, 2005.

[60] T. Lieuwen, V. McDonell, D. Santavicca, and T. Sattelmayer. Burner development and operability issues associated with steady flowing syngas fired combustors. *Combustion Science and Technology*, 180(6):1169–1192, 2008.

[61] N. A. Samiran, J.-H. Ng, M. Nazri, M. Jaafar, A. Valera-Medina, and C. T. Chong. H2-rich syngas strategy to reduce nox and co emissions and improve stability limits under premixed swirl combustion mode. *International Journal of Hydrogen Energy*, 41(42):19243–19255, 2016. ISSN 0360-3199.

[62] N. A. Samiran, M. N. M. Jaafar, J.-H. Ng, S. S. Lam, and C. T. Chong. Progress in biomass gasification technique – with focus on malaysian palm

biomass for syngas production. *Renewable and Sustainable Energy Reviews*, 62:1047–1062, 2016. ISSN 1364-0321.

[63] C. Dong, Q. Zhou, Q. Zhao, Y. Zhang, T. Xu, and S. Hui. Experimental study on the laminar flame speed of hydrogen/carbon monoxide/air mixtures. *Fuel*, 88(10):1858–1863, 2009. ISSN 0016-2361.

[64] J. Natarajan, T. Lieuwen, and J. Seitzman. Laminar flame speeds of h2/co mixtures: Effect of co2 dilution, preheat temperature, and pressure. *Combustion and Flame*, 151(1):104–119, 2007. ISSN 0010-2180.

[65] C. Liu, B. Yan, G. Chen, and X.-S. Bai. Structures and burning velocity of biomass derived gas flames. *International Journal of Hydrogen Energy*, 35(2):542–555, 2010. ISSN 0360-3199.

[66] B. Yan, Y. Wu, C. Liu, J. F. Yu, B. Li, Z. Li, G. Chen, X.-S. Bai, M. Alden, and A. A. Konnov. Experimental and modeling study of laminar burning velocity of biomass derived gases/air mixtures. *International Journal of Hydrogen Energy*, 36(5):3769–3777, 2011. ISSN 0360-3199.

[67] L. D. Thi, Y. Zhang, and Z. Huang. Shock tube study on ignition delay of multi-component syngas mixtures – effect of equivalence ratio. *International Journal of Hydrogen Energy*, 39(11):6034–6043, 2014. ISSN 0360-3199.

[68] H. C. Lee, L. Y. Jiang, and A. A. Mohamad. A review on the laminar flame speed and ignition delay time of syngas mixtures. *International Journal of Hydrogen Energy*, 39(2):1105–1121, 2014. ISSN 0360-3199.

[69] J. S. Kim, J. Park, O. B. Kwon, D. S. Bae, J. H. Yun, and S. I. Keel. A study on flame structure and extinction in downstream interaction between lean premixed ch4–air and (50% h2+50% co) syngas–air flames. *International Journal of Hydrogen Energy*, 36(9):5717–5728, 2011. ISSN 0360-3199.

[70] N. A. Samiran, J.-H. Ng, M. Nazri, M. Jaafar, A. Valera-Medina, and C. T. Chong. Swirl stability and emission characteristics of co-enriched syngas/air flame in a premixed swirl burner. *Process Safety and Environmental Protection*, 112:315–326, 2017. ISSN 0957-5820.

[71] A. N. Lipatnikov and J. Chomiak. Molecular transport effects on turbulent flame propagation and structure. *Progress in Energy and Combustion Science*, 31(1):1–73, 2005. ISSN 0360-1285.

[72] S. Li, X. Zhang, D. Zhong, F. Weng, S. Li, and M. Zhu. Effects of inert dilution on the lean blowout characteristics of syngas flames. *International Journal of Hydrogen Energy*, 41(21):9075–9086, 2016. ISSN 0360-3199.

[73] P. Strakey, N. Weiland, and G. Richards. Combustion strategies for syngas and high-hydrogen fuel. *The Gas Turbine Handbook*, 2006.

[74] D. E. Giles, S. Som, and S. K. Aggarwal. Nox emission characteristics of counterflow syngas diffusion flames with airstream dilution. *Fuel*, 85(12): 1729–1742, 2006. ISSN 0016-2361.

[75] S.-G. Kim, J. Park, and S.-I. Keel. Thermal and chemical contributions of added h2o and co2 to major flame structures and no emission characteristics in h2/n2 laminar diffusion flame. *International Journal of Energy Research*, 26(12):1073–1086, 2002.

[76] M. Arai. Flue gas recirculation for low nox combustion system, 2000.

[77] P. Røkke and J. Hustad. Exhaust gas recirculation in gas turbines for reduction of co2 emissions; combustion testing with focus on stability and emissions. *International Journal of thermodynamics*, 8(4):167–173, 2005.

[78] T. C. Williams, C. R. Shaddix, and R. W. Schefer. Effect of syngas composition and co2-diluted oxygen on performance of a premixed swirl-stabilized combustor. *Combustion Science and Technology*, 180(1):64–88, 2007.

[79] P. Sayad, A. Schonborn, and J. Klingmann. Experimental investigations of the lean blowout limit of different syngas mixtures in an atmospheric, premixed, variable-swirl burner. *Energy & fuels*, 27(5):2783–2793, 2013.

[80] S. Daniele, P. Jansohn, and K. Boulouchos. Lean premixed combustion of undiluted syngas at gas turbine relevant conditions: Nox emissions and lean operational limits. 43130:137–144, 2008.

[81] F. A. Williams. *Combustion Theory, 2nd Ed.* Menlo Park: Benjamin-Cummings Publishing Co., 1985.

[82] S. M. Candel and T. J. Poinsot. Flame Stretch and the Balance Equation for the Flame Area. *Combustion, Science and Technology*, 70(1-3):1, 1990.

[83] T. Echekki and J. H. Chen. Unsteady strain rate and curvature effects in turbulent premixed methane-air flames. *Combustion and Flame*, 106: 184–202, 1996.

[84] N. Chakraborty. Comparison of displacement speed statistics of turbulent premixed flames in the regimes representing combustion in corrugated flamelets and thin reaction zones. *Physics of Fluids*, 19(10):105109, 2007.

[85] R. Sankaran, E. R. Hawkes, J. H. Chen, T. Lu, and C. K. Law. Structure of a spatially developing turbulent lean methane-air bunsen flame. *Proceeding of the Combustion Institute*, 31 I(1):1291, 2007.

[86] H. Wang, E. R Hawkes, and J. H. Chen. A direct numerical simulation study of flame structure and stabilization of an experimental high ka ch4/air premixed jet flame. *Combustion and Flame*, 180:110–123, 2017.

[87] S. Luca, A. Attili, E. L. Schiavo, F. Creta, and F. Bisetti. On the statistics of flame stretch in turbulent premixed jet flames in the thin reaction zone regime at varying reynolds number. *Proceedings of the Combustion Institute*, 37:2451–2459, 2019.

[88] C. Dopazo, J. Martín, and J. Hierro. Local geometry of isoscalar surfaces. *Physical Review E*, 76(5):056316, 2007.

[89] L. Cifuentes, C. Dopazo, J. Martin, and C. Jimenez. Local flow topologies and scalar structures in a turbulent premixed flame. *Physics of Fluids*, 26 (6):065108, 2014.

[90] N. Chakraborty and R. S. Cant. Unsteady effects of strain rate and curvature on turbulen premixed flames in an inflow–outflow configuration. *Combustion and Flame*, 137(1-2):129–147, 2004.

[91] E. R. Hawkes and J. H. Chen. Comparison of direct numerical simulation of lean premixed methane-air flames with strained laminar flame calculations. *Combustion and Flame*, 144:112–125, 2006.

[92] H. S. Kim and H. Pitsch. Scalar gradient and small-scale structure in turbulent premixed combustion. *Physics of Fluids*, 19(11):115104, 2007.

[93] S. Chaudhuri. Life of flame particles embedded in premixed flames interacting with near isotropic turbulence. *Proceedings of the Combustion Institute*, 35:1305–1312, 2015.

[94] D. Cecere, E. Giacomazzi, N. M. Arcidiacono, and F. R. Picchia. Direct numerical simulation of high pressure turbulent lean premixed ch4/h2-air slot flames. *International Journal of Hydrogen Energy*, 43:5184–5198, 2018.

[95] G. H. Markstein. *Nonsteady Flame Propagation*. Pergamon Press, 1964.

[96] M. Matalon and B. J. Matkowsky. Flames as gas dynamic discontinuities. *Journal of Fluid Mechanics*, 124:239–60, 1982.

[97] P. Pelcé and P. Clavin. Influence of hydrodynamics and diffusion upon the stability limits of laminar premixed flames. *Journal of Fluid Mechanics*, 124:219–237, 1982.

[98] A. G. Class, B. J. Matkowsky, and A. Y. Klimenko. A unified model of flames as gasdynamic discontinuities. *Journal of Fluid Mechanics*, 491: 11–49, 2003.

[99] A. P. Kelley, J. K. Bechtold, and C. K. Law. Premixed flame propagation in a confining vessel with weak pressure rise. *Journal of Fluid Mechanics*, 691:26–51, 2012.

[100] G. K. Giannakopoulos, A. Gatzoulis, C. E. Frouzakis, M. Matalon, and A. G. Tomboulides. Consistent definitions of "flame displacement speed" and "markstein length" for premixed flame propagation. *Combustion and Flame*, 162:1249, 2015.

[101] R. Yu, T. Nilsson, G. Brethouwer, N. Chakraborty, and A. Lipatnikov. Assessment of an evolution equation for the displacement speed of a constant-density reactive scalar field. *Flow, Turbulence and Combustion*, pages 1–20, 2020.

[102] R. Yu, T. Nillson, F. Christer, and A. N. Lipatnikov. Evolution equations for the decomposed components of displacement speed in a reactive scalar field. *Journal of Fluid Mechanics*, 911:A38, 2021.

[103] J. H. Chen and H. G. Im. Correlation of flame speed with stretch in turbulent premixed methane-air flames. In *Symposium (International) on Combustion*, volume 27, pages 819–826, 1998.

[104] A. A. Subash, R. Collin, M. Aldén, A. Kundu, and J. Klingmann. Laser-based investigation on a dry low emission industrial prototype burner at atmospheric pressure conditions. In *Turbo Expo: Power for Land, Sea, and Air*, volume 49767. American Society of Mechanical Engineers, 2016.

[105] P. Albrecht, S. Bade, C. Paschereit, and E. Gutmark. *Avoidance Strategy for NOx Emissions and Flame Instabilities in a Swirl-Stabilized Combustor.*

[106] D. Page, B. Shaffer, and V. McDonell. Establishing Operating Limits in a Commercial Lean Premixed Combustor Operating on Synthesis Gas Pertaining to Flashback and Blowout. Volume 1: Aircraft Engine; Ceramics;

Coal, Biomass and Alternative Fuels; Controls, Diagnostics and Instrumentation:647–656, 06 2012.

[107] B. A. Imteyaz, M. A. Nemitallah, A. A. Abdelhafez, and M. A. Habib. Combustion behavior and stability map of hydrogen-enriched oxy-methane premixed flames in a model gas turbine combustor. *International Journal of Hydrogen Energy*, 43(34):16652–16666, 2018.

[108] V. Papapostolou, N. Chakraborty, M. Klein, and H. G. Im. Effects of reaction progress variable definition on the flame surface density transport statistics and closure for different combustion regimes. *Combustion Science and Technology*, 191(8):1276–1293, 2019.

[109] T. Elperin, N. Kleeorin, M. Liberman, A. N. Lipatnikov, I. Rogachevskii, and R. Yu. Turbulent diffusion of chemically reacting flows: Theory and numerical simulations. *Phys. Rev. E*, 96:053111, Nov 2017.

[110] M. Day, I. Shepherd, J. Bell, J. Grcar, and M. Lijewski. Displacement speeds in turbulent premixed flame simualtions. *Computational Combustion 2007, ECCOMAS Thematic Conference, 18-20 July 2007, Delft, The Netherlands*, Jul .

[111] R. Yu and A. N. Lipatnikov. Surface-averaged quantities in turbulent reacting flows and relevant evolution equations. *Physics Review E*, 100: 013107, Jul 2019.

[112] D. Veynante and L. Vervisch. Turbulent combustion modeling. *Progressing in Energy and Combustion Science*, 28(3):193, 2002.

[113] N. Peters, P. Terhoeven, J. H. Chen, and T. Echekki. Statistics of flame displacement speeds from computations of 2-d unsteady methane-air flames. In *Proceeding in the Combustion Institute*, volume 27, pages 833–839, 1998.

[114] T. Echekki and J. H. Chen. Analysis of the contribution of curvature to premixed flame propagation. *Combustion and Flame*, 118:308–311, 1999.

[115] M. Klein, D. Alwazzan, and N. Chakraborty. A direct numerical simulation analysis of pressure variation in turbulent premixed bunsen burner flames-part 1: Scalar gradient and strain rate statistics. *Computers & Fluids*, 173:178–188, 2018.

[116] M. Klein, D. Alwazzan, and D. Chakraborty. A direct numerical simulation analysis of pressure variation in turbulent premixed bunsen burner

flames-part 2: Surface density function transport statistics. *Computers & Fluids*, 173:147–156, 2018.

[117] R. Yu and A. N. Lipatnikov. A dns study of sensitivity of scaling exponents for premixed turbulent consumption velocity to transient effects. *Flow, Turbulence and Combustion*, 102(3):679–698, 2019.

[118] S. B. Pope. The evolution of surfaces in turbulence. *International Journal of Engineering Science*, 26(5):445, 1988.

[119] H. L. Dave and S. Chaudhuri. Evolution of local flame displacement speeds in turbulence. *Journal of Fluid Mechanics*, 884:A46, 2020.

[120] R. Yu, J. F. Yu, and X.-S. Bai. An improved high-order scheme for DNS of low Mach number turbulent reacting flows based on stiff chemistry solver. *Journal of Computational Physics*, 231(16):5504, 2012.

[121] G. S. Jiang and C. W. Shu. Efficient implementation of weighted eno schemes. *Journal of Computational Physics*, 126(1):202, 1996.

[122] R. Yu and X.-S. Bai. A semi-implicit scheme for large Eddy simulation of piston engine flow and combustion. *International Journal of Numerical Methods in Fluids*, 71(1):13, 2013.

[123] T. S. Lundgren. Linearly forces isotropic turbulence. *Center for Turbulence Research - Annual Research Briefs 2003*, 2003.

[124] C. Rosales and C. Meneveau. Linear forcing in numerical simulations of isotropic turbulence: Physical space implementations and convergence properties. *Physics of Fluids*, 17(9):095106, 2005.

[125] V. Eswaran and S. B. Pope. An examination of forcing in direct numerical simulations of turbulence. *Computers Fluids*, 16(3):257–278, 1988.

[126] A. G. Lamorgese, D. A. Caughey, and S. B. Pope. Direct numerical simulation of homogeneous turbulence with hyperviscosity. *Physics of Fluids*, 17(1):015106, 2005.

[127] R. Yu, X.-S. Bai, and V. Bychkov. Fractal flame structure due to the hydrodynamic darrieus-landau instability. *Physics Review E*, 92(6):063028, 2015.

[128] J. Jeong and F. Hussain. On the identification of a vortex. *Journal of Fluid Mechanics*, 285:69–94, 1995.

[129] X. Liu. *Experimental studies of turbulent flames at gas turbine relevant burners and operating conditions*. PhD thesis, Lund University, 03 2021.

[130] R. K. Hanson, J. M. Seitzman, and P. H. Paul. Planar laser-fluorescence imaging of combustion gases. *Applied Physics B*, 50:441–454, 06 1990.

[131] Z. S. Li, B. Li, Z. W. Sun, X.-S. Bai, and M. Aldén. Turbulence and combustion interaction: High resolution local flame front structure visualization using simultaneous single-shot plif imaging of ch, oh, and ch2o in a piloted premixed jet flame. *Combustion and Flame*, 157(6):1087–1096, 2010.

[132] K. Kohse-Höinghaus. Laser techniques for the quantitative detection of reactive intermediates in combustion systems. *Progress in Energy and Combustion Science*, 20(3):203–279, 1994. ISSN 0360-1285.

[133] J. W. Daily. Laser induced fluorescence spectroscopy in flames. *Progress in Energy and Combustion Science*, 23(2):133–199, 1997.

[134] T. Metz, X.-S. Bai, F. Ossler, and M Aldén. Fluorescence lifetimes of formaldehyde (h2co) in the a1a2→x1a1 band system at elevated temperatures and pressures. *Spectrochimica Acta Part A: Molecular and Biomolecular Spectroscopy*, 60(5):1043–1053, 2004. ISSN 1386-1425.

[135] K. N. Gabet, R. A. Patton, N. Jiang, W. R. Lempert, and J. A. Sutton. High-speed ch2o plif imaging in turbulent flames using a pulse-burst laser system. *Applied Physics B*, 106(3):569–575, 2004. ISSN 1432-0649.

[136] P. A. Libby and F. A. Williams. Turbulent flows involving chemical reactions. *Annual Review of Fluid Mechanics*, 8(1):351–376, 1976.

[137] Measurement principle of the particle image velocimetry (piv). URL `https://www.optolution.com/en/measuring-principles/piv-principle/`.

[138] M. Raffel, C. J. Kähler, C. E. Willert, S. T. Wereley, Scarano F., and J. Kompenhans. *Particle Image Velocimetry: A Practical Guide*. Springer Science+Business Media, 3rd edition, 2018. ISBN 978-3-319-68851-0.

[139] J. Ballester and T. García-Armingol. Diagnostic techniques for the monitoring and control of practical flames. *Progress in Energy and Combustion Science*, 36(4):375–411, 2010. ISSN 0360-1285.

[140] M. Lauer and T. Sattelmayer. On the Adequacy of Chemiluminescence as a Measure for Heat Release in Turbulent Flames With Mixture Gradients. *Journal of Engineering for Gas Turbines and Power*, 132(6), 03 2010.

[141] Psp4000-h, 115 v. URL https://www.mc-techgroup.com/en/products-special-systems/gas-sampling/gas-sample-probes/40s1000a.

[142] N. Syred and J. M. Beér. Combustion in swirling flows: A review. *Combustion and Flame*, 23(2):143–201, 1974.

[143] N. Syred. A review of oscillation mechanisms and the role of the precessing vortex core (pvc) in swirl combustion systems. *Progress in Energy and Combustion Science*, 32(2):93–161, 2006.

[144] A. K. Gupta, D. G. Lilley, and N. Syred. *Swirl flows*. Abacus Press, Tunbridge Wells, England, 1984.

[145] N. Syred. *The damping of precessing vortex cores by combustion in swirl*. Astronautica Acta, 1972.

[146] A. Valera-Medina, N. Syred, and A. Griffiths. *Characterisation of Large Coherent Structures in a Swirl Burner under Combustion Conditions*.

[147] H. J. Sheen, W. J. Chen, S. Y. Jeng, and T. L. Huang. Correlation of swirl number for a radial-type swirl generator. *Experimental Thermal and Fluid Science*, 12(4):444–451, 1996.

[148] K. S. Kedia and A. F. Ghoniem. The blow-off mechanism of a bluff-body stabilized laminar premixed flame. *Combustion and Flame*, 162(4):1304–1315, 2015.

[149] S. Menon. CO Emission and Combustion Dynamics Near Lean-Blowout in Gas Turbine Engines. Volume 1: Turbo Expo 2004:153–160, 06 2004.

[150] Q. Zhang, D. R. Noble, and T. Lieuwen. Characterization of Fuel Composition Effects in H2COCH4 Mixtures Upon Lean Blowout. *Journal of Engineering for Gas Turbines and Power*, 129(3):688–694, 12 2006.

[151] D. G. Pugh, P. J. Bowen, R. Marsh, A. P. Crayford, J. Runyon, S. Morris, A. Valera-Medina, and A. Giles. Dissociative influence of h2o vapour/spray on lean blowoff and nox reduction for heavily carbonaceous syngas swirling flames. *Combustion and Flame*, 177:37–48, 2017.

[152] A. Amato, B. Hudak, P. D'Carlo, D. Noble, D. Scarborough, J. Seitzman, and T. Lieuwen. Methane Oxycombustion for Low CO2 Cycles: Blowoff Measurements and Analysis. *Journal of Engineering for Gas Turbines and Power*, 133(6), 02 2011.

[153] A. A. Subash, R. Collin, M. Aldén, A. Kundu, and J. Klingmann. Experimental investigation of the influence of burner geometry on flame characteristics at a dry low emission industrial prototype burner at atmospheric pressure conditions. In *Turbo Expo: Power for Land, Sea, and Air*, volume 50848. American Society of Mechanical Engineers, 2017.

[154] O. Lucca-Negro and T. O'Doherty. Vortex breakdown: a review. *Progress in Energy and Combustion Science*, 27(4):431–481, 2001. ISSN 0360-1285.

[155] S. L. Plee and A. M. Mellor. Review of flashback reported in prevaporizing/premixing combustors. *Combustion and Flame*, 32:193–203, 1978.

[156] F. Kiesewetter, M. Konle, and T. Sattelmayer. Analysis of Combustion Induced Vortex Breakdown Driven Flame Flashback in a Premix Burner With Cylindrical Mixing Zone. *Journal of Engineering for Gas Turbines and Power*, 129(4):929–936, 04 2007.

[157] P. Gokulakrishnan and M. S. Klassen. *NOx and CO Formation and Control*, page 175–208. Cambridge Aerospace Series. Cambridge University Press, 2013.

[158] M. C. Drake and R. J. Blint. Relative importance of nitric oxide formation mechanisms in laminar opposed-flow diffusion flames. *Combustion and Flame*, 83(1):185–203, 1991.

[159] A. A. Konnov, G. Colson, and J. De Ruyck. The new route forming no via nnh. *Combustion and Flame*, 121(3):548–550, 2000.

[160] E. Hodzic. *Analysis of flow dynamics and flame stabilization in gas turbine related combustors*. PhD thesis, Lund University, 11 2016.

[161] E. Hodzic, S. Yu, A. A. Subash, X. Liu, X. Liu, R.-Z. Szasz, X.-S. Bai, Z. Li, and M. Alden. Numerical and experimental investigation of the cecost swirl burner. *ASME Turbo Expo 2018: Turbomachinery Technical Conference and Exposition*, 2018.

[162] M. Bertsch. *Numerical and experimental investigation of a gasturbine model combustor with axial swirler*. Lund University, 2021.

[163] G. Darrieus. Propagation d'un front de flamme. *Unpublished work presented at La Technique Moderne*, 1938.

[164] L. Landau. On the theory of slow combustion. In *Dynamics of Curved Fronts*, page 403. Academic Press, 1988.

[165] M. Emadi, D. Karkow, T. Salameh, A. Gohil, and A. Ratner. Flame structure changes resulting from hydrogen-enrichment and pressurization for low-swirl premixed methane–air flames. *International Journal of Hydrogen Energy*, 37(13):10397–10404, 2012.

[166] D. G. Goodwin, H. K. Moffat, I. Schoegl, R. L. Speth, and B. W. Weber. Cantera: An object-oriented software toolkit for chemical kinetics, thermodynamics, and transport processes, 2022.

[167] G. P. Smith, D. M. Golden, M. Frenklach, N. W. Moriarty, B. Eiteneer, M. Goldenberg, C. T. Bowman, R. K. Hanson, S. Song, W. C. Gardiner Jr., V. V. Lissianski, and Z. Qin. http://www.me.berkeley.edu/gri_mech/.

[168] H. Feuk. *Lifetime Surface Phosphor Thermometry - Technique Developments, Sources of Error, and Applications*. PhD thesis, Faculty of Engineering, LTH, March 2023.

[169] S. M. Walton, X. He, B. T. Zigler, and M. S. Wooldridge. An experimental investigation of the ignition properties of hydrogen and carbon monoxide mixtures for syngas turbine applications. *Proceedings of the Combustion Institute*, 31(2):3147–3154, 2007.

[170] J. Park, J. S. Kim, Chung J. H., J. H. Yun, and S. I. Keel. Chemical effects of added co2 on the extinction characteristics of h2/co/co2 syngas diffusion flames. *International Journal of Hydrogen Energy*, 34(20):8756–8762, 2009.

[171] G. I. Barenblatt, Y. B. Zeldovich, and A. G. Istratov. On diffusional thermal stability of a laminar flame. *Journal of Applied Mechanics and Technical Physics*, 4:21, 1962.

[172] R. Yu and A. N. Lipatnikov. Statistics conditioned to isoscalar surfaces in highly turbulent premixed reacting systems. *Computers and Fluids*, 187: 62–82, 2019.

[173] J. H. Bechtel and R. E. Teets. Hydroxyl and its concentration profile in methane–air flames. *Applied Optics*, 18(24):4138–4144, Dec 1979.

[174] R. Sadanandan, M. Stöhr, and W. Meier. Simultaneous oh-plif and piv measurements in a gas turbine model combustor. *Applied Physics B*, (3), 2008.

[175] R. S. Barlow, R. W. Dibble, J.-Y. Chen, and R. P. Lucht. Effect of damköhler number on superequilibrium OH concentration in turbulent

nonpremixed jet flames. *Combustion and Flame*, 82(3):235–251, 1990. ISSN 0010-2180.

[176] I. Boxx, C. Slabaugh, P. Kutne, R. P. Lucht, and W. Meier. 3kHz PIV/OH-PLIF measurements in a gas turbine combustor at elevated pressure. *Proceedings of the Combustion Institute*, 35(3):3793–3802, 2015.

[177] R. Mao, J. Wang, W. Zhang, Z. An, W. Lin, M. Zhang, and Z. Huang. Effect of high hydrogen enrichment on the outer-shear-layer flame of confined lean premixed CH4/H2/air swirl flames. *International Journal of Hydrogen Energy*, 46(34):17969–17981, 2021.

[178] D. Han, A. Satija, J. P. Gore, and R. P. Lucht. Experimental study of CO2 diluted, piloted, turbulent CH4/air premixed flames using high-repetition-rate OH PLIF. *Combustion and Flame*, 193:145–156, 2018. ISSN 0010-2180.

[179] L. Gao, X. Yu, J. Peng, Y. Tian, Z. Cao, F. Zhong, G. Wu, and M. Han. Flame characteristics of a cavity-based scramjet combustor using OH-PLIF and feature extraction. *International Journal of Hydrogen Energy*, 47(47):20662–20675, 2022. ISSN 0360-3199.

[180] N. Otsu. A threshold selection method from gray-level histograms. *IEEE Transactions on Systems, Man, and Cybernetics*, 9(1):62–66, 1979.

[181] W. Zhang, J. Wang, Q. Yu, W. Jin, M. Zhang, and Z. Huang. Investigation of the fuel effects on burning velocity and flame structure of turbulent premixed flames based on leading points concept. *Combustion Science and Technology*, 190(8):1354–1376, 2018.

[182] M. Zhang, J. Wang, Y. Xie, Z. Wei, W. Jin, Z. Huang, and H. Kobayashi. Measurement on instantaneous flame front structure of turbulent premixed CH4/H2/air flames. *Experimental Thermal and Fluid Science*, 52:288–296, 2014. ISSN 0894-1777.

[183] S. A. Filatyev, J. F. Driscoll, C. D. Carter, and J. M. Donbar. Measured properties of turbulent premixed flames for model assessment, including burning velocities, stretch rates, and surface densities. *Combustion and Flame*, 141(1):1–21, 2005. ISSN 0010-2180.

[184] J. Wang, S. Guo, W. Zhang, M. Zhang, and Z. Huang. Effect of hydrogen ratio on turbulent flame structure of oxyfuel syngas at high pressure up to 1.0 mpa. *International Journal of Hydrogen Energy*, 44(21):11185–11193, 2019. ISSN 0360-3199.

[185] J. Zhang and A. Ratner. Experimental study on the excitation of thermoacoustic instability of hydrogen-methane/air premixed flames under atmospheric and elevated pressure conditions. *International Journal of Hydrogen Energy*, 44(39):21324–21335, 2019. ISSN 0360-3199.

[186] H. Kobayashi, K. Seyama, H. Hagiwara, and Y. Ogami. Burning velocity correlation of methane/air turbulent premixed flames at high pressure and high temperature. *Proceedings of the Combustion Institute*, 30(1):827–834, 2005. ISSN 1540-7489.

[187] M. Zhang, J. Wang, J. Wu, Z. Wei, Z. Huang, and K. Hideaki. Flame front structure of turbulent premixed flames of syngas oxyfuel mixtures. *International Journal of Hydrogen Energy*, 39(10):5176–5185, 2014. ISSN 0360-3199.

[188] W. Zhang, J Wang, W. Lin, S. Guo, M. Zhang, G. Li, J. Ye, and Z. Huang. Measurements on flame structure of bluff body and swirl stabilized premixed flames close to blow-off. *Experimental Thermal and Fluid Science*, 104:15–25, 2019. ISSN 0894-1777.

Scientific publications

Author contributions

Paper I: Displacement Speed Analysis of Surface Propagation in Moderately Turbulent Premixed Reacting Waves

Physics of Fluids 33, 035109 (2021)
https://doi.org/10.1063/5.0039023

Francesco Pignatelli, Rixin Yu, Xue-Song Bai, Karl-Johan Nogenmyr

The numerical simulations were done by the candidate based on an in-house DNS code. The candidate implemented the post-processing diagnostic equations in the in-house DNS code and participated in the data analysis and in the writing process with the advice of the co-authors.

Paper II: Pilot Impact on Turbulent Premixed Methane/Air and Hydrogen-Enriched Methane/Air Flames in a Laboratory-Scale Gas Turbine Model Combustor

International Journal of Hydrogen Energy 47, 60 (2022)
https://doi.org/10.1016/j.ijhydene.2022.05.282

Francesco Pignatelli, Haisol Kim, Xin Liu, Arman Ahamed Subash, Robert Zoltan Szasz, Xue-Song Bai, Christian Brackmann, Marcus Aldén, Daniel Lörstad

The candidate designed the experimental case and rig operability conditions, and participated in the experimental campaign, and performed the data analysis. The candidate wrote the first version of the manuscript and revised the manuscript with the advice of the co-authors.

Paper III: Impact of Pilot Flame and Hydrogen Enrichment on Turbulent Methane/Hydrogen/Air Swirling Premixed Flames in a Model Gas Turbine Combustor

Manuscript to be submitted to Fuel

Francesco Pignatelli, David Sanned, Saeed Derafshzan, Robert Zoltan Szasz, Xue-Song Bai, Mattias Richter, Daniel Lörstad, Per Petersson, Arman Ahamed Subash

The candidate designed the experiments, led the experimental campaign, performed the experiments and the data analysis, and wrote the manuscript with the advice of the co-authors.

Paper IV: Impact of Methane and Hydrogen-Enriched Methane Pilot Injection on the Surface Temperature of a Scaled-Down Burner Nozzle Measured Using Phosphor Thermometry

International Journal of Turbomachinery Propulsion and Power 7, 29 (2022) https://doi.org/10.3390/ijtpp7040029

Henrik Feuk, **Francesco Pignatelli**, Arman Ahamed Subash, Ruike Bi, Robert-Zoltán Szász, Xue-Song Bai, Daniel Lörstad, Mattias Richter

The candidate designed the experiments, participated in the experimental campaign, supported the data analysis, and contributed to writing the manuscript.

Paper V: Effect of CO2 Dilution on Structures of Premixed Syngas/Air Flames in a Gas Turbine Model Combustor

Manuscript under Review in Combustion and Flame

Francesco Pignatelli, Saeed Derafshzan, David Sanned, Nikolaos Papafilippou, Robert-Zoltán Szász, Muhammad Aqib Chishty, Per Petersson, Xue-Song Bai, Rikard Gebart, Andreas Ehn, Mattias Richter, Daniel Lörstad, Arman Ahamed Subash

The candidate designed the experiments, led the experimental campaign, performed the experiments and the data analysis, and wrote the manuscript with the advice of the co-authors.

Printed by Media-Tryck, Lund 2023 NORDIC SWAN ECOLABEL 3041 0903

Faculty of Engineering
Department of Energy Sciences

ISRN LUTMDN/TMHP-23/1172-SE
ISBN 978-91-8039-513-7
ISSN 0282-1990